2007

NMR studies of the vanadium spin dynamics and spin structure in LiV2O4, CaV2O4, and (LixV1-x)3BO5 (x ≈ 0.33, 0.40)

Xiaopeng Zong
Iowa State University

NMR studies of the vanadium spin dynamics and spin structure in LiV_2O_4, CaV_2O_4, and $(Li_xV_{1-x})_3BO_5$ ($x \approx 0.33$, 0.40)

by

Xiaopeng Zong

A dissertation submitted to the graduate faculty

in partial fulfillment of the requirements for the degree of

DOCTOR OF PHILOSOPHY

Major: Condensed Matter Physics

Program of Study Committee:
David C. Johnston, Co-major Professor
Ferdinando Borsa, Co-major Professor
Jörg Schmalian
Robert McQueeney
Craig Ogilvie
Steve Martin

Iowa State University

Ames, Iowa

2007

献给我的父母

To my parents

TABLE OF CONTENTS

CHAPTER 1. Introduction

Strong electron correlation is believed to be an essential and unifying factor in diverse properties of condensed matter systems. Ground states that can arise due to electron correlation effects include Mott insulators,[1] heavy fermion,[2] ferromagnetism and antiferromagnetism,[3] spin glasses,[4] and high-temperature superconductivity.[5] The electronic systems in transition metal oxide compounds are often highly correlated. In this thesis, I will present experimental studies on three strongly correlated vanadium oxide compounds: LiV_2O_4, $(Li_xV_{1-x})_3BO_5$, and CaV_2O_4, which have completely different ground states.

1.1 Motivations

1.1.1 NMR Study of LiV_2O_4 Containing Magnetic Defects

Landau's Fermi liquid theory[6, 7] describes a metallic system where there exist strong Coulomb interactions between the electrons. The theory suggests that the low energy (low temperature) excitations (quasiparticles) of such a system have properties rather similar to those of a free electron gas. However, as a result of electron interactions, the effective mass of the quasiparticles is renormalized. Heavy fermion refers to a Landau Fermi liquid whose low energy quasiparticle excitations have an effective mass two to three orders of magnitude larger than the free electron mass. Typical manifestations of heavy mass are the large linear electronic specific heat coefficients and spin susceptibilities at low temperatures. Most heavy fermions are f-electron systems containing rare-earth or actinide elements. The heavy fermion behavior of those systems can be explained by the periodic Anderson model.[8] In the model, the f-electrons are highly localized and experience a strong on-site Coulomb repulsion between f-electrons. Because of the hybridization of the conduction electrons with the localized f-

electrons, the f-electron local moments are screened at low temperatures (Kondo effect) which leads to a large enhancement of the density of states near the Fermi level and a large effective mass of the quasiparticles in those systems.

Magnetically pure LiV_2O_4 is a rare d-electron heavy fermion system at low temperatures $T < 10$ K.[9] The low temperature linear electronic specific heat coefficient γ (0.42 J/mol K^2) and magnetic susceptibility χ_0 (≈ 0.01 cm^3/mol) show large ($\gtrsim 180$) enhancements compared to the values expected for a free electron gas, indicating the presence of strong electron correlations. Recent photoemission measurements[10] observed a sharp peak structure in the electronic density of states at ~ 4 meV above the Fermi level at low temperatures ($T < 20$ K), which confirmed the heavy fermion state in LiV_2O_4.

Figure 1.1 shows the spinel crystal structure (space group $Fd\bar{3}m$) of LiV_2O_4. All vanadium atoms are crystallographically equivalent. The vanadium atoms are inside octahedra with oxygen atoms on the vertices. The vanadium atoms have a fractional formal charge state of $V^{3.5+}$, so each vanadium atom retains 1.5 d-electrons. Another important feature in the crystal structure of LiV_2O_4 is the presence of geometrical frustration of the magnetic interactions. High temperature susceptibility data suggest that the nearest-neighbor interaction between vanadium atoms is antiferromagnetic. Because the vanadium atoms form a network of corner-shared tetrahedra, the frustration arises due to the triangular arrangement of the vanadium moments on each face of the tetrahedra.

Despite continuous theoretical efforts, a detailed understanding of the heavy fermion behaviors in LiV_2O_4 remains a great challenge. An obvious possible explanation is the Kondo effect similar to that in the f-electron heavy fermions. The five degenerate vanadium $3d$ orbitals are split by the crystal electric field (CEF) into an orbital triplet (t_{2g} orbitals) and an orbital doublet (e_g orbitals) ≈ 2 eV higher in energy than the t_{2g} orbitals. Due to a rhombohedral component to the CEF at the vanadium sites, the t_{2g} orbitals are slightly split into a singlet A_{1g} orbital and doublet E_g orbitals. It has been proposed[11, 12] that one of the 1.5 d-electrons occupies the narrow A_{1g} band and is highly localized and the remaining 0.5 electrons occupy a much broader E_g band. The electrons in the A_{1g} band play the role of local

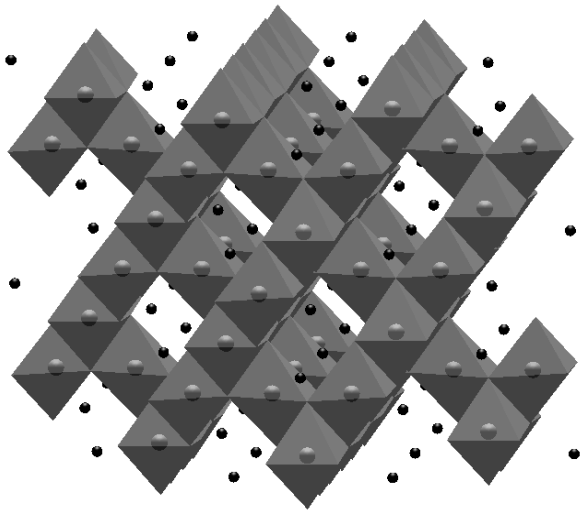

Figure 1.1 The spinel crystal structure of LiV_2O_4. The oxygen atoms are located on the vertices of the octahedra. The large spheres inside the octahedra are vanadium atoms and the small spheres outside the octahedra are lithium atoms.

moments and the electrons in the E_g band correspond to the conduction electrons. However, such a scenario lacks detailed theoretical support.[13] For example, it is hard to justify how an (antiferromagnetic) Kondo coupling can overwhelm a large (ferromagnetic) Hund's exchange coupling.[13]

The heavy fermion behavior might be closely related to the geometrical frustration in the system. It has been suggested that the frustration suppresses any long-range magnetic order so that the local spin or orbital fluctuations dominate the thermodynamic properties at low temperatures.[12, 14–17] A large enhancement of the electronic specific heat coefficient has been suggested from such a model.[16] However, a more quantitative comparison with the specific heat coefficient and other experimental results remains an unsolved task. There are other possible mechanisms to explain the heavy fermion behavior in LiV_2O_4.[13, 18] Recent quantum Monte Carlo simulations[13] suggested that the strongly correlated A_{1g} band constitutes a slightly doped Mott insulator, which, at low temperatures, exhibits a sharp (heavy) quasiparticle peak just above the Fermi level, which is consistent with the recent photoemission results.[10]

NMR was an important local probe in establishing the low temperature heavy fermion

behavior in LiV_2O_4.[9, 19] The low temperature T ^{7}Li nuclear spin lattice relaxation rate $1/T_1$ follows a Korringa relation $1/T_1 \propto T$ with a coefficient $1/T_1T = 2.2$ s^{-1}K^{-1}, 6000 times larger than in the non-heavy fermion isostructural superconducting[20] compound $LiTi_2O_4$.[21] The Korringa ratio $\kappa = 4\pi k_B \gamma_n^2 K^2 T_1 T/\hbar\gamma_e^2$, where K is the Knight shift, γ_n and γ_e are gyromagnetic ratio of ^{7}Li nuclear spin and the electronic spin, respectively, is equal to 0.7, which is close to the value of unity expected for a free electron gas.

Recently, we found that the low temperature ^{7}Li NMR properties of LiV_2O_4 are very sensitive to the presence of a small amount of magnetic defects (concentration $n = 0.73$ mol%) within the LiV_2O_4 spinel structure.[22, 23] The NMR properties exhibit inhomogeneous features such as inhomogeneous line broadening and a stretched exponential nuclear spin-lattice relaxation versus time. The nuclear spin-lattice relaxation rate versus temperature deviates from the Korringa relation and a peak was observed at temperature $T \sim 1$ K. One important issue is thus to understand the nature of the LiV_2O_4 system with magnetic defects, in particular, whether the heavy fermion properties are still preserved in the presence of magnetic defects and whether the observed inhomogeneity in the ^{7}Li NMR is related to an underlying spatial inhomogeneity in the electronic properties. In addition to its intrinsic interest, a study of the electronic state of LiV_2O_4 with magnetic defects may help us to better understand the heavy fermion mechanism in the magnetically pure material.

Under the above motivations, we carried out a systematic study of the variations of the ^{7}Li NMR properties versus magnetic defect concentration n for different n values in powders ($n = 0.21, 0.49$, and 0.83 mol%) and single crystals ($n = 0.38$ mol%) in the temperature range 0.5–4.2 K. The magnetic defect concentrations are determined through static magnetization measurements in the T range of 1.8–5.0 K.[12] We also studied the ac magnetic susceptibility χ_{ac} at 14 MHz from 0.5 to 6 K in the single crystals and in the powder sample with 0.83 mol% magnetic defects. Both the ^{7}Li NMR spectrum and nuclear spin-lattice relaxation rate are inhomogeneous in the presence of magnetic defects. We study a model assuming that the inhomogeneity in NMR arises from local field inhomogeneity due to different positions of the ^{7}Li nuclei relative to the magnetic defects. Our study shows that local field inhomogeneity

is an important effect of the magnetic defects. The results indicate that the heavy Fermi liquid survives the introduction of magnetic defects. Furthermore, our results indicate that the natures of the magnetic defects in the powder and single crystal samples are different. Field-dependent $\chi_{\rm ac}$ measurements show the signature of spin freezing in the powder sample ($n_{\rm defect} = 0.83$ mol%) at $T \approx 1.0$ K, which coincides with the peak position in the nuclear spin-lattice relaxation rate in the same sample. In contrast, spin freezing was not observed in the single crystals down to $T = 0.5$ K from either NMR or $\chi_{\rm ac}$ measurements, despite the relatively large magnetic defect concentration.

1.1.2 ^{17}O and ^{51}V NMR studies of zig-zag spin chain CaV_2O_4

Frustrated magnetic systems have attracted great research interest because such systems can exhibit diverse low temperature properties.[24] For example, both the heavy fermion behavior in LiV_2O_4 and the spin glass behavior in $(Li_xV_{1-x})_3BO_5$ discussed below are likely related to the presence of magnetic frustration in both systems. In many frustrated systems, frustration leads to a noncollinear magnetically ordered ground state. One well-known example is an XY-like antiferromagnet on a stacked, triangular lattice with only nearest-neighbor exchange interactions such as in $CsMnBr_3$[25] and $CsVI_3$[26]. Frustration in those systems results in a spin structure where the spins on three sublattices form 120° angles with nearest neighbors on the other sublattices.[27] Furthermore, experiments[28–32] and simulations[33–36] in frustrated Ising and Heisenberg systems show that frustration can result in a partially ordered state. Such a state is characterized by a coexistence in an equilibrium state of one or more magnetically ordered sublattices with at least one sublattice that stays disordered at all or a range of temperatures.

In a one-dimensional spin chain with an antiferromagnetic nearest-neighbor exchange interaction, frustration can be introduced by a nonzero antiferromagnetic next-nearest-neighbor exchange interaction. The Hamiltonian for such a system is written as

$$\mathcal{H} = J_1 \sum \boldsymbol{S}_i \cdot \boldsymbol{S}_{i+1} + J_2 \sum \boldsymbol{S}_i \cdot \boldsymbol{S}_{i+2}, \tag{1.1}$$

where $J_1(>0)$ and $J_2(>0)$ are the nearest and next-nearest-neighbor exchange interactions,

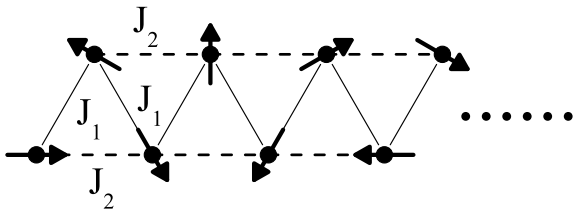

Figure 1.2 The helical spin configuration for a frustrated zig-zag antiferromagnetic classical spin chain with antiferromagnetic nearest- and next-nearest-neighbor exchange interactions J_1 and J_2, respectively. In the displayed spin configuration, the direction of each spin is changed by 150° counter clockwise relative to its nearest neighbor on lower left or upper left. This spin configuration corresponds to $J_2/J_1 = \sqrt{3}/6$.

respectively, and index i run through all the spins in the chain. In real materials, the next-nearest-neighbor interaction can be introduced by forming a zig-zag spin structure, which reduces the distance between next-nearest-neighbor spins. For a zig-zag spin chain with classical Heisenberg spins, the ground state has a helical configuration as shown in Fig. 1.2, when the ratio between the exchange constants satisfies $J_2/J_1 > 1/4$.[24] For $J_2/J_1 \leq 1/4$, the ground state spin configuration is a collinear structure.[24]

CaV_2O_4 is a possible candidate of a zig-zag spin chain system.[37, 38] It has an orthorhombic crystal structure (space group *Pnam*) at room temperature as displayed in Fig. 1.3. There are two crystallographically inequivalent vanadium sites which respectively form two inequivalent zig-zag spin chains along the c-axis. The formal charge state of the vanadium ions is V^{3+}, from which one expects a spin value of $S = 1$. T. Hikihara et al.[39] studied a quantum zig-zag spin-1 chain with anisotropic interactions described by

$$\mathcal{H} = \sum_{\rho=1}^{2} \left[J_\rho \sum_i \left(S_i^x S_{i+\rho}^x + S_i^y S_{i+\rho}^y + \Delta S_i^z S_{i+\rho}^z \right) \right], \tag{1.2}$$

where the index i runs through all spin sites along the zig-zag chain and $\Delta > 0$. In a phase region of $0 < \Delta \lesssim 0.7$ and $0.5 \lesssim J_2/J_1 < 1.4$ ($J_1 > 0$), the ground state of the system is a gapless chiral phase where there is a long range chiral order *without accompanying long range spin order*. This state has not been clearly observed for any system. In the case of isotropic interactions $\Delta = 1$, there is a Haldane energy gap[40] in the magnetic excitation spectrum for $0 < J_2/J_1 < 1.4$.[39, 41]

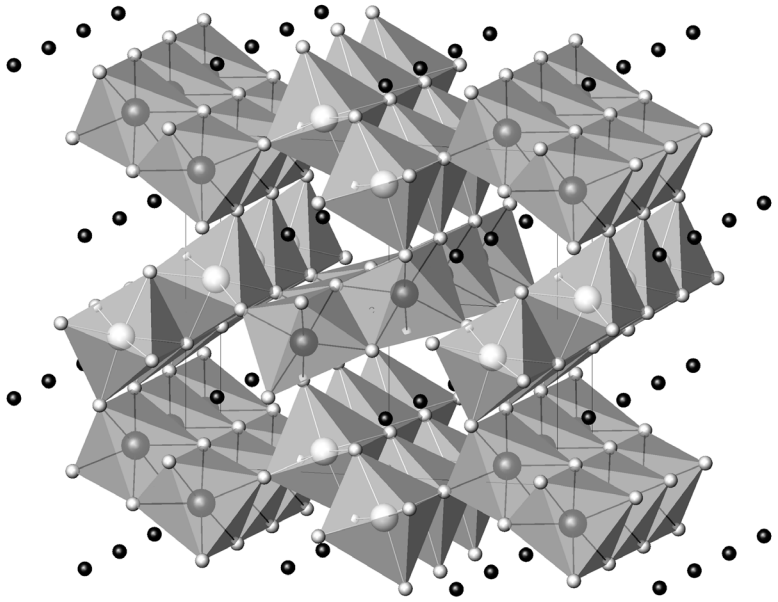

Figure 1.3 The crystal structure of CaV_2O_4. The large spheres are vanadium atoms where the two different shades correspond to the two crystallographically inequivalent sites. The small black spheres are calcium atoms and the small gray spheres on the vertices of the octahedra are oxygen sites.

Kikuchi et al. [37, 38] performed magnetization and ^{51}V NMR studies in CaV_2O_4 powders and suggested that the ground state of the system might be a gapless chiral phase with no long-range spin order.[37, 38] The lack of spin order was deduced from the observation of a ^{51}V NMR signal near the corresponding Larmor frequency $H\gamma_{\rm v}/(2\pi)$ for $2 < T < 160$ K. Both the Knight shift and magnetic susceptibility did not vanish in the low temperature limit ($T = 5$ K), suggesting the absence of an energy gap for magnetic excitations. Furthermore, the temperature dependence of the nuclear spin-lattice relaxation rate $1/T_1$ was found to be proportional to temperature in the temperature range 1.8 K $< T <$ 30 K, in contrast to thermally activated behavior in a gapped system. However, this suggestion of long-range chiral order without long-range spin order contradicts earlier powder neutron diffraction studies which showed that the system is in an antiferromagnetic state at 4.2 K.[42] The neutron diffraction pattern was found to be consistent with three collinear models with spins parallel to the b-axis. By assuming the same spin moment at all vanadium sites, the magnetic moment of

each vanadium spin was determined to be 1.06(6) μ_B, only about half the value expected for a vanadium spin with g-factor $g \approx 2$ and $S = 1$.[42] Recently, A. Niazi et al. grew CaV_2O_4 single crystals and an antiferromagnetic phase transition was observed for the annealed single crystals at $T_N \approx 70$ K.[43] The easy axis for spin ordering was found to be approximately along the b-axis. This result is consistent with the previous neutron scattering result.[42] However, the zero temperature limit of the susceptibility with the field along the easy-axis (b-axis) seems too large to be explained by the Van Vleck and core electron contributions, indicating a noncollinear spin structure in the ordered state.

In order to obtain further evidence of the magnetic phase transition and to study the magnetic properties in the ordered state, we carried out ^{51}V NMR studies on CaV_2O_4 single crystals and ^{17}O NMR studies on ^{17}O-enriched powder samples. The temperature dependences of the ^{17}O NMR line width and nuclear spin-lattice relaxation rate give strong evidence for a long-range antiferromagnetic transition at $T_N = 78$ K in the powder. We did not find a ^{51}V NMR signal at the normal Larmor frequency $\omega = \gamma_v H$, in disagreement with Refs. [38] and [37]. However, a *zero-field* ^{51}V NMR signal was observed at low temperatures ($f \approx 237$ MHz at 4.2 K) in the crystals. The field swept spectra with the field in different directions reveal indeed a noncollinear spin structure, and a model for the ordered magnetic structure was proposed.

1.1.3 Structure, Magnetization and NMR Studies of Spin Glass $(Li_xV_{1-x})_3BO_5$ with $x \approx 0.33$ and 0.40

Many disordered magnetic systems enter a spin glass state at low temperature.[4] In contrast to conventional magnets, the spins (magnetic moments) in spin glasses are in a disordered frozen state and do not exhibit any spatial periodicity.[44] Two ingredients are often present in spin glass systems: disorder and frustration. In some spin glass systems such as $Eu_xSr_{1-x}S$[45] and $Li_xZn_{1-x}V_2O_4$,[46] the frustration is inherent in the structure. In $Eu_xSr_{1-x}S$, the frustration comes from the opposite signs of nearest-neighbor (ferromagnetic) and next-nearest-neighbor (antiferromagnetic) exchange interactions between Eu^{2+} moments. In $Li_xZn_{1-x}V_2O_4$ which has the spinel structure, the frustration is geometric in origin and arises because vana-

dium moments occupy the vertices of tetrahedra and the interaction between nearest neighboring vanadium moments is antiferromagnetic. In other spin glasses, the frustration is closely related to the presence of disorder. An example in this class is the canonical spin glass systems such as CuMn, where due to the oscillatory nature of the RKKY interaction, the interactions between magnetic atoms can be either ferromagnetic or antiferromagnetic depending on their relative distance and thus significant frustration is present.

The spin glass transition is often detected by a dramatic change in the dynamic properties of the system. Upon approaching the spin glass transition, the spin fluctuations slow down rapidly.[47–50] The slowing down gives rise to a cusp in the temperature dependences of the ac magnetic susceptibility close to the spin glass transition temperature.[51, 52] In NMR and μSR experiments, the slowing down shows up as a peak in the temperature dependence of nuclear spin-lattice relaxation rate or the rate of longitudinal muon spin depolarization, respectively.[48, 50, 53] In the spin glass state, the magnetic response of the spin glass system exhibits complex behavior. One can observe irreversible behaviors such as a splitting versus temperature between the zero-field-cooled and field-cooled magnetization.[54] Upon changing the applied field in the spin glass state, the magnetization approaches its new equilibrium value with a very slow rate.[55] Beside irreversibility and slow relaxation, spin glasses also exhibit interesting aging and memory effects.[56, 57] The aging effect refers to the nonstationary dynamic properties of the spin glass system, i.e. the magnetic dynamic response depends on the time the system has been kept in the spin glass state. The memory effect refers to the system's ability to remember a previous magnetic state. For example, the system can return to a magnetization value of a previous state, which is at the same temperature as the current temperature, but is separated from the current state by a period during which the system was kept at a lower temperature.

The decay of the average spin autocorrelation function $q^{\alpha}(t) = \langle S_i^{\alpha}(0) S_i^{\alpha}(t) \rangle$ is highly nonexponential in spin glasses, where $\alpha (= x, y, z)$ is the spin component index, i is the spin site index, and $\langle \cdots \rangle$ denotes a spatial average.[47, 58–61] Above the spin glass transition temperature, Ogielski[47] observed the following empirical function for $q(t)$ ($\alpha = z$ for Ising

spins)

$$q(t) \sim t^{-x} \exp\left[-(t/\tau)^{\beta}\right] \tag{1.3}$$

in the simulation of the three dimensional short-range Ising spin glass, where exponents x ($0.1 < x < 0.5$) and β ($0.3 < \beta < 1$) are temperature dependent and both decrease monotonically with decreasing temperature. The correlation time τ diverges at the transition temperature and below the transition temperature only a power law decay can be observed for $q(t)$. A correlation of the form in Eq. (1.3) is supported by neutron spin echo, μSR, and ac susceptibility experiments.[58, 59, 62]

The origin of the nonexponential decay of $q(t)$ is an issue of continuous debate. One common approach is to assume that $q(t)$ arises from the average of a distribution of single exponential functions of different magnetic clusters in the system.[58, 62–67] Another viewpoint claims that the nonexponential spin autocorrelation function is an intrinsic, homogeneous feature of spin glasses.[59, 68] One argument to support such a view is that the different relaxation times are associated with different excitation modes in the system that overlap in space. Since a spin can take part in different modes simultaneously, the relaxation for each spin is nonexponential.[68, 69] Another homogeneous nonexponential relaxation mechanism is hierarchical relaxation where the relaxation pathway at a specific time depends on relaxation occurring in previous pathways.[70] Some simulations show that a situation intermediate between the above two viewpoints might exist in real spin glasses. By following the fluctuation of individual spins, it was found that even the relaxation of an individual spin is nonexponential and the detailed relaxation curves differ between different spins. [61, 71, 72]

Spin glasses are very sensitive to the presence of applied magnetic fields. In an applied magnetic field, the sharp cusp observed in zero field in the temperature dependence of the ac susceptibility is often rounded and suppressed to lower temperatures.[73] The applied field might also change the nature of spin glass freezing. In spin glasses at *zero* applied magnetic field, the existence of a true phase transition at finite temperature is supported by the universal static and dynamic scaling behaviors observed close to the spin glass transition temperature in many spin glass systems.[59, 74, 75] The spin glass transition seems to be destroyed by even

a very small field ($H = 2$ Oe) in the short range Ising spin glass $Fe_{0.5}Mn_{0.5}TiO_3$.[73, 76, 77] On the other hand, in Heisenberg spin glasses with RKKY interactions between the spins such as dilute CuMn and AuFe alloys, the persistence of a frozen spin glass phase in a strong magnetic field was inferred through magnetization and torque measurements.[78–81] The latter measurements do not, however, prove the existence of a (spin glass) phase transition in finite field.

NMR is a useful microscopic tool to study the local spin dynamics in spin glass systems.[49, 50, 82–84] In order to avoid the applied magnetic field affecting the electronic spin dynamics, some of the measurements were performed in either zero[49, 85] or small applied magnetic fields ($H < 1.33$ kOe).[84] The applied magnetic field was found to decrease the correlation time of electronic spin fluctuations upon increasing the applied magnetic field from 0.28 to 1.33 kOe in dilute CuMn spin glasses (Mn concentration ≤ 43 ppm). On the other hand, in CuMn spin glasses with higher Mn concentrations ($\sim 1\%$), a frozen configuration was observed at low temperatures ($T < 4.2$ K) below the zero field ordering temperature ($T_c = 10$ K) even under an applied field of 23 kOe.[83, 84] Thus, the effect of the magnetic field may depend on the average interaction strength between the magnetic moments, which are different in CuMn spin glasses with different Mn concentrations.

In our recent NMR studies in heavy fermion LiV_2O_4 containing 0.73 mol% magnetic defects, we found a stretched exponential behavior $1 - M(t)/M(\infty) = \exp[-(t/T_1^*)^\beta]$ for the recovery of the ^{7}Li nuclear magnetization $M(t)$ versus time t following a saturation pulse sequence in the temperature range 0.5–4.2 K.[22] Earlier μSR studies showed that LiV_2O_4 with 0.13 mol% magnetic defects undergoes a spin glass freezing below ~ 0.7 K.[86] The stretched exponential recovery is in strong contrast to a single exponential behavior observed in magnetically pure LiV_2O_4 samples, where no spin glass behavior was observed down to 20 mK.[9] In order to better understand the relation between the stretched exponential recovery and the dynamics of spin glasses, it is highly desirable to study the NMR nuclear spin-lattice relaxation behavior in other spin glass systems.

We obtained $(Li_xV_{1-x})_3BO_5$ single crystals in our attempt to grow single crystals of LiV_2O_4

using $LiBO_2$ flux. It has an orthorhombic crystal structure (space group *Pbam*), where Li or V statistically occupy to varying extents four inequivalent sites VL1–VL4 that are octahedrally coordinated by oxygen atoms. Early magnetization measurements showed a deviation of the magnetization M from being proportional to the applied magnetic field H at temperatures $T < 25$ K, indicating a possible spin glass state.[87] However, additional experimental studies are necessary to further characterize the magnetic state of the system at low temperatures.

To further characterize the structural and magnetic properties of $(Li_xV_{1-x})_3BO_5$ and to investigate the dynamic properties of a spin glass system in a strong magnetic field, we carried out studies of $(Li_xV_{1-x})_3BO_5$ powders ($x = 0.33$) and single crystals ($x = 0.40$) by x-ray diffraction, magnetization and NMR measurements. The structure contains both frustration and disorder, the two ingredients often considered necessary for a spin glass. Magnetization measurements show an overall antiferromagnetic interaction among vanadium spins and reveal a transition into a spin glass state at a sample and magnetic field dependent temperature below ~ 10 K. Furthermore, we found that the ^{7}Li nuclear spin lattice relaxation versus time t in $(Li_{0.33}V_{0.67})_3BO_5$ indeed follows a temperature dependent stretched exponential behavior $1 - M(t)/M(\infty) = \exp[-(t/T_1^*)^\beta]$, where $M(t)$ is the longitudinal nuclear magnetization. It was previously shown[22, 88] that a unique distribution of nuclear spin lattice relaxation rates $1/T_1$'s can be obtained from the observed stretched exponential recovery with given fitted values of $1/T_1^*$ and β. By assuming that the stretched exponential nuclear relaxation is dominated by electronic dynamical heterogeneity in the system, we derived the temperature-dependent distribution of the vanadium electronic spin relaxation times from the ^{7}Li relaxation data. The derived distribution of electronic spin relaxation times is found to be consistent with other NMR results, supporting the presence of electronic dynamical inhomogeneity in spin glasses. The temperature at which a dramatic dynamical slowing down is observed in NMR is insensitive to the presence of strong magnetic fields up to 4.7 T, consistent with previous NMR results in *Cu*Mn spin glasses with high Mn concentrations.[83, 84]

1.2 Organization of the Thesis

The thesis is organized as follows. In chapter 2, we give a review of the basic NMR principles and experimental methods that are helpful to an understanding of the NMR results presented in the thesis. ^{7}Li NMR studies on LiV_2O_4 powder and single crystal samples with different concentrations of magnetic defects are reported in chapters 3 and 4. ^{17}O and ^{51}V NMR studies on CaV_2O_4 samples are presented in chapter 5. Structure, magnetization, and ^{7}Li and ^{11}B NMR studies on $(Li_xV_{1-x})_3BO_5$ samples are presented in chapter 6. In chapter 7, we give a summary of the thesis. This thesis also contains an appendix that presents a ^{11}B NMR study on two isostructural superconductors OsB_2 and RuB_2 in their normal state.

References

[1] N. F. Mott, *Metal-Insulator Transitions* (Taylor & Francis Ltd, London, 1974).

[2] G. R. Stewart, Rev. Mod. Phys. **56**, 755 (1984).

[3] P. Fazekas, *Lecture Notes on Electron Correlation and Magnetism* (World Scientific, Singapore, 1999).

[4] K. Binder and A. P. Young, Rev. Mod. Phys. **58**, 801 (1986).

[5] Patrick A. Lee, arXiv:0708.2115v1 [cond-mat.str-el] (unpublished).

[6] L. D. Landau, Sov. Phys. JETP **3**, 920 (1957).

[7] L. D. Landau, Sov. Phys. JETP **5**, 101 (1957).

[8] A. C. Hewson, *The Kondo Problem to Heavy Fermions* (Cambridge University Press, Cambridge, 1993).

[9] S. Kondo, D. C. Johnston, C. A. Swenson, F. Borsa, A. V. Mahajan, L. L. Miller, T. Gu, A. I. Goldman, M. B. Maple, D. A. Gajewski, E. J. Freeman, N. R. Dilley, R. P. Dickey, J. Merrin, K. Kojima, G. M. Luke, Y. J. Uemura, O. Chmaissem, and J. D. Jorgensen, Phys. Rev. Lett. **78**, 3729 (1997).

[10] A. Shimoyamada, S. Tsuda, K. Ishizaka, T. Kiss, T. Shimojima, T. Togashi, S. Watanabe, C. Q. Zhang, C. T. Chen, Y. Matsushita, et al., Phys. Rev. Lett. **96**, 026403 (2006).

[11] V. I. Anisimov, M. A. Korotin, M. Zölfl, T. Pruschke, K. Le Hur, and T. M. Rice, Phys. Rev. Lett. **83**, 364 (1999).

[12] S. Kondo, D. C. Johnston, and L. L. Miller, Phys. Rev. B **59**, 2609 (1999).

[13] R. Arita, K. Held, A. V. Lukoyanov, and V. I. Anisimov, Phys. Rev. Lett. **98**, 166402 (2007).

[14] V. Yushankhai, A. Yaresko, P. Fulde, and P. Thalmeier, Phys. Rev. B **76**, 085111 (2007).

[15] V. Eyert, K.-H. Höck, S. Horn, A. Loid, and P. S. Riseborough, Europhys. Lett. **46**, 762 (1999).

[16] Y. Yamashita and K. Ueda, Phys. Rev. B **67**, 195107 (2003).

[17] H. Tsunetsugu, J. Phys. Soc. Jpn. **71**, 1844 (2002).

[18] P. Fulde, J. Phys.: Condens. Matter **16**, S591 (2004).

[19] A. V. Mahajan, R. Sala, E. Lee, F. Borsa, S. Kondo, and D. C. Johnston, Phys. Rev. B **57**, 8890 (1998).

[20] D. C. Johnston, J. Low Temp. Phys. **25**, 145 (1976).

[21] M. Dalton, D. P. Tunstall, J. Todd, S. Arumugam, and P. P. Edwards, J. Phys.: Condens. Matter **6**, 8859 (1994).

[22] D. C. Johnston, S.-H. Baek, X. Zong, F. Borsa, J. Schmalian, and S. Kondo, Phys. Rev. Lett. **95**, 176408 (2005).

[23] H. Kaps, M. Brando, W. Trinkl, N. Büttgen, A. Loidl, E.-W. Scheidt, M. Klemm, and S. Horn, J. Phys.: Condens. Matter **13**, 8497 (2001).

[24] H. T. Diep, *Frustrated Spin Systems* (World Scientific, Hackensack, New Jersey, 2004).

[25] T. E. Mason, B. D. Gaulin, and M. F. Collins, Phys. Rev. B **39**, 586 (1989).

[26] H. W. Zandbergen, J. Solid State Chem. **37**, 308 (1981).

[27] M. F. Collins and O. A. Petrenko, Can. J. Phys. **75**, 605 (1997).

[28] X. G. Zheng, T. Kawae, H. Yamada, K. Nishiyama, and C. N. Xu, Phys. Rev. Lett. **97**, 247204 (2006).

[29] M. A. Gîrţu, C. M. Wynn, W. Fujita, K. Awaga, and A. J. Epstein, Phys. Rev. B **57**, R11058 (1998).

[30] M. A. Gîrţu, C. M. Wynn, W. Fujita, K. Awaga, and A. J. Epstein, Phys. Rev. B **61**, 4117 (2000).

[31] G. Cao, V. Durairaj, S. Chikara, S. Parkin, and P. Schlottmann, Phys. Rev. B **75**, 134402 (2007).

[32] S. Niitaka, K. Yoshimura, K. Kosuge, M. Nishi, and K. Kakurai, Phys. Rev. Lett. **87**, 177202 (2001).

[33] R. Quartu and H. T. Diep, Phys. Rev. B **55**, 2975 (1997).

[34] P. Azaria, H. T. Diep, and H. Giacomini, Phys. Rev. Lett. **59**, 1629 (1987).

[35] D. Blankschtein, M. Ma, A. N. Berker, G. S. Grest, and C. M. Soukoulis, Phys. Rev. B **29**, 5250 (1984).

[36] C. Santamaria and H. T. Diep, J. Appl. Phys. **81**, 5276 (1997).

[37] H. Kikuchi, M. Chiba, and T. Kubo, Can. J. Phys. **79**, 1551 (2001).

[38] H. Fukushima, H. Kikuchi, M. Chiba, Y. Fujii, Y. Yamamoto, and H. Hori, Prog. Theor. Phys. Supp. **145**, 72 (2002).

[39] T. Hikihara, M. Kaburagi, H. Kawamura, and T. Tonegawa, J. Phys. Soc. Jpn. **69**, 259 (2000).

[40] F. D. M. Haldane, Phys. Rev. Lett. **50**, 1153 (1983).

[41] A. Kolezhuk, R. Roth, and U. Schollwöck, Phys. Rev. Lett. **77**, 5142 (1996).

[42] J. M. Hastings, L. M. Corliss, W. Kunnmann, and S. La Placa, J. Phys. Chem. Solids **28**, 1089 (1967).

[43] A. Niazi, S. Bud'ko, A. Honecker, J. Q. Yan, D. L. Schlagel, T. A. Lograsso, and D. C. Johnston, (unpublished); A. Niazi, D. C. Johnston, S. Bud'ko, D. L. Schlagel, T. A. Lograsso, and A. Honecker, Bull. Am. Phys. Soc. **51**, 192 (2006), Abstract B23.6.

[44] K. H. Fischer and J. A. Hertz, *Spin glasses* (Cambridge University Press, Cambridge, 1991).

[45] H. Mydosh, Lecture Notes in Physics **192**, 90 (1983).

[46] Y. Ueda, N. Fujiwara, and H. Yasuoka, J. Phys. Soc. Jpn. **66**, 778 (1997).

[47] A. T. Ogielski, Phys. Rev. B **32**, 7384 (1985).

[48] Y. J. Uemura, T. Yamazaki, D. R. Harshman, M. Senba, and E. J. Ansaldo, Phys. Rev. B **31**, 546 (1985).

[49] M. C. Chen and C. P. Slichter, Phys. Rev. B **27**, 278 (1983).

[50] D. Bloyet, E. Varoquaux, C. Vibet, O. Avenel, and M. P. Berglund, Phys. Rev. Lett. **23**, 250 (1978).

[51] C. A. M. Mulder, A. J. van Duyneveldt, and J. A. Mydosh, Phys. Rev. B **23**, 1384 (1981).

[52] C. A. M. Mulder, A. J. van Duyneveldt, and J. A. Mydosh, Phys. Rev. B **25**, 515 (1982).

[53] R. H. Heffner, M. Leon, M. E. Schillaci, D. E. MacLaughlin, and S. A. Dodds, J. Appl. Phys. **53**, 2174 (1982).

[54] S. Nagata, P. H. Keesom, and H. R. Harrison, Phys. Rev. B **19**, 1633 (1979).

[55] L. Lundgren, P. Svedlindh, P. Nordblad, and O. Beckman, Phys. Rev. Lett. **51**, 911 (1983).

[56] F. Lefloch, J. Hammann, M. Ocio, and E. Vincent, Europhys. Lett. **18**, 647 (1992).

[57] A. Maiorano, E. Marinari, and F. Ricci-Tersenghi, Phys. Rev. B **72**, 104411 (2005).

[58] A. P. Murani, J. Magn. Magn. Mater. **22**, 271 (1981).

[59] C. Pappas, F. Mezei, G. Ehlers, P. Manuel, and I. A. Campbell, Phys. Rev. B **68**, 054431 (2003).

[60] K. Gunnarsson, P. Svedlindh, P. Nordblad, L. Lundgren, H. Aruga, and A. Ito, Phys. Rev. Lett. **61**, 754 (1988).

[61] H. Takano and S. Miyashita, J. Phys. Soc. Jpn. **64**, 423 (1995).

[62] I. A. Campbell, A. Amoto, F. N. Gygax, D. Herlach, A. Schenck, R. Cywinski, and S. H. Kilcoyne, Phys. Rev. Lett. **72**, 1291 (1994).

[63] L. Lundgren, P. Svedlindh, and O. Beckman, J. Magn. Magn. Mater. **25**, 33 (1981).

[64] L. E. Wenger, Lecture Notes in Physics **192**, 60 (1983).

[65] F. Matsukura and Y. Tazuke, J. Phys. Soc. Jpn. **63**, 1474 (1994).

[66] D. A. Smith, J. Phys. F: Metal Phys. **4**, L266 (1974).

[67] L. Lundgren, P. Nordblad, and P. Svedlindh, Phys. Rev. B **34**, 8164 (1986).

[68] A. Keren, G. Bazalitsky, I. Campbell, and J. S. Lord, Phys. Rev. B **64**, 054403 (2001).

[69] R. M. C. de Almeida, N. Lemke, and I. A. Campbell, Braz. J. Phys. **30**, 701 (2000).

[70] R. G. Palmer, D. L. Stein, E. Abrahams, and P. W. Anderson, Phys. Rev. Lett. **53**, 958 (1984).

[71] S. C. Glotzer, N. Jan, T. Lookman, A. B. MacIsaac, and P. H. Poole, Phys. Rev. E **57**, 7350 (1998).

[72] C. Brangian, W. Kob, and K. Binder, J. Phys. A: Math. Gen. **35**, 191 (2002).

[73] J. Mattsson, T. Jönsson, P. Nordblad, H. Aruga Katori, and A. Ito, Phys. Rev. Lett. **74**, 4305 (1995).

[74] K. H. Fisher and J. A. Hertz, *Spin Glasses* (Cambridge University Press, Cambridge, 1991).

[75] P. Nordblad and P. Svendlidh, in *Spin Glasses and Random Fields*, edited by A. P. Young (World Scientific, London, 1997).

[76] P. E. Jönsson, H. Takayama, H. A. Katori, and A. Ito, Phys. Rev. B **71**, 180412 (2005).

[77] P. E. Jönsson and H. Takayama, J. Phys. Soc. Jpn. **74**, 1131 (2005).

[78] G. G. Kenning, D. Chu, and R. Orbach, Phys. Rev. Lett. **66**, 2923 (1991).

[79] D. Chu, G. G. Kenning, and R. Orbach, Phys. Rev. Lett. **72**, 3270 (1994).

[80] D. Petit, L. Fruchter, and I. A. Campbell, Phys. Rev. Lett. **83**, 5130 (1999).

[81] D. Petit, L. Fruchter, and I. A. Campbell, Phys. Rev. Lett. **88**, 207206 (2002).

[82] D. E. MacLaughlin and H. Alloul, Phys. Rev. Lett. **36**, 1158 (1976).

[83] D. E. MacLaughlin and H. Alloul, Phys. Rev. Lett. **38**, 181 (1977).

[84] D. A. Levitt and R. E. Walstedt, Phys. Rev. Lett. **38**, 178 (1977).

[85] H. Alloul, Phys. Rev. Lett. **42**, 603 (1979).

[86] J. Merrin, Y. Fudamoto, K. M. Kojima, M. Larkin, G. M. Luke, B. Nachumi, Y. J. Uemura, S. Kondo, and D. C. Johnston, J. Magn. Magn. Mater. **177-181**, 799 (1998).

[87] M. Onoda, J. Solid State Chem. **141**, 418 (1998).

[88] D. C. Johnston, Phys. Rev. B **74**, 184430 (2006).

CHAPTER 2. Introduction to Nuclear Magnetic Resonance

Nuclear magnetic resonance (NMR) is a powerful microscopic tool to study the electronic and magnetic properties of condensed matter systems. In Sec. 2.1, we will introduce the basic physical principles of nuclear induction experiments[1] and discuss the meaning of the NMR parameters (T_1, T_2, Knight shift, and line width) and their connection with microscopic properties in condensed matter systems. In Sec. 2.2, we will discuss the experimental methods to measure those NMR parameters.

2.1 NMR Principles and Definition of the Parameters

2.1.1 Motion of Isolated Nuclear Spins

When a nuclear spin with angular momentum $\hbar\boldsymbol{I}$ and magnetic moment $\boldsymbol{\mu} = \gamma_{\rm n}\hbar\boldsymbol{I}$ is located inside a uniform static magnetic field $\boldsymbol{H}$, the interaction between the field and magnetic moment is described by the following simple Hamiltonian:

$$\mathcal{H} = -\boldsymbol{\mu}\cdot\boldsymbol{H} = -\gamma_{\rm n}\hbar H_0 I_z, \tag{2.1}$$

where the field is taken to be H_0 along the $\hat{\boldsymbol{k}}$ direction, $\gamma_{\rm n}$ is the gyromagnetic ratio of the nuclear spin, and $\hbar$ is Planck's constant divided by 2π. We denote the unit vectors along the x, y and z axes by $\hat{\boldsymbol{i}}$, $\hat{\boldsymbol{j}}$, and $\hat{\boldsymbol{k}}$, respectively. The energy eigenvalues consist of a set of equally spaced Zeeman levels: $E = -\gamma_{\rm n}\hbar H m$, where $m = -I, -I+1, \cdots, I$.

The principle feature of nuclear magnetic resonance is the observation of transitions between the above Zeeman levels, caused by an applied radio frequency (RF) field with a frequency at resonance with the Larmor precession of nuclear moments around the constant field $\boldsymbol{H}$. One common method to detect such transitions is nuclear induction, which was originally used by F.

Bloch and his co-workers.[1, 2] The principles of nuclear induction experiments will be described below. A classical description is sufficient to understand the principles. The equations which follow still hold in a quantum mechanical description provided that one replaces the vectors by the quantum mechanical expectation values of the corresponding operators.

According to the theory of classical mechanics and electrodynamics, the equation of motion for a system of nuclear spins under a uniform external magnetic field $\boldsymbol{H}$ is given by

$$\frac{d\boldsymbol{L}}{dt} = \boldsymbol{M} \times \boldsymbol{H}, \tag{2.2}$$

where $\boldsymbol{L}$ is the total angular momentum of the nuclear system, $\boldsymbol{M}$ the total magnetization, and we have ignored for the moment the effects of nuclear relaxation processes and interactions between nuclear spins. Since $\boldsymbol{M} = \gamma_{\mathrm{n}}\boldsymbol{L}$, the above equation can be rewritten as

$$\frac{d\boldsymbol{M}}{dt} = \gamma_{\mathrm{n}}\boldsymbol{M} \times \boldsymbol{H}. \tag{2.3}$$

For a constant field $\boldsymbol{H}$, Eq. (2.3) describes the Larmor precession of $\boldsymbol{M}$ with angular frequency $\gamma_{\mathrm{n}}\boldsymbol{H}$.

Next we transform Eq. (2.3) into a reference frame rotating with a constant angular velocity $\boldsymbol{\Omega}$ along the $\hat{\boldsymbol{k}}$ direction. We denote vector components in the rotating reference frame with primes and define the time derivative of an arbitrary vector $\boldsymbol{A}$ in this frame by

$$\frac{\delta \boldsymbol{A}}{\delta\, t} = \hat{\boldsymbol{i}}'\frac{dA'_x}{dt} + \hat{\boldsymbol{j}}'\frac{dA'_y}{dt} + \hat{\boldsymbol{k}}'\frac{dA'_z}{dt}.$$

With respect to the nonrotating (laboratory) frame, the directions of $\hat{\boldsymbol{i}}'$ and $\hat{\boldsymbol{j}}'$ change with time as:

$$\hat{\boldsymbol{i}}' = \hat{\boldsymbol{i}}\cos\Omega t + \hat{\boldsymbol{j}}\sin\Omega t$$

and

$$\hat{\boldsymbol{j}}' = \hat{\boldsymbol{j}}\cos\Omega t - \hat{\boldsymbol{i}}\sin\Omega t.$$

Therefore, one has

$$\frac{d\boldsymbol{A}}{d\, t} = \frac{\delta\, \boldsymbol{A}}{\delta\, t} + \boldsymbol{\Omega} \times \boldsymbol{A} \tag{2.4}$$

Then by setting $\boldsymbol{A} = \boldsymbol{M}$ and combining Eqs. (2.3) and (2.4), one has

$$\frac{\delta\, \boldsymbol{M}}{\delta\, t} = \boldsymbol{M} \times (\gamma_{\mathrm{n}}\boldsymbol{H} + \boldsymbol{\Omega}). \tag{2.5}$$

This equation shows that the equation of motion in Eq. (2.3) remains the same in the rotating reference frame as long as we replace the field $\boldsymbol{H}$ by a new field $\boldsymbol{H}_{\rm eff} = \boldsymbol{H} + \boldsymbol{\Omega}/\gamma_{\rm n}$.

In typical NMR experiments, the uniform applied field $\boldsymbol{H}$ consists of a constant field $H_0\hat{\boldsymbol{k}}$ plus a small oscillating field $\boldsymbol{H}_1(t) = 2H_1\hat{\boldsymbol{i}}\cos\Omega t$ perpendicular to $\hat{\boldsymbol{k}}$. The latter can be decomposed into two fields rotating in opposite directions: $\boldsymbol{H}_\pm = H_1(\hat{\boldsymbol{i}}\cos\Omega t \pm \hat{\boldsymbol{j}}\sin\Omega t)$. Since $H_0 \gg H_1$, one naively expects the effect of the two components $\boldsymbol{H}_\pm$ to be negligible. We will show that the effect of $\boldsymbol{H}_-$ becomes important close to the resonance (we use a right-handed coordinate system). In the reference frame rotating with angular velocity $-\Omega\hat{\boldsymbol{k}}$, both the constant field $H_0\hat{\boldsymbol{k}}$ and $\boldsymbol{H}_-$ are static. The $\boldsymbol{H}_+$ component appears as a rotating field with an angular frequency 2Ω, so its effect is averaged out to zero. The effective field in the rotating frame after neglecting $\boldsymbol{H}_+$ becomes $\boldsymbol{H}_{\rm eff} = (H_0 - \Omega/\gamma_{\rm n})\hat{\boldsymbol{k}}' + H_1\hat{\boldsymbol{i}}'$ and the equation of motion is

$$\frac{\delta \boldsymbol{M}}{\delta t} = \gamma_{\rm n}\boldsymbol{M} \times \left[(H_0 - \Omega/\gamma_{\rm n})\hat{\boldsymbol{k}}' + H_1\hat{\boldsymbol{i}}'\right]. \tag{2.6}$$

Equation (2.6) shows that the effect of the strong external field H_0 can be completely canceled by the rotation in the rotating frame if the resonance condition $\Omega = \gamma_{\rm n}H_0$ is satisfied. Then the motion of the nuclear spins is only affected by their interaction with the RF field H_1. It is then possible using an RF pulse at frequency $\gamma_{\rm n}H/(2\pi)$ applied for a time $\tau = \pi/(2\gamma_{\rm n}H_0)$ to tilt the nuclear magnetization away from the strong field $\boldsymbol{H}_0$, and upon removal of the RF field H_1, the tilted nuclear magnetization precesses around $\boldsymbol{H}_0$ and thus induces a rotating RF flux in the x-y plane. If the nuclear spin system under study is surrounded by a coil wound with its axis parallel to the x-y plane, then an RF voltage signal across its terminals is induced. It is such a signal that is detected in the nuclear induction method. The techniques that use RF pulses to manipulate and observe the motions of nuclear spins are called pulsed NMR. A detailed discussion of NMR measurements based on pulsed NMR techniques will be presented in Sec. 2.2.

2.1.2 Nuclear Spin Lattice Relaxation

In the above discussions, we ignored the interactions of nuclear spins with their environments. Such interactions have the effect of allowing the system to relax into a state that is in thermal equilibrium with the environment. In thermal equilibrium, the nuclear spin system has a net magnetization along the direction of the field with the equilibrium magnetization *per mole* of nuclear spins given by the nuclear Curie law for M_z

$$M_{0z} = H_0 \frac{\hbar^2 \gamma_{\rm n}^2 I(I+1) N_{\rm A}}{3 k_{\rm B} T}, \tag{2.7}$$

and where

$$M_{0x} = M_{0y} = 0,$$

T is the absolute temperature, $k_{\rm B}$ is Boltzmann's constant, and $N_{\rm A}$ is Avogadro's number.

Bloch[1] introduced the effect of relaxation phenomenologically into the equations of motion (2.3) by introducing T_1 and T_2 as the time constants for relaxations of the longitudinal and transverse magnetizations, respectively. The Bloch equations are

$$\begin{aligned} \frac{dM_z}{dt} &= \gamma(\boldsymbol{M} \times \boldsymbol{H})_z + \frac{M_z - M_{0z}}{T_1} \\ \frac{dM_x}{dt} &= \gamma(\boldsymbol{M} \times \boldsymbol{H})_x + \frac{M_x}{T_2} \\ \frac{dM_y}{dt} &= \gamma(\boldsymbol{M} \times \boldsymbol{H})_y + \frac{M_y}{T_2}. \end{aligned} \tag{2.8}$$

Two different time scales T_1 and T_2 have been introduced to characterize the longitudinal and transverse relaxations, respectively, because these two relaxation processes in general involve different physical mechanisms. During the T_1 relaxation process, the total Zeeman energy of the system changes with time, so an exchange of energy with the heat bath (lattice) is necessary. The heat bath can be of many forms such as molecular rotation, lattice vibration, or electronic spin fluctuations. The T_2 process is called the nuclear spin-spin or transverse spin relaxation. The nuclear Zeeman energy is conserved during this relaxation process and no energy exchange between the nuclear spin system and the heat bath is required. Mechanisms responsible for the T_2 process will be discussed in subsection 2.1.3.

Measurements of nuclear spin-lattice relaxation rates are particularly useful to study the electronic spin fluctuations in condensed matter systems. Electronic spin fluctuations produce fluctuating local magnetic fields that interact with nuclear spins and induce transitions between adjacent nuclear Zeeman levels. $1/T_1$ can be obtained by solving the master equations that describe the evolution of the nuclear spin populations of different Zeeman levels.[3] If the initial nuclear populations of different Zeeman levels follow a Boltzmann distribution, then recovery of the nuclear magnetization follows a single exponential with a time constant T_1 given by

$$1/T_1 = 2W \equiv 2\frac{W_{m\to m-1}}{(I-m+1)(I+m)}, \tag{2.9}$$

where $W_{m\to m-1}$ is the induced transition rate between adjacent nuclear Zeeman levels $I_z = |m\rangle$ and $|m-1\rangle$ and W is independent of m.[3] In the limit of small perturbation of nuclear Zeeman levels $h(t) \ll H_0$, where $\boldsymbol{h}(t)$ is the local fluctuating magnetic field at a nuclear site, then for that nucleus the transition rate can be calculated by time dependent perturbation theory and one has[4]

$$\frac{1}{T_1} = 2W = \frac{\gamma_{\rm n}^2}{2}\int_{-\infty}^{\infty}\langle h_x(0)h_x(t) + h_y(0)h_y(t)\rangle \exp(-i\omega_{\rm n}t)\,{\rm d}t, \tag{2.10}$$

where $\omega_{\rm n} = \gamma_{\rm n}H_0$ is the Larmor frequency of the nuclear spins, $h_x(t)$ and $h_y(t)$ are components of the fluctuating local fields perpendicular to the external field $H_0\hat{\boldsymbol{k}}$ at the nuclear site, and $\langle\cdots\rangle$ denotes an average over choices of the time origin.

In order to relate $1/T_1$ to the electronic spin dynamics, consider the following bilinear coupling Hamiltonian between a nuclear spin $\boldsymbol{I}$ at the origin $\boldsymbol{r} = 0$ and the surrounding localized electronic spins $\boldsymbol{S}_i$,

$$\mathcal{H}' = \sum_i \sum_{\alpha\beta} S_i^{\alpha}\mathcal{A}_{\alpha,\beta}(\boldsymbol{r}_i)I_{\beta}, \tag{2.11}$$

where $\alpha, \beta = x, y, z$, $\mathcal{A}$ is a 3 by 3 hyperfine coupling tensor, and $\sum_i$ runs over all surrounding electronic spin sites. When the electronic spins are in the paramagnetic state $\langle \boldsymbol{S}_i\rangle = 0$ (for zero applied magnetic field), Eq. (2.11) defines an effective fluctuating field $\boldsymbol{h}$ with spatial components

$$h_{\beta} = -\frac{1}{\hbar\gamma_{\rm n}}\sum_i\sum_{\alpha} S_i^{\alpha}\mathcal{A}_{\alpha,\beta}(\boldsymbol{r}_i). \tag{2.12}$$

Inserting Eq. (2.12) into Eq. (2.10) and assuming no correlation between different electronic spin components, one has

$$\frac{1}{T_1} = \frac{1}{2\hbar^2} \sum_{\alpha'=x,y} \sum_{i,j} \sum_{\alpha} \mathcal{A}_{\alpha,\alpha'}(\boldsymbol{r}_i)\mathcal{A}_{\alpha,\alpha'}(\boldsymbol{r}_j) J^{\alpha}_{ij}(\omega_0), \tag{2.13}$$

where $J^{\alpha}_{i,j}(\omega_{\rm n})$ is the Fourier transform of the two spin correlation function defined as

$$J^{\alpha}_{i,j}(\omega_{\rm n}) = \int_{-\infty}^{\infty} dt\, e^{-i\,t\omega_{\rm n}} \langle S^{\alpha}_i(t) S^{\alpha}_j(0)\rangle.$$

For a system possessing translational invariance, the spectral density $J^{\alpha}_{i,j}(\omega_{\rm n})$ is only a function of $\boldsymbol{r}_i - \boldsymbol{r}_j$, so it can be written as $J^{\alpha}(\omega_{\rm n}, \boldsymbol{r}_i - \boldsymbol{r}_j)$. It is convenient to express $J^{\alpha}(\omega_{\rm n}, \boldsymbol{r}_i - \boldsymbol{r}_j)$ in terms of its Fourier components in $\boldsymbol{q}$ space

$$\begin{aligned} J^{\alpha}(\omega_{\rm n}, \boldsymbol{r}_i - \boldsymbol{r}_j) &= \frac{1}{N} \sum_{\boldsymbol{q}} J^{\alpha}(\omega_{\rm n}, \boldsymbol{q}) {\rm e}^{i\boldsymbol{q}(\boldsymbol{r}_i - \boldsymbol{r}_j)} \\ &= \frac{1}{N} \frac{2k_{\rm B}T}{N_{\rm A}(g\mu_{\rm B})^2} \sum_{\boldsymbol{q}} \frac{\chi''_{\alpha}(\omega_{\rm n}, \boldsymbol{q})}{\omega_{\rm n}} {\rm e}^{i\boldsymbol{q}(\boldsymbol{r}_i - \boldsymbol{r}_j)}, \end{aligned} \tag{2.14}$$

where N is the number of lattice points in the system, $\sum_{\boldsymbol{q}}$ runs over all the $\boldsymbol{q}$ values in the first Brillouin zone,* χ'' is the imaginary part of the magnetic susceptibility per mole of electronic spins, and the fluctuation dissipation theorem[5] is used.

Substituting Eq. (2.14) into Eq. (2.13), one has

$$\frac{1}{T_1} = \frac{1}{N\hbar^2} \frac{k_{\rm B}T}{N_{\rm A}(g\mu_{\rm B})^2} \sum_{\boldsymbol{q}} \sum_{\alpha'=x,y} \sum_{\alpha} |\mathcal{A}_{\alpha,\alpha'}(\boldsymbol{q})|^2 \frac{\chi''_{\alpha}(\omega_{\rm n}, \boldsymbol{q})}{\omega_{\rm n}}, \tag{2.15}$$

where $\mathcal{A}_{\alpha,\alpha'}(q) = \sum_i \mathcal{A}_{\alpha,\alpha'}(\boldsymbol{r}_i) {\rm e}^{-i\boldsymbol{q}\cdot\boldsymbol{r}_i}$ is the Fourier transform of $\mathcal{A}_{\alpha,\alpha'}(\boldsymbol{r})$. The presence of the "filter" factors $|\mathcal{A}_{\alpha,\alpha'}(\boldsymbol{q})|^2$ complicates the relationship between $1/T_1$ and $\chi''(\omega_{\rm n}, \boldsymbol{q})$. On the other hand, if an explicit expression for the "filter" factors can be obtained from theoretical considerations, one can obtain direct information on the symmetry and on the correlation properties of the fluctuations.[6]

*We assume that the crystal structure consists of a single electronic spin per primitive cell. To generalize to structures with more than one spin per primitive cell, we need to introduce additional indices on S, $J(\omega, \boldsymbol{q})$, $\mathcal{A}(\boldsymbol{r})$, and $\chi''(\omega, \boldsymbol{q})$ to label different spins within the primitive cell.

2.1.3 Nuclear Spin-Spin Relaxation

A brief discussion of nuclear spin-spin relaxation and the time constant T_2 has been given following the discussion of the Bloch Eqs. (2.8). One simple mechanism for the T_2 process in solids is the dipole-dipole interaction between nuclear spins. The dipole-dipole interaction allows rapid energy transfer from one spin to another, leading to an internal thermal equilibrium state and a decay of the transverse magnetization. The relaxation rate due to this mechanism is of the order of[7]

$$1/T_2 \sim \frac{\gamma_{\rm n}^2 \hbar}{r^3}, \tag{2.16}$$

where r is the distance between nearest neighbor nuclei. Taking $\gamma_{\rm n} = 10.4$ kHz/G as for ^{7}Li nuclei and $r = 3$ Å, Eq. (2.16) yields $T_2 \sim 200$ μs.

Another mechanism for the nuclear *spin-spin* relaxation is the interaction with a fluctuating local magnetic field, which also leads to the nuclear *spin-lattice* relaxation. In the motional narrowing limit $(\langle h_z^2 \rangle)^{1/2} \gamma_{\rm n} \tau \ll 1$, where τ is the correlation time of longitudinal local fluctuating field h_z, the nuclear spin-spin relaxation rate due to this mechanism can be written as[7]

$$\frac{1}{T_2} = \frac{1}{2T_1} + \gamma_{\rm n}^2 \langle h_z^2 \rangle \tau, \tag{2.17}$$

where $1/T_1$ is given by Eq. (2.10).

A decrease of transverse magnetization with time can also be induced by the presence of static local field inhomogeneities. If the static local field inhomogeneity has magnitude ΔH_0, different nuclear spins have slightly different Larmor frequencies, which results in a phase mismatch of width $\Delta H_0 \gamma_n t$ if all spins have the same phase at $t = 0$. The net transverse magnetization decays with time with increasing phase mismatch. The relaxation time of transverse magnetization including all the above effects is often denoted by T_2^*, to distinguish it from T_2 that is defined as the intrinsic relaxation time without any field inhomogeneity effects.[8]

2.1.4 Nuclear Spin Susceptibility

When the nuclear spin system is subjected to a sufficiently weak RF excitation $H_x = 2H_1 \cos \omega t$ in addition to the strong field $H_z = H_0$, the magnetic response $M_x(t)$ to the RF

field may be assumed proportional to H_1, i.e.,

$$M_x(t) = 2H_1 \left[\chi'(\omega)\cos\omega t + \chi'' \sin\omega t\right], \tag{2.18}$$

where $\chi'(\omega)$ and $\chi''(\omega)$ are independent of H_1 and are called the real and imaginary parts of the nuclear magnetic susceptibility $\chi = \chi' - i\chi''$, respectively. According to Eq. (2.18), χ satisfies the relations

$$M_x = 2H_1 \mathrm{Re}\left\{\chi e^{i\omega t}\right\}, \text{ for } H_x = 2H_1 \mathrm{Re}\left\{e^{i\omega t}\right\} \tag{2.19}$$

and

$$M_x = 2H_1 \mathrm{Im}\left\{\chi e^{i\omega t}\right\}, \text{ for } H_x = 2H_1 \mathrm{Im}\left\{e^{i\omega t}\right\}, \tag{2.20}$$

where "Re" and "Im" stand for real and imaginary parts, respectively.

The macroscopic quantities χ' and χ'' can be related to the atomic properties of the system under study such as the wavefunctions, matrix elements, and energy levels . According to the electrodynamics, the average power absorbed by the nuclear spin system from the above RF field excitation $H_x = 2H_1 \cos\omega t$ is

$$\overline{P} = \frac{\omega}{2\pi}\int_0^{2\pi/\omega} H\frac{dM}{dt}dt = 2\omega\chi'' H_1^2. \tag{2.21}$$

On the other hand, a quantum mechanical treatment of the absorption process gives the following expression for the average absorption power (at $T \gg \hbar H_0\gamma_\mathrm{n}/k_\mathrm{B} \sim 1$ mK)[7]

$$\overline{P} = \frac{2\pi\hbar H_1^2\omega^2}{Zk_\mathrm{B}T}\sum_{a,b} e^{-E_a/k_\mathrm{B}T}|\langle a|\mu_x|b\rangle|^2\delta(E_a - E_b - \hbar\omega), \tag{2.22}$$

where E_a, E_b are the energy eigenvalues of the nuclear many-spin Hamiltonian with corresponding many-spin wave functions $|a\rangle$ and $|b\rangle$, $\mu_x = \gamma_\mathrm{n}\sum_i I_{ix}$ is the x-component of the total nuclear magnetization, and the nuclear spin partition function is $Z = \sum_a e^{-E_a/k_\mathrm{B}T}$. Comparing Eqs. (2.21) and (2.22), one has

$$\chi''(\omega) = \frac{\hbar\omega\pi}{Zk_\mathrm{B}T}\sum_{a,b} e^{-E_a/k_\mathrm{B}T}|\langle a|\mu_x|b\rangle|^2\delta(E_a - E_b - \hbar\omega). \tag{2.23}$$

The real part of χ, $\chi'(\omega)$, can be calculated from the Kramers-Kronig relation

$$\chi'(\omega) - \chi'(\infty) = \frac{1}{\pi}P\int_{-\infty}^{\infty}\frac{\chi''(\omega)}{\omega' - \omega}d\omega', \tag{2.24}$$

where the symbol P stands for taking the principal part of the integral, i.e., $P\int_{-\infty}^{\infty} = \int_{-\infty}^{\omega-R} + \int_{\omega+R}^{\infty}$ as $R \to 0$ simultaneously in the two integrals. Therefore, the real part is

$$\chi'(\omega) = \frac{\hbar\omega}{Zk_{\mathrm{B}}T} \sum_{a,b} e^{-E_a/k_{\mathrm{B}}T} |\langle a|\mu_x|b\rangle|^2 \frac{1}{E_a - E_b + \hbar\omega}. \tag{2.25}$$

2.1.5 Absorption Line Broadening

Measurements of the absorption spectrum $\chi''(\omega)$ can provide useful information about the interactions and local environments of the nuclear spin system. For a system consisting of isolated nuclear spins under a homogeneous external field, according to Eq. (2.23), the absorption line is very narrow since only transitions between neighboring nuclear Zeeman levels are allowed that all have the same energy separation $\hbar H\gamma_{\mathrm{n}}$. For a system of nuclear spins inside a solid, a number of physical phenomena may contribute to the broadening of the resonance line, which will be discussed in the following.

The most obvious origin of line broadening is the presence of magnetic field inhomogeneities. Such an inhomogeneity can arise either from the lack of homogeneity of the applied static magnetic field or a distribution of static local magnetic fields produced by polarized electronic magnetic moments in the sample. The broadening due to the inhomogeneity in applied magnetic field is of the order or less than 1 kHz for a 1 cm size sample, which is often negligible compared to the local field inhomogeneity and the nuclear dipolar broadening mechanisms discussed below. One can define a function $f(\omega)$ to describe the shape of the resonance line

$$f(\omega) = \frac{\pi}{Z} \sum_{a,b} e^{-E_a/k_{\mathrm{B}}T} |\langle a|\mu_x|b\rangle|^2 \delta(E_a - E_b - \hbar\omega) = k_{\mathrm{B}}T \frac{\chi''}{\hbar\omega}. \tag{2.26}$$

The function $f(\omega)$ is proportional to the distribution of local fields $P(\delta H) \propto f(H_0\gamma_{\mathrm{n}} + \delta H\gamma_{\mathrm{n}})$, since the number of neighboring Zeeman level pairs in the above sum contributing to a given ω value is proportional to the number of nuclear spins experiencing a total magnetic field $H_0 + \delta H = \omega/\gamma_{\mathrm{n}}$.

Another common broadening mechanism in solids is the magnetic dipole-dipole coupling between nuclear spin moments. The nuclear moments induce magnetic dipolar fields at their neighboring nuclear sites. Since such small fields can either aid or oppose the static field H_0,

a spread in the resonance condition results. One can define the second moment (mean square deviation) of $f(\omega)$ as

$$\langle \Delta\omega^2 \rangle = \frac{\int_0^\infty (\omega - \langle\omega\rangle)^2 f(\omega) d\omega}{\int_0^\infty f(\omega) d\omega}, \tag{2.27}$$

where $\langle\omega\rangle = \int_0^\infty \omega f(\omega) d\omega / \int_0^\infty f(\omega) d\omega$ is the average frequency of resonance. For nuclear dipolar broadening $\langle\omega\rangle = H_0\gamma_n$, i.e., the nuclear dipolar interactions do not introduce an overall shift of the resonance line.

For coupling between identical nuclear spins I,[9] the second moment $\langle \Delta\omega^2 \rangle_{II}$ of the absorption spectrum is

$$\langle \Delta\omega^2 \rangle_{II} = \frac{3}{4}\gamma_I^4 \hbar^2 I(I+1) \sum_k \frac{(1 - 3\cos^2\theta_{jk})^2}{r_{jk}^6}, \tag{2.28}$$

where γ_I is the gyromagnetic ratio of a spin I, $\boldsymbol{r}_{jk}$ is the vector from nucleus j to nucleus k, θ_{jk} is the angle between $\boldsymbol{r}_{jk}$ and the applied magnetic field, and the summation runs over all nuclear sites with $k \neq j$. For coupling between two different types of nuclear spins (with spins I and S), the second moment $\langle \Delta\omega^2 \rangle_{IS}$ for spin I is given by[9]

$$\langle \Delta\omega^2 \rangle_{IS} = \frac{1}{3N}\gamma_I^2 \gamma_S^2 \hbar^2 S(S+1) \sum_{j,k} \frac{(1 - 3\cos^2\theta_{jk})^2}{r_{jk}^6}, \tag{2.29}$$

where N is the total number of spins I in the system, γ_S is the gyromagnetic ratio of spins S, and $\sum_j$ and $\sum_k$ run over all I and S spin sites, respectively.[9]

There are other mechanisms that can cause the broadening of the resonance line. The T_1 processes produce a thermal equilibrium population of the nuclear spin system by balancing the rates of transitions between different Zeeman levels. Such processes put a limit on the lifetime of the Zeeman states, which effectively broadens the resonance lines by an energy of the order of $\hbar/T_1$. Furthermore, nuclear spins with spin quantum number $I > 1/2$ possess a nonvanishing electric quadrupole moment. The presence of a nonzero electric field gradient (EFG) on the nuclear site can lift the degeneracy of the resonance frequencies between adjacent Zeeman levels, giving rise to either resolved or unresolved splittings of the resonance lines. The latter effectively broaden the line. A more detailed discussion of nuclear quadrupole splitting is given in the next subsection.

2.1.6 Electric Quadrupole Interaction

Classically, the interaction energy of a nucleus [with charge density $\rho(\boldsymbol{r})$] with an electric potential V due to its surrounding electrons and nuclei is

$$\begin{aligned} E &= \int \rho(\boldsymbol{r}) V(\boldsymbol{r}) d^3\boldsymbol{r} \\ &= V(0) \int \rho d^3\boldsymbol{r} + \sum_\alpha V_\alpha \int x_\alpha \rho d^3\boldsymbol{r} + \frac{1}{2} \sum_{\alpha,\beta} V_{\alpha\beta} \int x_\alpha x_\beta \rho d^3\boldsymbol{r} \cdots, \end{aligned} \tag{2.30}$$

where $V_\alpha \equiv \partial V/\partial x_\alpha|_{\boldsymbol{r}=0}$, the electric field gradient tensor (at the nuclear mass center) is $V_{\alpha\beta} \equiv \partial^2 V/\partial x_\alpha \partial x_\beta|_{\boldsymbol{r}=0}$, the origin is chosen at the mass center of the nucleus, and x_α ($\alpha = 1, 2, 3$) stands for x, y, or z, respectively. The first term is the electrostatic energy of the nucleus taken as a point charge. The second term is the interaction energy of an electric dipole moment with an external electric field. It vanishes since the electric dipole moment of a nucleus is zero.[7] The third term is the electric quadrupole term. By Laplace's equation, one has $V_{xx} + V_{yy} + V_{zz} = 0$. One can always find principal axes of $V_{\alpha\beta}$ such that $V_{\alpha\beta} = 0$ if $\alpha \neq \beta$. In a quantum mechanical treatment,[7] the electric quadrupole interaction is described by the following Hamiltonian

$$\mathcal{H}_Q = \frac{e^2 qQ}{4I(2I-1)} \left[3I_z^2 + \frac{\eta}{2}(I_+^2 + I_-^2) - I(I+1) \right], \tag{2.31}$$

where e is the electron charge, $eq = V_{zz}$, $\eta = (V_{xx} - V_{yy})/V_{zz}$, $I_\pm = I_x \pm iI_y$, Q is the electric quadrupole moment of the nucleus, and x, y, z axes are parallel to the principal axes. It is conventional to choose x, y, and z in such a way that $|V_{zz}| \geq |V_{yy}| \geq |V_{xx}|$ and $0 \leq \eta \leq 1$.

In the presence of a strong applied magnetic field, $\mathcal{H}_Q$ in Eq. (2.31) can be treated by the perturbation method. For simplicity, let us assume that the EFG possesses an axial symmetry such that $\eta = 0$. In first order perturbation theory, the energies of different Zeeman levels is given by [7]

$$E_m = -\gamma_{\rm n} \hbar H_0 m + \frac{e^2 qQ}{4I(2I-1)} \left(\frac{3\cos^2\theta - 1}{2} \right) [3m^2 - I(I+1)], \tag{2.32}$$

where θ is the angle between the z axis and the quantization axis z' (along the direction of the external field). The shift of the resonance frequency between $I_z' = |m\rangle$ and $|m-1\rangle$ due to the

electric quadrupole effect is

$$\delta\nu_m^{(1)} = -\nu_Q \left(m - \frac{1}{2}\right) \frac{3\cos^2\theta - 1}{2}, \tag{2.33}$$

where

$$\nu_Q = \frac{3e^2qQ}{4\pi\hbar I(2I-1)}. \tag{2.34}$$

From Eq. (2.33), the frequency of the central line $|1/2\rangle \leftrightarrow |-1/2\rangle$ is not affected by the quadrupole interaction to first order. However, the central line is affected if the perturbation is carried out to second order. To second order, the frequency shift of the central line is given by[10]

$$\delta\nu_{\frac{1}{2}}^{(2)} = -\frac{\nu_Q^2}{16\nu_L}\left[I(I+1) - \frac{3}{4}\right](1-\cos^2\theta)(9\cos^2\theta - 1), \tag{2.35}$$

where $\nu_L = H_0\gamma_\mathrm{n}/2\pi$. The second order frequency shift is inversely proportional to the external field, so its effect is larger at lower fields.

2.1.7 Relaxation and Knight Shift in Metals

In a metal, the dominant mechanism for nuclear spin-lattice relaxation is provided by the coupling of nuclear spins to the spin magnetic moments of the conduction electrons. For metals with a substantial s-character to the wave function at the Fermi surface, the dominant coupling comes from the s-state contact interaction between the nuclear and electronic spins

$$\mathcal{H}' = \frac{8\pi}{3}\gamma_\mathrm{e}\gamma_\mathrm{n}\hbar^2 \sum_i \boldsymbol{I}\cdot\boldsymbol{S}_i\delta(\boldsymbol{r}_i), \tag{2.36}$$

where γ_e is the gyromagnetic ratio of electronic spins.

In order to calculate the nuclear spin lattice relaxation rate due to the above interaction, one needs to calculate the rates of induced transitions between adjacent Zeeman levels

$$W_{m\to m-1} = \sum_{\boldsymbol{k}s,\boldsymbol{k}'s'} W_{m\boldsymbol{k}s\to m-1\boldsymbol{k}'s'} f(E_{\boldsymbol{k}s})[1 - f(E_{\boldsymbol{k}'s'})], \tag{2.37}$$

where $\boldsymbol{k}$ and s denote the electronic spatial and spin quantum numbers, $E_{\boldsymbol{k}s}$ is the energy of a electron in such a state, $f(E)$ is the Fermi function, and $W_{m\boldsymbol{k}s\to m-1\boldsymbol{k}'s'}$ is the transition rate

from initial state $|m\boldsymbol{k}s\rangle$ to final state $|m-1\boldsymbol{k'}s'\rangle$. $W_{m\boldsymbol{k}s\to m-1\boldsymbol{k'}s'}$ is given from Fermi's golden rule by

$$W_{m\boldsymbol{k}s\to m-1\boldsymbol{k'}s'} = \frac{2\pi}{\hbar}|\langle m\boldsymbol{k}s|\mathcal{H}'|m-1\boldsymbol{k'}s'\rangle|^2\delta(E_m + E_{\boldsymbol{k}s} - E_{m-1} - E_{\boldsymbol{k'}s'}). \tag{2.38}$$

Due to the presence of the factor $f(E_{\boldsymbol{k}s})[1-f(E_{\boldsymbol{k'}s'})]$ in Eq. (2.37), only electrons close to the Fermi surface make significant contributions to the summation. A detailed calculation of Eq. (2.37) gives

$$1/T_1 = \frac{W_{m\to m-1}}{(I-m+1)(I+m)} = \frac{64}{9}\pi^3\hbar^3\gamma_{\rm e}^2\gamma_{\rm n}^2\langle|u_k(0)|^2\rangle_{E_{\rm F}}^2\rho^2(E_{\rm F})k_{\rm B}T, \tag{2.39}$$

where the first equality is the same as Eq. (2.9), $\rho(E_{\rm F})$ is the density of states at the Fermi energy for one spin direction, $|u_{\boldsymbol{k}}(0)|^2$ is the probability density of finding an electron with wave vector $\boldsymbol{k}$ at the nuclear site, and $\langle\cdots\rangle_{E_{\rm F}}$ means an average over the Fermi surface.[7]

In addition to dominating the nuclear spin lattice relaxation, the contact interaction also gives rise to a shift of the nuclear resonance frequency. Since the shift is proportional to the external magnetic field, one defines a field independent quantity called the Knight shift[11]

$$K \equiv \frac{\nu_{\rm m}-\nu_{\rm d}}{\nu_{\rm d}}, \tag{2.40}$$

where $\nu_{\rm m}$ and $\nu_{\rm d}$ are NMR frequencies in a metal and a diamagnetic substance, respectively.

The Knight shift is proportional to the difference in the energy of the contact interaction when the nuclear spin is in two adjacent Zeeman levels. Such an energy difference gives rise to an effective field for the nuclear spin that shifts its resonance frequency. The interaction energy can be calculated in first order perturbation approach by $E_{\rm en} = \langle\phi|\mathcal{H}'|\phi\rangle$, where $|\phi\rangle$ denotes the state of the combined electronic and nuclear system. After taking the thermal average of all states of the electronic system (assuming it is not affected by the state of the nuclear spins), one obtains

$$E_{\rm en} = -\gamma_{\rm n}\hbar m\left[\frac{8\pi}{3}\langle|u_k(0)|^2\rangle_{E_{\rm F}}\chi_{\rm e}^{\rm s}H_0\right] \tag{2.41}$$

if the nuclear spin is in the $I_z = |m\rangle$ state. In the above equation, $\chi_{\rm e}^{\rm s}$ is the spin susceptibility of the electronic spin system. The term inside the brackets in Eq. (2.41) corresponds to the

effective field on the nuclear site, so the Knight shift is

$$K = \frac{\Delta H}{H_0} = \frac{8\pi}{3}\langle|u_k^2(0)|\rangle_{E_\mathrm{F}}\chi_\mathrm{e}^\mathrm{s}. \tag{2.42}$$

For a Fermi gas of noninteracting spins, $\chi_\mathrm{e}^\mathrm{s} = \frac{1}{2}\gamma_\mathrm{e}^2\hbar^2\rho(E_\mathrm{F}) = \frac{1}{2}g^2\mu_\mathrm{B}^2\rho(E_\mathrm{F})$, where $g \approx 2.00$ is the spectroscopic splitting factor (g-factor) of the electron spin and μ_B is the Bohr magneton, so from Eqs. (2.39) and (2.42), one obtains the Korringa relation[12]

$$K^2T_1T = \frac{\hbar}{4\pi k_\mathrm{B}}\frac{\gamma_\mathrm{e}^2}{\gamma_\mathrm{n}^2} \equiv S, \tag{2.43}$$

where the second equality defines the constant S. The quantity K^2T_1T/S is called the Korringa ratio. In the heavy fermion compound LiV_2O_4, the Korringa ratio is equal to 0.7,[13] close to the value of unity expected for a Fermi gas/liquid system.

2.2 NMR Experiments

2.2.1 Free Induction Decay and Spin Echo

In Sec. 2.1.1, we briefly discussed the pulsed NMR method, in which the nuclear magnetization can be tilted with RF pulses in order to observe a nuclear induction signal. The most simple technique to produce such an induction signal is by applying only one RF pulse at resonance with the Larmor precession of the nuclear spins. The induced NMR signal by such a pulse is called free induction decay (FID). At resonance, Eq. (2.6) reduces to

$$\frac{\delta \boldsymbol{M}}{\delta t} = \gamma_\mathrm{n}\boldsymbol{M} \times H_1\hat{\boldsymbol{i}}', \tag{2.44}$$

where the nuclear magnetization is initially at thermal equilibrium with the lattice and points along the direction of the external field $\boldsymbol{H}_0$ before the RF field is applied. In the presence of an RF field, Eq. (2.44) describes the Larmor precession of the nuclear magnetization $\boldsymbol{M}$ with angular frequency $H_1\gamma_\mathrm{n}$ in the rotating frame. If the RF pulse has a duration of $t_\omega = \pi/(2H_1\gamma_\mathrm{n})$, then $\boldsymbol{M}$ lies along the y' direction at the end of the pulse. Such a pulse is called a $\pi/2$ pulse. In the lab frame, M precesses around the external field $H_0\hat{\boldsymbol{k}}$ after the H_1 field is removed. Thus an RF voltage signal will be induced in a coil with its axis parallel to x-y

plane surrounding the nuclear spin system under study. The signal decays as the transverse magnetization M relaxes back to the thermal equilibrium value $M_x = M_y = 0$. As discussed in Sec. 2.1.3, the time scale for the relaxation of transverse magnetization is called T_2^*, which includes dephasing contributions from nuclear spin-spin interactions, local field fluctuations, and static field inhomogeneities.

The dephasing due to static field inhomogeneity can be compensated using the spin echo technique.[14] The idea of a spin echo formation is illustrated in Fig. 2.1. The equilibrium magnetization is shown in Fig. 2.1(a). After application of a $\pi/2$ pulse along the x' direction [denoted by $(\pi/2)_{x'}$ in Fig. 2.1(f)] at $t = 0$ in Fig. 2.1(b), the precession phases of some of the spins start getting ahead of the average and some start getting behind due to a slight difference in their Larmor frequencies, as shown in Fig. 2.1(c). As a result, the net transverse magnetization decays as the nuclear spins fan out in the x'-y' plane. Now a second RF pulse is applied along the x' direction at time $t = \tau$. The duration of the second pulse is twice that of a $\pi/2$ pulse (called a π pulse), so the spin directions are rotated by 180° around the x' axis, as shown in Fig. 2.1(d). After the second pulse, spins which had gotten ahead of the average phase are now behind the average by the same amount. Similarly, those spins which were behind the average are now ahead of the average by the same amount. Therefore, the spins start to refocus and at time $t = 2\tau$, all the spins are again in phase with each other, as shown in Fig. 2.1(e). This results in an echo signal being observed, centered at $t = 2\tau$, that consists of the refocusing and dephasing signals back to back, as shown in Fig. 2.1(f).

2.2.2 Measurement of the Spectrum with Pulsed NMR

For a linear system, the response $F(t)$ of the system due to an external excitation $i(t)$ is given by

$$F(t) = \int_{-\infty}^{\infty} S(t - t')i(t')dt', \tag{2.45}$$

where $S(t)$ is called the response function of the system and $S(t < 0) = 0$ in order to preserve causality. The Fourier transform $\tilde{f}(\omega) = \int_{-\infty}^{\infty} f(t)e^{-i\omega t}dt$ on both sides of the equation yields $\tilde{F}(\omega) = \tilde{S}(\omega)\tilde{i}(\omega)$, which can be rewritten as $\tilde{S}(\omega) = \tilde{F}(\omega)/\tilde{i}(\omega)$. If the excitation is a Dirac

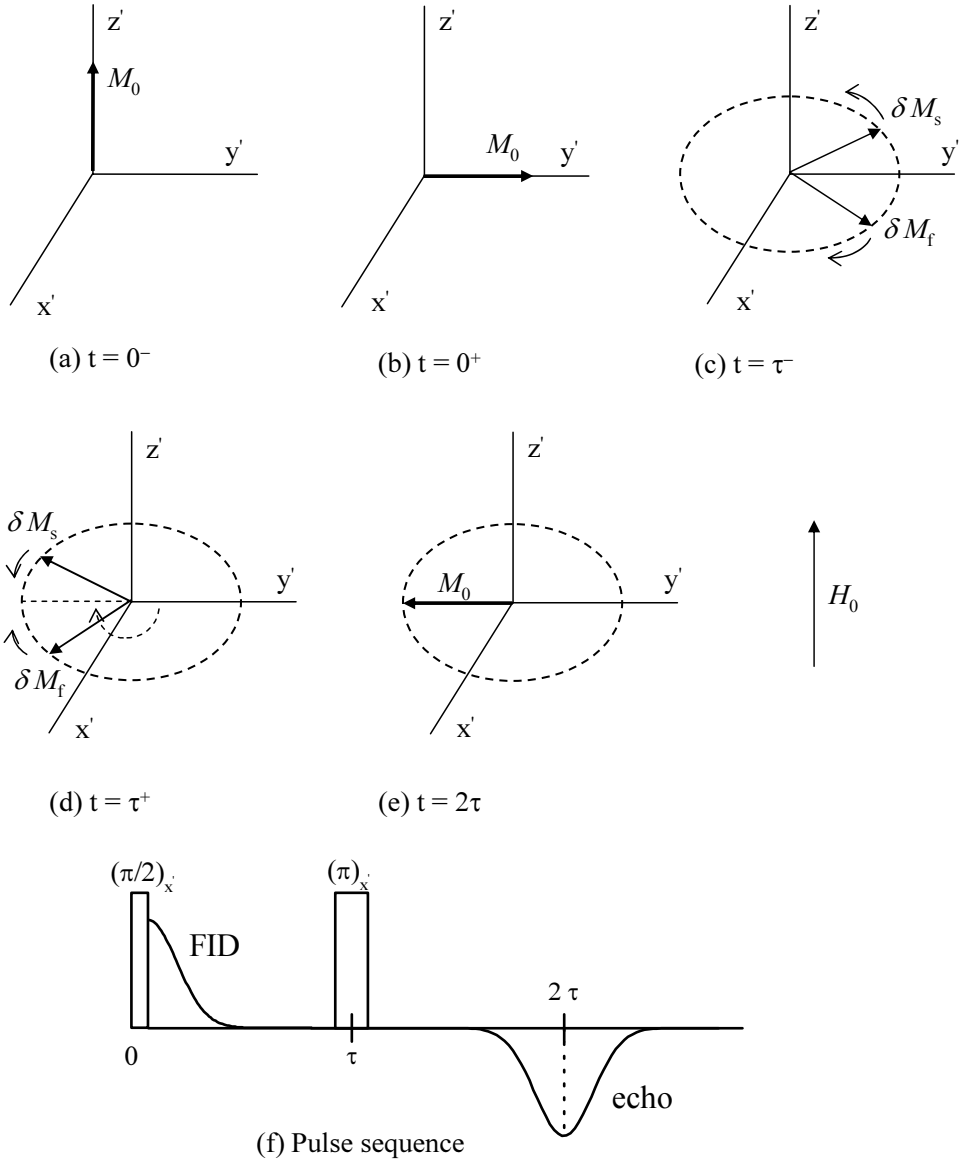

Figure 2.1 Formation of free induction decay and Hahn echo in the rotating coordinate system, as explained in the text. (After Ref. [7]) Panel (f) shows the pulse sequence and the induced free induction decay (FID) and echo signals following the first and second pulses, respectively. The subscripts on the parentheses give the directions of the $\boldsymbol{H}_1$ fields in the x'-y' plane. The echo consists of the refocusing and dephasing signals back to back.

delta function $i(t) = h\delta(t)$, then $\tilde{i}(\omega) = h$ and $\tilde{S}(\omega) = \tilde{F}(\omega)/h$. Thus the Fourier transform of the system response to a delta function directly gives the response spectrum of the system.

An RF pulse $\boldsymbol{H_1}(t) = 2H_1\hat{\boldsymbol{i}}\cos\omega t$ perpendicular to the external magnetic field $H_0\hat{\boldsymbol{k}}$ approximates a delta function under the condition $\gamma_{\rm n}H_1 \gg \Delta\omega$ and $\gamma_{\rm n}H_1 \gg |\omega - \omega_0|$, where ω_0 and $\Delta\omega$ are the center and width of the NMR absorption spectrum, respectively.[7] Therefore, the real and imaginary parts of the Fourier transform of the FID signal induced by such a pulse gives directly the dispersion and absorption spectrum of the system, respectively. In practice, we only use absorption spectrum. In NMR experiments utilizing a single coil for both RF power transmission and NMR signal detection, the initial part of an FID signal often cannot be measured as a result of a "dead time" of the NMR spectrometer immediately after the application of the RF pulse. The "dead time" is the result of the saturation of the receiver due to the strong rf pulse and the finite time necessary for the receiver to become operational again. Such a problem can often be circumvented by creating an echo as described above, and performing a Fourier transform on the second (latter) half of the echo signal. The echo appears after delay τ following the second pulse, so the effect of the "dead time" can be avoided. This is one reason that the 2-pulse sequence in Fig. 2.1 is used to produce echos.

For very wide and inhomogeneously broadened lines, the condition $\gamma_{\rm n}H_1 \gg \Delta\omega$ cannot be satisfied. In addition, the spectral width can exceed the response window of the NMR spectrometer due to the high-Q factor of the resonant circuit and as a result the FID and echo signals will be distorted. In this case, one can resort to a pulsed NMR technique called spin echo integration spectroscopy (SEIS), in which one measures and plots the area of the spin echo as a function of the applied magnetic field. In order to avoid distortion of the measured spectrum, the step of field sweep must be small compared to the width in magnetic field of any features of the spectrum to be recorded.[15] A variant of SEIS in which one sweeps the frequency is sometimes used to record NMR spectra when the field sweep is not possible. However, frequency sweep has the disadvantage that the response of the NMR spectrometer changes with measuring frequency. A more sensitive and efficient way to measure a wide NMR spectrum is the frequency step and sum (FSS) method, in which the transient echo signal at a

series of equally spaced magnetic fields are recorded, then their Fourier transforms are summed after shifting the frequency of each Fourier transform by the corresponding field shift.[15] All wide line spectra in this thesis were obtained by the SEIS method with either field or frequency sweep.

2.2.3 Measurement of T_2

The nuclear spin-spin relaxation time T_2 can be measured using the RF pulse sequence

$$\left(\frac{\pi}{2}\right) - \tau - (\pi) - \tau - \text{echo}$$

with a series of pulse separation τ values. Since the dephasing of the magnetization due to the static field inhomogeneity completely refocuses at time $t = 2\tau$, the decay of echo intensity versus 2τ reflects the intrinsic decay of the transverse magnetization. If the echo intensity $M(t)$ with $t = 2\tau$ follows an exponential decay, then a single T_2 value can be extracted from fitting the $M(t)$ data by the function $M(t) = M_0 \exp(-t/T_2)$. If $M(t)$ versus t $(= 2\tau)$ follows instead a half Gaussian as is often observed in solids, then T_2 can be defined as the time at which the echo decays to $1/e$ of its initial value. In such a case, T_2 can be extracted from fitting the $M(t)$ data by $M(t) = M_0 \exp[-(t/T_2)^2]$. In chapter 6 on the study of $(\text{Li}_x\text{V}_{1-x})_3\text{BO}_5$, the ^{7}Li nuclear spin-spin relaxation crosses over from a half Gaussian decay at high temperatures to a single exponential decay at low temperatures. In order to obtain a consistent description over the whole temperature range, we used the function $M(t) = M_0 \exp(-t/T_2) \exp[-(t/T_{2g})^2]$ to fit the experimental data.

2.2.4 Measurement of T_1

The nuclear spin lattice relaxation time can be measured by the so-called saturation recovery pulse sequence:

$$\underbrace{\left[\left(\frac{\pi}{2}\right) - \tau_1 - \left(\frac{\pi}{2}\right) - \tau_1 - \cdots\right]_{n-1} - \left(\frac{\pi}{2}\right)}_{\text{saturating comb pulses}} - \tau - \underbrace{\left(\frac{\pi}{2}\right) - \tau_2 - (\pi) - \tau_2 - \text{echo}}_{\text{reading pulses}},$$

where the saturating $\pi/2$ pulses are repeated n times with a separation of τ_1 between neighboring pulses. Immediately following the comb pulses, the longitudinal nuclear magnetization

initially equal to zero starts to recover for a time τ toward the thermal equilibrium value. The recovered magnetization at the end of period τ is monitored by the two reading pulses that produce an echo. The echo intensity is proportional to the recovered longitudinal magnetization right before the first reading pulse. The delay τ is varied in different runs of the above pulse sequence in order to map out the recovery curve of the echo intensity $M(t)$ (with $t = \tau$).

The above pulse sequence is useful to measure nuclear spin lattice relaxation rates of wide lines ($\gtrsim$ 100 kHz), for which a single $\pi/2$ pulse cannot completely saturate the whole line. In order to effectively saturate the whole line, the value of τ_1 should in principle satisfy $T_2 \lesssim \tau_1 \ll T_1$ so that the longitudinal nuclear magnetization does not have time to relax in the interval between neighboring pulses yet the nuclear spin system has time to establish an internal thermal equilibrium. The τ_2 value should be set as small as possible in order to maximize signal intensity as long as the "dead time" effect of the spectrometer can be avoided.

Depending on the shape of the recovery curve $M(t)$, one can fit $M(t)$ data with different functions to extract the relaxation rates. In order to see the recovery behavior more clearly and see if the initial conditions correspond to full saturation of the line, one often plots $1 - M(t)/M(\infty)$ in a semilog scale, in which a single exponential recovery shows a straight line. For a single exponential recovery, the following fitting function is used to extract T_1 values

$$1 - \frac{M(t)}{M(\infty)} = \exp(-t/T_1). \tag{2.46}$$

If a distribution of T_1 values exist in the system, then $1 - M(t)/M(\infty)$ deviates upwards from a straight line in a semilog scale plot. However, if the initial decay is sufficiently well defined so that one can derive a value for the initial slope, then one can use Eq. (2.46) to derive a single relaxation parameter. The $1/T_{1\,\mathrm{eff}}$ value thus obtained gives the average relaxation rates of all nuclear spins. In case the initial linear part is not well defined, one can often try to fit the recovery curve by a stretched exponential function

$$1 - \frac{M(t)}{M(\infty)} = \exp[-(t/T_1^*)^\beta] \tag{2.47}$$

with $0 < \beta \leq 1$. For a true stretched exponential decay, values of $1/T_1^*$ and β obtained from the fit allow us to obtain a unique distribution of $1/T_1$ values.[16, 17]

A nonexponential recovery of $M(t)$ also can arise in the presence of electric quadrupole interactions for nuclear spins with $I > 1/2$. The quadrupole interaction makes the energy differences between adjacent Zeeman levels unequal and thus splits the absorption line into $2I$ equally spaced lines, as discussed in Sec. 2.1.6. The inequality in energy spacing excludes the rapid first order spin-spin interaction as a way to establish a common spin temperature in the nuclear spin system,[18] where each nuclear spin relaxes towards its equilibrium value with the same time dependence as for other nuclei. In the absence of a common spin temperature, the spin-lattice relaxation is in general not characterized by a single relaxation time. The behavior of the relaxation arising from any general nuclear spin-lattice interaction can be obtained by solving the $2I$ rate (master) equations, which determines the evolution with time of the differences in populations between adjacent Zeeman levels, and is described in general by $2I$ relaxation times. The final solution of the rate equations depends on the nature of the relaxation process and on the initial conditions.[19] Below we will only consider the case where the relaxation transition probability W is of magnetic origin with $\Delta m = \pm 1$. For quadrupole relaxation which involves transitions also with $\Delta m = \pm 2$ the situation is different but this case will not be encountered in the present thesis.

Below we will only discuss the *magnetic* relaxation for nuclear spins with $I = 3/2$ since this is the only situation that we will encounter in this thesis. If the quadrupole splitting is small such that the whole spectrum can still be saturated by applying a number of saturation pulses, then the recovery of $M(t)$ measured from transitions between any adjacent Zeeman level pairs still follows a single exponential with $1/T_1$ given by Eq. (2.9). Therefore, for this initial condition, the relaxation is not affected by the presence of quadrupole splitting. This is the case, for example, for ^{7}Li NMR ($I = 3/2$) in LiV_2O_4 samples that are magnetically pure, and in $(Li_xV_{1-x})_3BO_5$ to be discussed in subsequent chapters. On the other hand, if the absorption spectrum is so wide that only the central $m = |-1/2\rangle \leftrightarrow |1/2\rangle$ line can be irradiated and a $\pi/2$ comb sequence is applied to saturate it, then two different initial conditions need to be considered. (i) The duration of the comb sequence is much shorter than $1/W$. The initial

population differences *per spin* between adjacent Zeeman levels are

$$a_{1/2,-1/2} = 0 \text{ and } a_{-1/2,-3/2} = a_{3/2,1/2} = \frac{\epsilon}{2}, \tag{2.48}$$

where $\epsilon = \gamma_{\rm n}\hbar H/k_{\rm B}T$ and $a_{m,m-1}$ is the population in level m minus the population in level $m-1$. (ii) The duration of the comb sequence is much longer than $1/W$. Then the latter two lines in Eq. (2.48) have time to go back to equilibrium with the lattice and the initial condition is given by

$$a_{1/2,-1/2} = 0 \text{ and } a_{-1/2,-3/2} = a_{3/2,1/2} = \frac{\epsilon}{3}.$$

The recovery curves in the two cases are respectively given by[19, 20]

$$\text{case (i): } 1 - \frac{M(t)}{M(\infty)} = 0.1\exp(-2Wt) + 0.9\exp(-12Wt) \tag{2.49}$$

$$\text{case (ii): } 1 - \frac{M(t)}{M(\infty)} = 0.4\exp(-2Wt) + 0.6\exp(-12Wt). \tag{2.50}$$

Here, there are two relaxation rates, instead of the three expected above from $2I = 3$, because the prefactor of the exponential for the third term is zero.

If the central line is narrow, then the central line can be saturated by a single $\pi/2$ pulse and case (i) is realized. On the other hand, for a strongly inhomogeneously broadened central line, one has to apply a number of saturation pulses in order to saturate the central line. In order to have a well defined initial condition, the saturation comb should last for a duration much longer than $1/W$ such that case (ii) is realized.

2.2.5 "Hole" Burning Experiment

In the saturation recovery pulse sequence introduced above, the magnetization of all the nuclear spins are saturated by the comb pulses, where by "saturation" we mean that the nuclear magnetization is tipped to an angle of 90° with respect to the applied field such that its component along the field direction is zero. For an inhomogeneously broadened line, it is also possible to saturate nuclear spins with resonance frequencies within a narrow frequency range of the spectrum. In the absence of nuclear spin spectral diffusion,[21] the NMR spectrum measured before those saturated spins relax back to thermal equilibrium with the lattice will

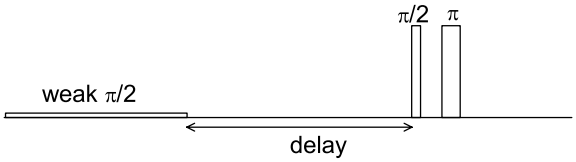

Figure 2.2 The pulse sequence for a "hole" burning experiment. A hole was produced in the spectrum by a weak $\pi/2$ pulse. After a delay, a $\pi/2$, π pulse sequence with much shorter pulse lengths is applied to generate an echo, from which the spectrum with a "hole" can be obtained by Fourier transform.

have a "hole" in the spectrum. A simple hole-burning RF pulse sequence is displayed in Fig. 2.2. A "hole" in the spectrum is produced by applying a weak and long $\pi/2$ pulse. For a rectangular RF pulse with pulse duration τ and frequency ν_0, the Fourier transform of the RF pulse is proportional to $\sin[(\nu-\nu_0)\tau\pi]/(\nu-\nu_0)$. Therefore, most of the power of the pulse is distributed within the frequency range from $\nu_0 - 1/\tau$ to $\nu_0 + 1/\tau$, and only spins within that frequency range are significantly saturated. To obtain the spectrum after burning the "hole", a $\pi/2$, π pulse sequence with much shorter pulse lengths than the weak hole burning pulse is applied to generate a Hahn echo signal and the spectrum with a "hole" is obtained from the Fourier transform of half the echo signal. Such short pulses are chosen because their power is distributed over a much broader frequency range so that nuclei from a much broader part of the spectrum can be excited and contribute to the echo signal. By varying the delay before the weak hole-generating $\pi/2$ pulse and the $\pi/2$, π echo-generating pulses, the "hole" recovery process can be monitored. In chapters 3 and 4, we will use such "hole" burning and recovery experiments on the ^{7}Li NMR spectra in LiV_2O_4 samples to study the effect of ^{7}Li nuclear spin spectral diffusion.

2.2.6 Experimental Errors

As discussed above, the nuclear spin-lattice relaxation rate $1/T_1$ and nuclear spin-spin relaxation rate $1/T_2$ are obtained by fitting the decay curves of the nuclear magnetization $M(t)$. The errors in $1/T_1$ and $1/T_2$ are dominated by the statistical error of $M(t)$, which is caused by the electrical noise and random fluctuation of the NMR spectrometer. The error

of $M(t)$ was estimated by the variation in $M(t)$ measured at different times under the same experimental condition. The error of $M(t)$ can be improved by summing the NMR signals from a large number of repetitions. In most cases, a sufficient number of repetitions were performed such that the relative error of the fully recovered nuclear magnetization is less than 1%. The errors of $1 - M(t)/M(\infty)$ used in T_1 measurements are calculated using the standard error propagation procedure. The errors are assumed to be independent for the data points at different t values. The errors of $1 - M(t)/M(\infty)$ or $M(t)$ are then used by the nonlinear least square fit program in calculating the errors in the fitted values of $1/T_1$ and $1/T_2$, respectively.

The broadening of NMR spectrum is often quantified by the full width at half maximum (FWHM) intensity of the absorption line. For narrow lines (FWHM $\lesssim$ 100 kHz), the spectrum is often conveniently measured by the Fourier transform of half the echo signal. However, the measured spectrum might still be distorted due to a variation of the spectrometer response at different frequencies and the uncertainty in defining the center of the echo. For broad lines (FWHM $\gtrsim$ 100 kHz) measured with frequency sweep, the error in the measured spectrum is mainly caused by the unknown response change of the spectrometer tuned at different frequencies. For a broad line measured with field sweep at fixed resonance frequency, the error in the measured spectrum is mainly caused by the error in the measurements of the magnetic field. In this thesis, the combined statistical and systematic relative error of the FWHM obtained from Fourier transform is estimated to be 5%. The relative error of the FWHM obtained from the frequency or field sweep is estimated to be 10%.

References

[1] F. Bloch, Phys. Rev. **70**, 460 (1946).

[2] F. Bloch, W. W. Hansen, and M. Packard, Phys. Rev. **70**, 474 (1946).

[3] N. Bloembergen, E. M. Purcell, and R. V. Pound, Phys. Rev. **73**, 679 (1948).

[4] T. Moriya, Prog. Theor. Phys. **16**, 23 (1956).

[5] R. M. White, *Quantum Theory of Magnetism* (McGraw-Hill, New York, 1970).

[6] F. Borsa and A. Rigamonti, in *Magnetic Resonance of Phase Transitions*, edited by F. J. Owens, C. P. Poole, and H. A. Farach (Academic Press, New York, 1979), p. 103.

[7] C. P. Slichter, *Principles of Magnetic Resonance* (Springer, Berlin, 1990), 3rd ed.

[8] E. Fukushima and S. B. W. Roeder, *Experimental Pulse NMR: A nuts and Bolts Approach* (Perseus Books, Cambridge, 1981).

[9] J. H. Van Vleck, Phys. Rev. **74**, 1168 (1948).

[10] A. Abragam, *Principles of Nuclear Magnetism* (Oxford University Press, Oxford, 1982).

[11] W. D. Knight, Phys. Rev. **76**, 1259 (1949).

[12] J. Korringa, Physica **16**, 601 (1950).

[13] A. V. Mahajan, R. Sala, E. Lee, F. Borsa, S. Kondo, and D. C. Johnston, Phys. Rev. B **57**, 8890 (1998).

[14] E. L. Hahn, Phys. Rev. **80**, 580 (1950).

[15] W. G. Clark, M. E. Hanson, F. Lefloch, and P. Ségransan, Rev. Sci. Instrum. **66**, 2453 (1995).

[16] D. C. Johnston, S.-H. Baek, X. Zong, F. Borsa, J. Schmalian, and S. Kondo, Phys. Rev. Lett. **95**, 176408 (2005).

[17] D. C. Johnston, Phys. Rev. B **74**, 184430 (2006).

[18] A. Abragam and W. G. Proctor, Phys. Rev. **109**, 1441 (1958).

[19] E. R. Andrew and D. P. Tunstall, Proc. Phys. Soc. London **78**, No. 499 (1961).

[20] S. H. Baek, B. J. Suh, E. Pavarini, F. Borsa, R. G. Barnes, S. L. Bud'ko, and P. C. Canfield, Phys. Rev. B **66**, 104510 (2002).

[21] N. Bloembergen, S. Shapiro, P. S. Pershan, and J. O. Artman, Phys. Rev. **114**, 445 (1959).

CHAPTER 3. Dynamics of Magnetic Defects in Heavy Fermion LiV_2O_4 from Stretched Exponential ^{7}Li NMR Relaxation

(This chapter is based on a paper published on Phys. Rev. Lett. by D. C. Johnston, S.-H. Baek, X. Zong, F. Borsa, J. Schmalian, and S. Kondo[1])

Abstract

^{7}Li NMR measurements on LiV_2O_4 from 0.5 to 4.2 K are reported. A small concentration of magnetic defects within the structure drastically changes the ^{7}Li nuclear magnetization relaxation versus time from a pure exponential as in pure LiV_2O_4 to a stretched exponential, indicating glassy behavior of the magnetic defects. The stretched exponential function is described as arising from a distribution of ^{7}Li nuclear spin-lattice relaxation rates and we present a model for the distribution in terms of the dynamics of the magnetic defects. Our results explain the origin of recent puzzling ^{7}Li NMR literature data on LiV_2O_4 and our model is likely applicable to other glassy systems.

Heavy fermion (HF, heavy Fermi liquid) behaviors have been widely observed at low temperatures T in many metals containing crystallographically ordered arrays of f-electron atoms, which are quite well understood theoretically [2]. In these metals, the current carriers act as if they have a (heavy) mass that is of order 10^2–10^3 times the free electron mass. Only a few d-electron compounds are known to show HF behaviors at low T, e.g. $Y_{1-x}Sc_xMn_2$ with $x \approx 0.03$ [3], LiV_2O_4 [4, 5], and most recently $Ca_{2-x}Sr_xRuO_4$ with $x \sim 0.3$–0.5 [6]. There is

currently no theoretical consensus on the mechanism for formation of the heavy fermion mass in LiV_2O_4 [7].

An important measurement for establishing Fermi liquid behavior at low T is nuclear magnetic resonance (NMR). For high magnetic purity samples of LiV_2O_4, the ^{7}Li nuclear spin-lattice relaxation rate $1/T_1$ is proportional to T (the Korringa law for a Fermi liquid) from about 10 K down to about 1.5 K [4, 8, 9]. In contrast to these results, recent ^{7}Li NMR measurements of several samples down to 30 mK by Trinkl, Kaps et al. strongly conflict with a Fermi liquid interpretation [10, 11]. In particular, non-exponential (stretched exponential) recovery of the nuclear magnetization, non-Korringa behavior in $1/T_1$ versus T, a peak in $1/T_1$ at ~ 0.6 K, and a strong field dependence of $1/T_1$ were found at low T. In view of the small number of known d-electron HF compounds and the importance of LiV_2O_4 within this small family, it is critical to determine if these results are intrinsic to the pure material, and if not, what they are due to.

Here we present ^{7}Li NMR measurements on two samples from 0.5 to 4.2 K that were carried out to study the influence of magnetic defects on the low-T HF properties of LiV_2O_4. We confirmed Fermi liquid behavior down to 0.5 K in a high magnetic purity sample. We find that a small concentration (0.7 mol%) of magnetic defects within the spinel structure drastically changes the detected spin dynamics and leads to the above behaviors described in Refs. [10] and [11], which therefore explain their results as arising from a significant concentration of magnetic defects in their samples. On the other hand, understanding the physics of magnetic defects in LiV_2O_4 is interesting and important in its own right and may further guide and constrain theoretical models for the pure material. A crucial aspect of LiV_2O_4 is the geometric frustration of V spins for antiferromagnetic ordering in the spinel structure. The geometric frustration is likely directly related to the suppression of antiferromagnetic order in pure LiV_2O_4 and the emergence of a heavy electron state instead. A large number of low lying spin excitations emerges and the system becomes "almost unstable", i.e. very susceptible with respect to crystal defects or other perturbations that locally lift the frustration and cause a condensation of the low lying states [12].

We develop a phenomenological description for the observed stretched exponential ^{7}Li nuclear relaxation in terms of a distribution of $1/T_1$ values and explain the physical meaning of the parameters. We further present a model for defect nucleated dynamical magnetic order in an almost unstable electronic system that can explain this distribution and that provides important insights about the behaviors of magnetic defects in LiV_2O_4. The stretched exponential function also describes the kinetics of diverse relaxation phenomena [13], so our model will likely have many applications to other fields.

The two LiV_2O_4 samples measured here were samples #12-1 and #3-3-a2 studied previously in Ref. [14], where their synthesis and characterization were described. The magnetic defect concentration $n_{\rm defect}$ in the two samples was previously estimated from magnetization measurements at low T [14]. Sample #12-1 shows a clear but weak intrinsic broad maximum in $\chi(T)$ at 16 K, characteristic of high magnetic purity [4, 14], with only a tiny upturn in $\chi(T)$ below 4 K corresponding to $n_{\rm defect} = 0.01$ mol%. The second sample, #3-3-a2, has $n_{\rm defect} = 0.7$ mol% which is sufficiently large that the low-T intrinsic broad maximum in $\chi(T)$ is completely masked by the magnetic defect Curie-like term[14]. The ^{7}Li NMR measurements were performed with a Fourier transform (FT) TecMag pulse spectrometer using ^{4}He (1.5–4.2 K) and ^{3}He (0.5–1.5 K) cryostats. The ^{7}Li NMR lineshape and the full width at half maximum (FWHM) were obtained from the FT of half of the echo signal. The ^{7}Li $1/T_1$ was determined by monitoring the recovery of the spin echo intensity following a saturating pulse sequence of $\pi/2$ pulses. The typical $\pi/2$ pulse width was 2 μs. The measurements were carried out at a frequency of 17.6 MHz (magnetic field $H = 10.6$ kOe) so that a direct comparison of our results with the corresponding ^{7}Li NMR data at 17.3 MHz in Refs. [10] and [11] could be made.

The resonance line for the pure sample #12-1 has a FWHM that is independent of T below 4.2 K whereas sample #3-3-a2 has a much broader line [Fig. 1(a)] that becomes increasingly broad with decreasing T [inset, Fig. 1(a)], indicating an increasing importance of magnetic inhomogeneity in the latter sample with decreasing T. The Knight shift K for both samples is the same and independent of T between 0.5 and 4.2 K, with $K = 0.141(15)\%$ in agreement with previous data [8] above 1.5 K.

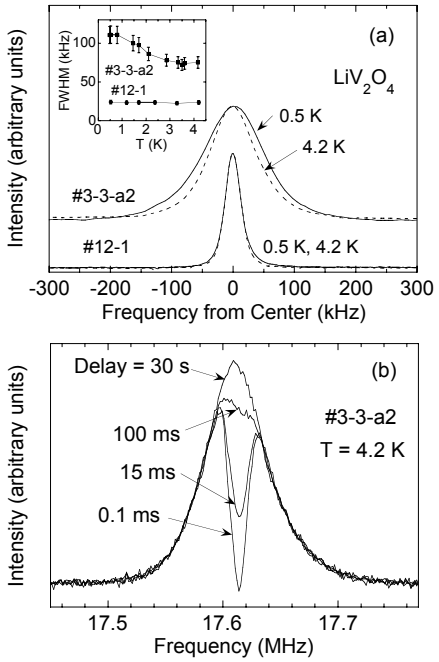

Figure 3.1 (a) ^{7}Li NMR lineshape at 0.5 and 4.2 K and full width at half maximum peak intensity versus temperature (FWHM, inset) for two samples of LiV_2O_4. (b) Hole-burning spectra at 4.2 K for sample #3-3-a2.

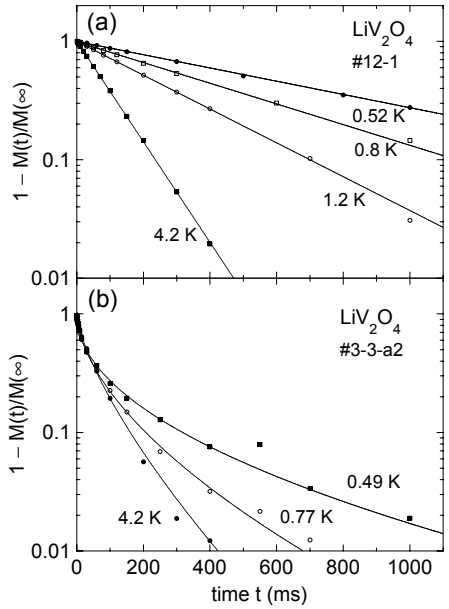

Figure 3.2 Recovery of the ^{7}Li nuclear magnetization M vs time t for LiV_2O_4 samples #12-1 (a) and #3-3-a2 (b). The solid curves in (a) and (b) are fits to the data at each T by an exponential and a stretched exponential, respectively.

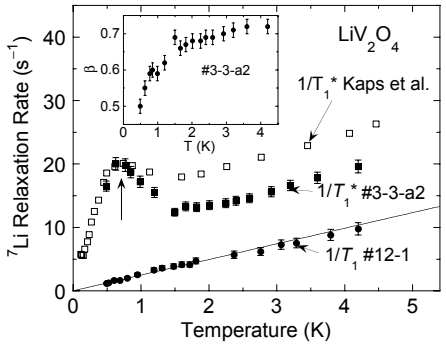

Figure 3.3 ^{7}Li nuclear spin-lattice relaxation rates in LiV_2O_4 vs temperature T. The lowest data set of $1/T_1$ vs T is for high purity sample #12-1; the fitted straight line is the Korringa law for a Fermi liquid. The $1/T_1^*$ vs T data sets are for our sample #3-3-a2 (filled squares) and from Kaps et al. (Ref. [11]) (open squares). The vertical arrow at about 0.7 K indicates the approximate T of the maxima in $1/T_1^*$. The inset shows the exponent β in the stretched exponential in Eq. (1) vs T.

Our main experimental results originate from measurements of the influence of magnetic defects on the ^{7}Li nuclear spin dynamics of LiV_2O_4. Figure 2(a) shows representative semilog plots of the time t dependent recovery of the ^{7}Li nuclear magnetization $M(t)$ after initial saturation for magnetically pure sample #12-1 at several T. The data at each T lie on a straight line (shown) with a well-defined $1/T_1$ determined from a fit of the data by $1-M(t)/M(\infty) = A\exp(-t/T_1)$, where the prefactor A is typically 0.9 to 1.1. The resulting $1/T_1$ is plotted vs T in Fig. 3. These data follow the Korringa law for a Fermi liquid ($1/T_1 \propto T$) with a weighted fit giving $(T_1T)^{-1} = 2.46(6)\mathrm{s}^{-1}\mathrm{K}^{-1}$. Our results thus further confirm Fermi liquid behavior for pure LiV_2O_4 at low T.

The $M(t)$ for sample #3-3-a2 with $n_{\mathrm{defect}} = 0.7$ mol% is shown for representative temperatures in Fig. 2(b). The recovery is drastically different from that of the pure sample, exhibiting strongly non-exponential behavior. Another important feature is that the shape of the recovery curve changes with decreasing T, particularly strongly below 1 K. Following Ref. [11], we fitted the data at each T by the stretched exponential function

$$1 - \frac{M(t)}{M(\infty)} = \exp[-(t/T_1^*)^{\beta}], \tag{3.1}$$

where β is the stretching exponent with $0 < \beta \leq 1$ and $1/T_1^*$ is a characteristic relaxation rate.

This function is nonanalytic for $t \to 0$. We therefore employed a low-t cutoff at 15 ms to the fit. The resulting $1/T_1^*(T)$ is plotted as filled squares in Fig. 3 and the fits are shown by the solid curves in Fig. 2(b). The variation of β with T is shown in the inset of Fig. 3. The ^{7}Li NMR $1/T_1^*$ data obtained at 17.3 MHz by Kaps et al. [11] are plotted vs T as open squares in Fig. 3. From the totality of the data in Figs. 1–3, we conclude that the data of Kaps et al. are not intrinsic to pure LiV_2O_4 but rather are dominated by the influence of magnetic defects.

The non-exponential recovery of $M(t)$ in sample #3-3-a2 suggests that there is a distribution of $1/T_1$ values in this sample for different ^{7}Li nuclei. To check this hypothesis, we performed relaxation measurements in different regions of the NMR spectrum. These are shown in Fig. 1(b) as "hole-burning" experiments. By using a long saturating $\pi/2$ pulse we can irradiate only the central part of the spectrum. The fact that the "hole" disappears gradually during relaxation without affecting the remaining part of the line shape indicates the absence of spectral diffusion, which means that ^{7}Li nuclei with different Larmor frequencies have no thermal contact over our time scale. Another experiment was done by monitoring the recovery of the part of the echo signal far from $t = 0$. The recovery was found to be nearly exponential and with a $1/T_1$ corresponding to the long time tail of the stretched exponential in Fig. 2(b). These two experiments together demonstrate that there does exist a distribution of $1/T_1$ values for the ^{7}Li nuclei in the sample at each T on our time scale and that these nuclei or groups of nuclei relax independently. The strong decrease of β with decreasing T in the inset of Fig. 3 must therefore reflect a significant change in the distribution of $1/T_1$ values with T as discussed next.

Our experiments thus demand that we model the stretched exponential relaxation in Eq. (1) as the sum over the sample of a probability distribution P of $1/T_1$ for the various ^{7}Li nuclei. Accordingly we write the stretched exponential function in Eq. (1) as

$$e^{-(t/T_1^*)^\beta} = \int_0^\infty P(s,\beta) e^{-st/T_1^*} ds \ , \tag{3.2}$$

where $s = T_1^*/T_1$ is the ratio of a particular relaxation rate $1/T_1$ within the sample to the fixed relaxation rate $1/T_1^*$ characteristic of $P(s,\beta)$, and of course $\int_0^\infty P(s,\beta) ds = 1$. For $\beta = 1$, $P(s,1)$ is the Dirac delta function at $s = 1$. For general β, Eq. (2) shows that $P(s,\beta)$ is

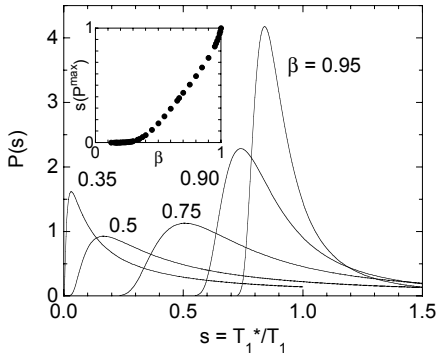

Figure 3.4 Probability density $P(s)$ for several stretched exponential exponents β. The inset shows the s values versus β at which $P(s)$ is maximum.

the inverse Laplace transform of the stretched exponential. The evolution of $P(s)$ with β for several values of β is shown in Fig. 4. With decreasing β, $P(s)$ broadens and becomes highly asymmetric, and the peak in $P(s)$ becomes finite and moves towards slower rates which is compensated by a long tail to faster rates. The value of s at which $P(s)$ is maximum is plotted versus β in the inset of Fig. 4; this value decreases with decreasing β and approaches zero exponentially for $\beta \lesssim 0.5$. The physical significance of $1/T_1^*$ for $1/3 \lesssim \beta < 1$ is that $1/T_1$ is about equally likely to be less than $1/T_1^*$ as it is to be greater; it is neither the average of $1/T_1$ nor the inverse of the average of T_1. For $s \gg 1$, $P(s,\beta) \sim 1/s^{1+\beta}$, so the average $s_{\rm ave} = (T_1^*/T_1)_{\rm ave}$ is infinite. Thus the moments of the distribution depend on the cut-off at large relaxation rates, but this cutoff is irrelevant for the physical interpretation of the long time relaxation. We see that the measured small values for β at low T in Fig. 3 for sample #3-3-a2 and that of Kaps et al. constitute strong evidence for a broad distribution of ^{7}Li $1/T_1$ values at these T.

We now discuss possible physical origins of the $1/T_1$ probability distributions in Fig. 4 and then propose a model that may be applicable to LiV_2O_4 containing magnetic defects. We note at the outset that our NMR measurements were carried out at $H = 10.6$ kOe for which the magnetization of the magnetic defects at $\lesssim 1$ K is significant [14], a situation for which very few calculations of either the average bulk or local electronic spin fluctuations are available. With this caveat, the contribution to the $1/T_1$ of a nucleus located at site $\mathbf{r}$, by fluctuations of

electron spins $\mathbf{S}(\mathbf{r}',t)$ with correlation function $q_{\mathbf{r}',\mathbf{r}''}(t) = \langle S_\alpha(\mathbf{r}',0)S_\alpha(\mathbf{r}'',t)\rangle$, is

$$\frac{1}{T_1}(\mathbf{r}) \propto \int d^3r' d^3r'' A_{\mathbf{r},\mathbf{r}'} A_{\mathbf{r},\mathbf{r}''} q_{\mathbf{r}',\mathbf{r}''}(\omega_n). \tag{3.3}$$

Here $A_{\mathbf{r},\mathbf{r}'}$ is the hyperfine interaction between nuclear and electron spins at sites $\mathbf{r}$ and $\mathbf{r}'$, respectively, and $q_{\mathbf{r}',\mathbf{r}''}(\omega_n)$ is the Fourier transform of the correlation function $q_{\mathbf{r}',\mathbf{r}''}(t)$ at the nuclear Larmor frequency $\omega_n = \gamma_n H$. For example, if one had a unique $1/T_1$, a unique $A_{\mathbf{r},\mathbf{r}'}$ with $\mathbf{r}' = \mathbf{r}''$, and a correlation function $q_{\mathbf{r}',\mathbf{r}'}(t) \sim e^{-\varepsilon t}$, one would have $1/T_1 \propto \varepsilon/(\varepsilon^2 + \omega_n^2)$, yielding a peak in $1/T_1$ as ε decreases through ω_n with decreasing T as observed for $1/T_1^*$ at ≈ 0.7 K in Fig. 3. This simplified example suggests that a significant fraction of the magnetic defects drastically slows down below ~ 1 K.

A distribution of $1/T_1$ could result from a spatial variation in the electron spin dynamics, i.e. $q_{\mathbf{r}',\mathbf{r}''}(t)$, or variations of the hyperfine interactions. In the latter case, a nonlocal hyperfine interaction $A_{\mathbf{r},\mathbf{r}'} \propto |\mathbf{r} - \mathbf{r}'|^{-3}$, caused by dipolar and/or RKKY interactions, can lead to a broad distribution in $1/T_1$. Depending on whether a given nuclear spin is close to or far away from a local defect that dominates the spin response $q_{\mathbf{r},\mathbf{r}'}(t)$, very different $1/T_1$ values occur. Geometric considerations lead to $P(s,\beta) \propto s^{-3/2}$, i.e. a fixed value $\beta = \frac{1}{2}$ for the stretched exponential which is in direct conflict with our data that show a strongly T-dependent β. A physically more interesting case is when stretched exponential nuclear relaxation is due to dynamical heterogeneity of the magnetic defect spin system, i.e. due to spatially varying $q_{\mathbf{r}',\mathbf{r}''}(t)$. For simplicity we consider the limit of a purely local hyperfine interaction $A_{\mathbf{r},\mathbf{r}'} \propto \delta_{\mathbf{r}-\mathbf{r}'}$. In the limit of strongly disordered spin systems, dynamical heterogeneity with anomalous long time dynamics was found in numerical simulations above the spin glass temperature [15]. The averaged autocorrelation function was shown to have the Ogielski form $q(t) = t^{-x}\exp[-(\varepsilon^* t)^\beta]$, where the energy scale ε^* characterizes the averaged electron spin response. As ε^* becomes smaller than ω_n with decreasing T, $1/T_1^*$ goes through a maximum, located at $T \sim 1$ K in our case, and $q(t)$ immediately yields a stretched exponential relaxation for the nuclear spins. However, these results were obtained in the strong disorder limit in contrast to dilute magnetic defects in LiV_2O_4.

The sensitivity of the HF state with respect to perturbations may be critical to under-

stand the behavior of LiV_2O_4 where $n_{\rm defect}$ is rather small, suggesting the following alternative model for the dynamics. If geometric frustration suppresses long range order in pure LiV_2O_4, it becomes natural that crystal defects can locally lift the frustration and cause a condensation of dynamic magnetic order in a finite region of volume $\simeq \xi^3$ around the defect. Due to the proximity to an ordered state and long-range electronic spin coupling in metallic systems, we expect ξ to be much larger than an interatomic spacing, in contrast to insulating frustrated systems with only nearest-neighbor interactions [16]. This might help to explain our previous low-T magnetization measurements which indicated that the magnetic defects have large average spins $\sim 3/2$ to 4 [14]. Fluctuations in the local tendency towards order lead to a probability $p(\xi) \propto e^{-c\xi^3}$ for such a droplet [17] and we analyze the system using the ideas of Griffiths physics in disordered magnets [18].

The lowest excitation energies, ε, of a droplet depend on its size ξ. Depending on how $\varepsilon(\xi)$ varies with ξ, different long-time dynamics emerges [19]. If $\varepsilon \propto \xi^{-\psi}$ the distribution function of the droplet energies becomes $p(\varepsilon) \propto e^{-\left(\frac{\varepsilon^*}{\varepsilon}\right)^{3/\psi}}$. If $1/T_1 \propto \varepsilon$, this yields $P(s,\beta) \propto e^{-s^{-3/\psi}}$, leading for large times to a stretched exponential relaxation with $\beta = \frac{1}{1+\psi/3}$. Such a behavior occurs in magnets with Heisenberg symmetry [19] where one finds $\beta = \frac{1}{2}$, if the spin dynamics is classical. For lower T, where quantum dynamics of the spins sets in, one finds $\beta = \frac{2-z}{4-z} < \frac{1}{2}$, if the dynamical exponent relating length and time scales obeys $z < 2$. For insulating antiferromagnets, one usually has $z = 1$, giving $\beta = 1/3$.

Probably more appropriate to LiV_2O_4 is the case of itinerant antiferromagnets where one expects $z = 2$, and an even more exotic situation occurs. In this case, $\varepsilon \propto e^{-b\xi^3}$, i.e. large droplets become extremely slow leading to quantum Griffiths behavior $P(s) \propto s^{-\lambda}$ at long times with nonuniversal exponent $\lambda = 1 - c/b$. Now, the nuclear spin relaxes according to a power law $1 - M(t)/M(\infty) \propto t^{-(1-\lambda)}$. It becomes very hard to distinguish at large times power law from stretched exponential behavior with small β at low T. However, there are clear predictions of this scenario which include (given $\lambda > 0$) singular non-Fermi-liquid type specific heat $C/T \propto T^{-\lambda}$, susceptibility $\chi \propto T^{-\lambda}$ and similar results for the field dependence of the magnetization [19], which can all be tested in future experiments.

Acknowledgements

Discussions with T. Vojta are gratefully acknowledged. Ames Laboratory is operated for the U.S. Department of Energy by Iowa State University under Contract No. W-7405-Eng-82. This work was supported by the Director for Energy Research, Office of Basic Energy Sciences.

References

[1] D. C. Johnston, S.-H. Baek, X. Zong, F. Borsa, J. Schmalian, and S. Kondo, Phys. Rev. Lett. **95**, 176408 (2005).

[2] A. C. Hewson, *The Kondo Problem to Heavy Fermions* (Cambridge University Press, Cambridge, 1993).

[3] R. Ballou, E. Lelièvre-Berna, and B. Fak, Phys. Rev. Lett. **76**, 2125 (1996), and cited references.

[4] S. Kondo et al., Phys. Rev. Lett. **78**, 3729 (1997).

[5] D. C. Johnston, Physica B **281&282**, 21 (2000).

[6] R. Jin et al., cond-mat/0112405; S. Nakatsuji et al., Phys. Rev. Lett. **90**, 137202 (2003).

[7] P. Fulde, J. Phys.: Condens. Matter **16**, S591 (2004).

[8] A. V. Mahajan et al., Phys. Rev. B **57**, 8890 (1998).

[9] K. Fujiwara et al., J. Phys.: Condens. Matter **16**, S615 (2004).

[10] W. Trinkl et al., Phys. Rev. B **62**, 1793 (2000).

[11] H. Kaps et al., J. Phys.: Condens. Matter **13**, 8497 (2001).

[12] A. J. Millis, Solid State Commun. **126**, 3 (2003).

[13] J. C. Phillips, Rep. Prog. Phys. **59**, 1133 (1996).

[14] S. Kondo, D. C. Johnston, and L. L. Miller, Phys. Rev. B **59,** 2609 (1999).

[15] S. C. Glotzer et al., Phys. Rev. E **57**, 7350 (1998).

[16] J. Villain, Z. Phys. B **33**, 31 (1979).

[17] A. J. Millis, D. K. Morr, and J. Schmalian, Phys. Rev. B **66**, 174433 (2002).

[18] R. B. Griffiths, Phys. Rev. Lett. **23**, 17 (1969).

[19] T. Vojta and J. Schmalian, Phys. Rev. B, **72**, 045438 (2005).

CHAPTER 4. ^{7}Li NMR Study of Magnetic Defects in Heavy Fermion LiV_2O_4

(This chapter is based on part of an article to be submitted to Phys. Rev. B by X. Zong, S. Das, F. Borsa, M. D. Vannette, R. Prozorov, J. Schmalian, and D. C. Johnston)

Abstract

We present a systematic study of the variations of the ^{7}Li NMR properties versus magnetic defect concentrations $n_{\rm defect}$ in powders ($n_{\rm defect} = 0.21, 0.49$, and 0.83 mol%) and single crystals ($n_{\rm defect} = 0.38$ mol%) samples in the temperature T range from 0.5 to 4.2 K. The magnetic defect concentrations are determined through static magnetization measurements in the T range of 1.8–5.0 K. We also studied the ac magnetic susceptibility $\chi_{\rm ac}$ at 14 MHz from 0.5 to 6 K in the single crystals and in the powder sample with 0.83 mol% magnetic defects. Both the ^{7}Li NMR spectrum and nuclear spin-lattice relaxation rate are inhomogeneous in the presence of magnetic defects. We study a model which assumes local field inhomogeneity due to different positions of the ^{7}Li nuclei relative to the magnetic defects. Our study shows that local field inhomogeneity is an important effect of the magnetic defects. Furthermore, our results indicate that the natures of the magnetic defects in the powder and single crystal samples are different. Field-dependent $\chi_{\rm ac}$ measurements show the signature of spin freezing in the powder sample ($n_{\rm defect} = 0.83$ mol%) at $T \approx 1.0$ K, which coincides with the peak position in the nuclear spin-lattice relaxation rate in the same sample. In contrast, spin freezing was not observed in the single crystals down to $T = 0.5$ K from either NMR or $\chi_{\rm ac}$ measurements, despite the relatively large magnetic defect concentration.

4.1 Introduction

LiV_2O_4 is a rare d-electron heavy fermion system at low temperatures $T < 10$ K.[1] The low temperature linear electronic specific heat coefficient γ (0.42 J/mol K^2) and magnetic susceptibility χ_0 (≈ 0.01 cm^3/mol) are 180 and 310 times those of a free electron gas, respectively, assuming each vanadium atom contributes 1.5 free electrons. The Wilson ratio $R_{\rm W}$, the ratio of the enhancement factors of χ_0 and γ, is equal to 1.7, reasonable for a heavy fermion system.[2] Heavy fermion behavior was further confirmed by electrical resistivity measurements which show a T^2 dependence below 2 K with a large coefficient $A = 2.2$ $\mu\Omega$ cm/K^2.[3, 4] The A and γ values approximately follow the Kadowaki-Woods relation, $A/\gamma^2 = 1.0 \times 10^{-5}$ Ω cm(mol K/J)^2, which holds for a variety of heavy fermion systems.[5] Despite continuous theoretical work, a detailed explanation of the heavy fermion behaviors in LiV_2O_4 remains a challenge.[6–8]

NMR was an important local probe in establishing the low temperature heavy fermion behavior in LiV_2O_4.[1, 9] The low temperature ^{7}Li nuclear spin lattice relaxation rate follows a Korringa relation $1/T_1 \propto T$, with a coefficient $1/T_1T = 2.2$ s^{-1}K^{-1}, 6000 times larger than in the non-heavy fermion isostructural superconducting[10] compound $LiTi_2O_4$.[11] The Korringa ratio $\kappa = 4\pi k_{\rm B}\gamma_{\rm n}^2 K^2 T_1 T/\hbar\gamma_{\rm e}^2$, where K is the Knight shift, $\gamma_{\rm n}$ and $\gamma_{\rm e}$ are the gyromagnetic ratios of the ^{7}Li nuclear spin and the conduction electron spin, respectively, is equal to 0.7, which is close to the value of unity expected for a free electron gas.

Recently, we found that the low temperature NMR properties of polycrystalline LiV_2O_4 are sensitive to the presence of a small concentration of magnetic defects ($n_{\rm defect} = 0.73$ mol%) within the spinel structure.[12, 13] While in a sample with negligible magnetic defects, the ^{7}Li nuclear magnetization $M(t)$ after delay t following a sequence of saturation pulses showed a single exponential decay, in the sample with $n_{\rm defect} = 0.73$ mol%, the nuclear spin-lattice relaxation showed a stretched exponential recovery $1 - M(t)/M(\infty) = \exp[-(t/T_1^*)^\beta]$, with the characteristic relaxation rate $1/T_1^*$ showing a peak at temperature $T \approx 0.7$ K. There was also a clear difference in the ^{7}Li NMR spectrum in these two samples. At low temperatures $T < 4.2$ K, the magnetically pure sample had a narrow spectrum with an almost temperature

independent width (full width half maximum FWHM $\sim$ 20 kHz). A strong temperature dependent inhomogeneous broadening (FWHM $\sim$ 100 kHz at $T < 4.2$ K) was observed in the sample with $n_{\rm defect} = 0.73$ mol%.

In order to further clarify the nature of the magnetic defects and their effect on the heavy fermion properties of LiV_2O_4, we performed ^{7}Li NMR studies on LiV_2O_4 samples versus magnetic defect concentration. Three polycrystalline samples and a collection of single crystals are studied in this paper. The powder samples are labeled as 6b, 7a, and 6a, with $n_{\rm defect} = 0.21$ mol%, 0.49 mol%, and 0.83 mol%, respectively. The single crystal sample is labeled as sample 1 with $n_{\rm defect} = 0.38$ mol%. We determined the magnetic defect concentrations through static magnetization measurements in the temperature range of 1.8–5 K and field range 0–5.5 T.[14] Furthermore, to study the presence of spin freezing, we measured the ac magnetic susceptibility at 14 MHz using the tunnel-diode resonator technique[15] of the single crystals and the powder sample 6a with $n_{\rm defect} = 0.83$ mol%.

The temperature dependences of the nuclear spin-lattice relaxation rates in our polycrystalline samples are similar to that of sample 3-3-a2 ($n_{\rm defect} = 0.73$ mol%) that we studied in Ref. [12], which showed a peak in $1/T_1^*(T)$ at about 1 K. However, we find a qualitative difference in the temperature dependence of $1/T_1^*$ in the single crystals, which instead decreases monotonically with decreasing temperature down to 0.5 K. We study the following model to analyze the NMR data. In the model, we consider the effect of a distribution of local fields due to different positions of the ^{7}Li nuclei relative to their nearby magnetic defects. For the polycrystalline samples, the model is quantitatively consistent with the inhomogeneous broadening of the line and the nonexponential relaxation behavior. In the single crystals, the model fails to explain the relaxation behavior at $T \lesssim 1.3$ K.

The remainder of this chapter is organized as follows. Experimental details are given in Sec. 4.2. In Sec. 4.3, we report the experimental results of the magnetization, the ac susceptibility, ^{7}Li NMR spectra, and nuclear spin-lattice relaxation rates. In Sec. 4.4, we analyze the NMR results using the above model. In Sec. 4.5, we summarize the main conclusions of the paper.

4.2 Experimental

Polycrystalline LiV_2O_4 samples were prepared using conventional solid state reaction. The starting materials were V_2O_3 (4N, MV Labs), V_2O_5 (4N, MV Labs), and Li_2CO_3 (5N, Alfa Aeser). Details of the sample synthesis procedure can be found in Ref. [14]. The typical size of the polycrystalline grains is in the range of 1–10 μm,[16] as determined using a scanning electron microscope (SEM). Single crystals were grown using a self-flux technique.[17] The flux consisted of a mixture of Li_3VO_4 and LiV_2O_4. The typical size of the crystals is 0.2 mm. Magnetization measurements were performed using a Quantum Design SQUID magnetometer in the temperature range 1.8–350 K and applied magnetic field range 0–5.5 T.

The ac magnetic susceptibility was measured using a highly sensitive self-resonating LC circuit where losses are compensated by a tunnel diode that has a region of negative differential resistance in its I-V characteristic. The resonant frequency of an empty coil $f_0 = 1/(2\pi\sqrt{LC})$ changes when a sample is placed in a coil. The shift of the resonant frequency, $\Delta f = f\,(T, H) - f_0$ is directly related to the ac susceptibility, $\chi\,(T, H)$, of the sample via[15]

$$\frac{\Delta f}{f_0} \approx -\frac{1}{2}\frac{V_\mathrm{s}}{V_\mathrm{c}} 4\pi\chi_\mathrm{ac}, \tag{4.1}$$

where χ_ac is the dimensionless volume ac susceptibility, V_s is the sample volume, and V_c is the coil volume. The volume magnetization is the magnetic moment per unit volume of the sample, with Gaussian units G cm^3/cm^3 = G. The volume susceptibility is the volume magnetization divided by field, which is then dimensionless. The optimized and thermally stabilized circuit resonates at 14 MHz with a stability of 0.05 Hz over hours.[15] The resonator was mounted in a ^{3}He cryostat with a temperature range 0.5–150 K. A static external field up to 90 kOe can be applied to study field-dependent properties.

^{7}Li NMR measurements were performed utilizing a phase-coherent pulse spectrometer at applied magnetic fields H = 1.06, 1.68 and 3.0 T and in the temperature range 0.5–4.2 K. Measurements above 1.5 K were performed with a ^{4}He bath cryostat and measurements below 1.5 K with a Janis ^{3}He cryostat. The typical $\pi/2$ pulse length was 3 μs. The ^{7}Li NMR spectra for narrow lines (FWHM $\lesssim$ 100 kHz) were measured by Fourier transform of half the Hahn

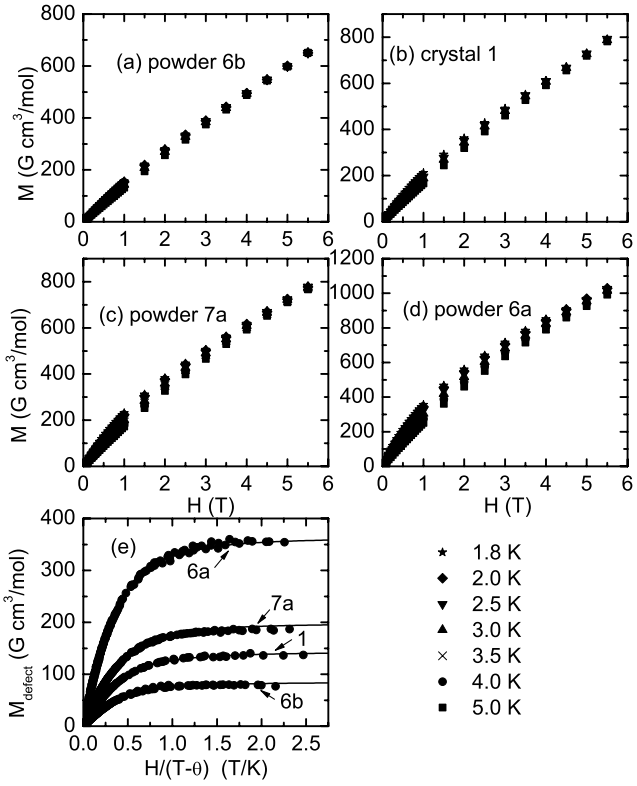

Figure 4.1 (a)–(d) Magnetization M versus applied magnetic field H isotherms at different temperatures T for powder and crystals samples. (e) The magnetic defect contributions $M_{\rm defect} = M - \chi_0 H$ to the data in panels (a)–(d) versus $H/(T-\theta)$. The χ_0 and θ values are listed in Table 4.1. The solid lines are plots of the second term in Eq. (4.2), $M_{\rm defect}$, versus $H/(T-\theta)$ with values of $n_{\rm defect}$, θ, and S given in Table 4.1.

echo signals, while for wider lines, the spectra were measured by integrating the echo area as a function of the applied magnetic field at a fixed frequency of rf pulses. Nuclear spin-lattice relaxation rates were measured by monitoring the recovery of the spin echo height using the standard saturation-recovery pulse sequence.

4.3 Results

4.3.1 Magnetic Defect Concentrations

The magnetic defect concentrations of the samples were determined from the low temperature (1.8 K $< T <$ 5 K) magnetization M versus applied magnetic field H isotherms.[14]

Table 4.1 Best fit values of the magnetic defect concentration $n_{\rm defect}$, the spin value S, the intrinsic susceptibility χ_0, and the effective Weiss temperature θ for powder samples 6b, 7a, and 6a and crystal sample 1 obtained by fitting Eq. (4.2) to the low temperature (1.8 K $\leq T \leq$5 K) magnetization versus field isotherms.

Sample	$n_{\rm defect}$ (mol%)	S	χ_0 (cm^3/mol)	θ (K)
6b	0.21(1)	3.6(2)	0.0104(1)	-0.75(14)
7a	0.49(1)	3.5(1)	0.0108(1)	-0.57(6)
6a	0.83(3)	3.9(1)	0.0122(2)	-0.64(10)
1	0.38(1)	3.3(1)	0.01186(4)	-0.43(6)

Figures 4.1(a), (b), (c), and (d) show the M versus H isotherms at different temperatures for samples 6b, 1, 7a, and 6a, respectively. The magnetic defect concentration $n_{\rm defect}$ and spin value S of the magnetic defects in each sample are determined by fitting the equation

$$M = \chi_0 H + N_{\rm A} g \mu_{\rm B} n_{\rm defect} S B_S(x) \tag{4.2}$$

to the M versus H isotherms at $T < 5$ K.[14] In Eq. (4.2), χ_0 is the intrinsic molar susceptibility of LiV_2O_4 at low temperatures $T < 5$ K, $N_{\rm A}$ is Avogadro's number, g is the (powder-averaged) spectroscopic splitting factor (g-factor) for the defect spins, $B_S(x)$ is the Brillouin function for spin S, and $x = gH\mu_{\rm B}S/k_{\rm B}(T-\theta)$. χ_0, S, θ, and $n_{\rm defect}$ are free parameters in the fit. The g value is fixed to 2 during the fit.[14] The best fit results are listed in Table 4.1. Figure 4.1(e) shows the defect contributions $M_{\rm defect} = M - \chi_0 H$ versus $H/(T-\theta)$ for the four samples. All the data points in Figs. 4.1(a), (b), (c), and (d) fall onto a universal curve for each sample, respectively, as described by the second term in Eq. (4.2).

4.3.2 ac Magnetic Susceptibility at 14 MHz

The ac magnetic susceptibility, $\chi_{\rm ac} = dM/dH$, is an important parameter directly related to the electronic spin dynamics. It is very sensitive to collective behavior such as spin freezing and a transition to the glassy state. Figure 4.2 shows $\Delta\chi_{\rm ac} \equiv \chi_{\rm ac}(T) - \chi_{\rm ac}(4.8\ {\rm K})$ versus temperature T at various values of the external field for powder sample 6a with $n_{\rm defect} =$ 0.83 mol%. Each curve corresponds to a magnetic field listed in the legend and the curves from top to bottom correspond to increasing magnetic field. We note that the change of

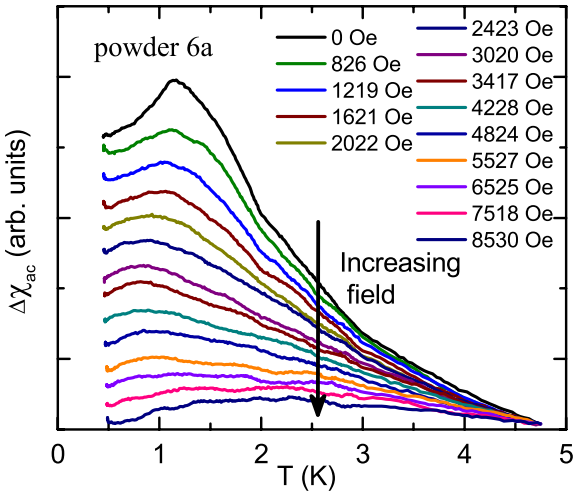

Figure 4.2 (color online.) $\Delta\chi_{\rm ac}$, the change of ac susceptibility $\chi_{\rm ac}$ at 14 MHz relative to its value at 4.8 K, versus temperature T for powder sample 6a with $n_{\rm defect} = 0.83$ mol% at several values of the magnetic field (indicated in the legend). $\chi_{\rm ac}$ decreases with increasing magnetic field.

the magnetic moment amplitude of the measured sample on decreasing the temperature from 1.1 K to 0.5 K in zero field corresponds to a change in magnetic moment of only about 5×10^{-10} G cm^3, which cannot be resolved by a conventional SQUID magnetometer for the same size (~ 0.3 mm^3) sample.

At zero static applied field, there is an obvious peak in $\Delta\chi_{\rm ac}$ at about 1.1 K in Fig. 4.2 that is most likely indicative of a collective freezing of the magnetic moments. The field dependence of the magnetic susceptibility is characteristic of a spin glass system where spin randomness is suppressed by the uniaxial field and the peak in $\chi_{\rm ac}$ associated with spin freezing is suppressed because the magnetic moments are closer to saturation. This result suggests collective freezing behavior of the magnetic defects in the LiV_2O_4 powder sample in zero field.

For our sample 1 consisting of a collection of single crystals with overall $n_{\rm defect} = 0.38$ mol%, the situation is quite different. We cannot measure the spin susceptibility because the diamagnetic susceptibility $\chi_{\rm ac,skin}$ arising from skin depth effects dominates it. The skin depth δ can be calculated from [18]

$$\delta = \frac{504}{(\sigma K_m \nu)^{1/2}} \text{ meters}, \tag{4.3}$$

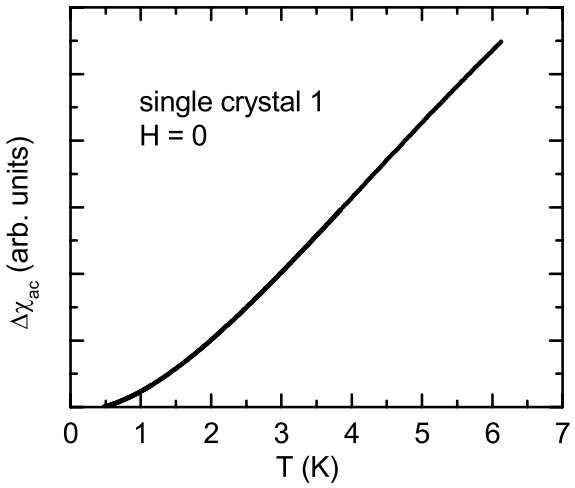

Figure 4.3 $\Delta\chi_{\rm ac}$, the change of ac magnetic susceptibility $\chi_{\rm ac}$ relative to its value at 0.5 K, versus temperature T in single crystal LiV_2O_4 (sample 1) in zero applied field and at a frequency of 14 MHz.

where K_m is relative permeability, σ is the conductivity in $\Omega^{-1}\mathrm{m}^{-1}$, and ν is the applied frequency in Hz. Setting $K_m = 1$, $\sigma = 5 \times 10^6\ \Omega^{-1}\mathrm{m}^{-1}$($\sigma$ value at 1.8 K in Ref. [17]), and $\nu = 14$ MHz, we obtain $\sigma \approx 0.06$ mm, significantly smaller than the size of each crystal in sample 1. Thus we expect that the $\chi_{\rm ac,\,skin}$ contribution to $\chi_{\rm ac}$ is significant and its effect increases with decreasing temperature as the resistivity decreases monotonically with decreasing temperature.[3, 4] Figure 4.3 shows the $\Delta\chi_{\rm ac} \equiv \chi_{\rm ac}(T) - \chi_{\rm ac}(0.5\ \mathrm{K})$ versus temperature T from 0.5 to 6 K. Since the static susceptibility of various samples is nearly T-independent or increases with decreasing T over this T range, the decrease in $\Delta\chi_{\rm ac}$ with decreasing T in Fig. 4.3 indicates that $\chi_{\rm ac,\,skin}(T)$ dominates the $\chi_{\rm ac}$ response there. Furthermore, we see no evidence for a collective spin freezing for this sample, and we did not find any field dependence up to an applied field of 10 kOe (not shown).

4.3.3 ^{7}Li NMR Line Width

The ^{7}Li NMR absorption line width is related to the local static magnetic field distribution. It becomes broader with increasing concentrations of magnetic defects. Figure 4.4 shows the absorption lines of the four samples at temperature $T = 4.2$ K and $H = 1.06$ T. Although the ^{7}Li nuclei have spin $I = 3/2$, both first and second order nuclear quadrupole broadening due

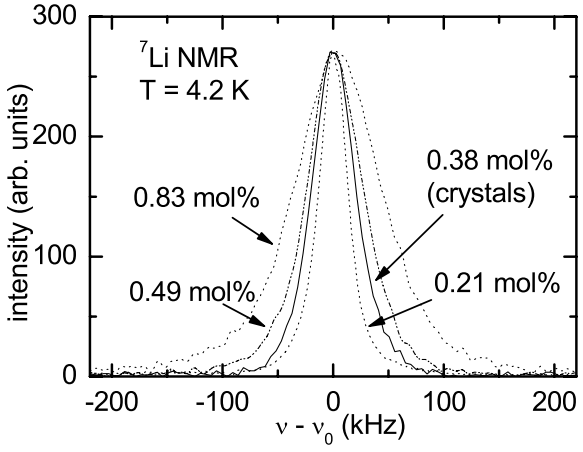

Figure 4.4 The ^{7}Li NMR absorption versus rf frequency ν at temperature $T = 4.2$ K and applied magnetic field $H = 1.06$ T in the four LiV_2O_4 samples. The frequency $\nu_0 = 17.6$ MHz.

to a structural distortion can be ruled out since we observe no satellite peaks or shortening of $\pi/2$ pulse length as compared to the magnetically pure LiV_2O_4 sample.[19, 20] The line width is significantly larger than the intrinsic width for an individual ^{7}Li nuclear spin, indicating an inhomogeneous magnetic broadening of the line. The intrinsic line width is of the order of $1/T_2 \approx 5$ kHz, where T_2 is the nuclear spin-spin relaxation time and is almost independent of the defect concentration and temperature below 4.2 K. Figure 4.5 displays the temperature dependences of the full width at half maximum peak intensity (FWHM) of the spectra for the four samples.

The broadening of the ^{7}Li NMR line has three contributions. The first contribution comes from the nuclear ^{7}Li-^{51}V and ^{7}Li-^{7}Li dipolar interactions. This contribution can be estimated using the Van Vleck second moment $\langle \Delta\omega^2 \rangle$.[21] A second broadening comes from the macroscopic field inhomogeneity due to a distribution of the demagnetization factors and a distribution of magnetic fields due to neighboring powder grains. This contribution is proportional to the magnetization of the sample and the resulting root mean square deviation of ^{7}Li NMR resonance frequencies can be written as $BM\rho_N\gamma_{\rm Li}/2\pi$, where M is the molar susceptibility, ρ_N is the density of LiV_2O_4 formula units in the sample, $\gamma_{\rm Li}$ the gyromagnetic ratio of ^{7}Li nuclei, and B a dimensionless factor. B is estimated to be 1.43 for a close packed powder sample

with ellipsoidal shapes.[22] A third broadening contribution comes from inhomogeneity due to the presence of magnetic defects within the sample. An estimate for this contribution is not possible without a model of the nature of the defects and the types of interactions between the defects and nearby ^{7}Li nuclear spins. However, the presence of this contribution can be inferred by comparing the experimental FWHM values and the values expected when including only the first two contributions, as follows.

The FWHM resulting from the first two contributions can be calculated within a Gaussian approximation by

$$\mathrm{FWHM_a} = 2.35\sqrt{\langle\Delta\omega^2\rangle/(2\pi)^2 + (BM\rho_N\gamma_{\mathrm{Li}}/2\pi)^2} \tag{4.4}$$

with $B = 1.43$, and $\langle\Delta\omega^2\rangle^{1/2}/2\pi = 2.7$ kHz.[23] M is calculated from Eq. (4.2) using the parameter values listed in Table 4.1. The $\mathrm{FWHM_a}$ calculated from Eq. (4.4) is plotted as the dashed lines in Fig. 4.5. It is clear that Eq. (4.4) cannot account for the observed broadening of the lines, so a local magnetic field inhomogeneity due to the presence of the magnetic defects must be present in the samples. We will return to this issue in Sec. 4.4.2.

4.3.4 Nuclear Spin-Lattice Relaxation Rates

The longitudinal ^{7}Li nuclear spin relaxation versus time $M(t)$ exhibits an increasingly non-exponential behavior with increasing amounts of magnetic defects or decreasing temperature. Figure 4.6 shows the recoveries of $M(t)$ following a saturation sequence for the four samples at different temperatures. The recovery data can be described by a stretched exponential function

$$1 - \frac{M(t)}{M(\infty)} = \exp[-(t/T_1^*)^\beta]. \tag{4.5}$$

The solid curves in Fig. 4.6 are best fits to the data by Eq. (4.5). The best fit values of $1/T_1^*(T)$ and $\beta(T)$ are shown in Figs. 4.7 and 4.8 for powder and single crystal samples, respectively.

The temperature dependence of $1/T_1^*$ is quite different in the powder and single crystal samples. A peak is observed in $1/T_1^*(T)$ for the powder samples 6a ($n_{\mathrm{defect}} = 0.83$ mol%, $T_{\mathrm{peak}} \approx 1.0$ K) and 7a ($n_{\mathrm{defect}} = 0.49$ mol%, $T_{\mathrm{peak}} \approx 0.6$–$0.7$ K). In the powder sample 6b with the smallest magnetic defect concentration ($n_{\mathrm{defect}} = 0.21$ mol%), $1/T_1^*$ starts to increase

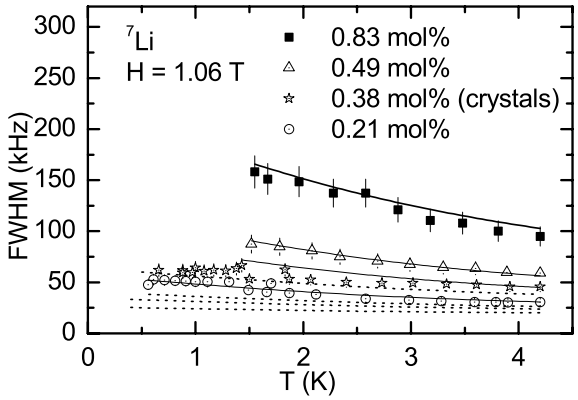

Figure 4.5 Temperature T dependence of full width at half maximum intensity (FWHM) of the ^{7}Li NMR spectrum under external magnetic field $H = 1.06$ T in the four LiV_2O_4 samples. The symbols are experimental results. The dotted lines are plots of Eq. (4.4) (with $B = 1.43$) that takes into account the contributions due to powder broadening and nuclear dipole-dipole interactions, but does not take into account local field inhomogeneity due to the magnetic defects. The solid lines are fits by Eq. (4.7), which also takes into account the local field inhomogeneity. The fitted solid lines from bottom to top are for samples with $n_{\rm defect} = 0.21$, 0.38 (crystals), 0.49, and 0.83 mol%, respectively.

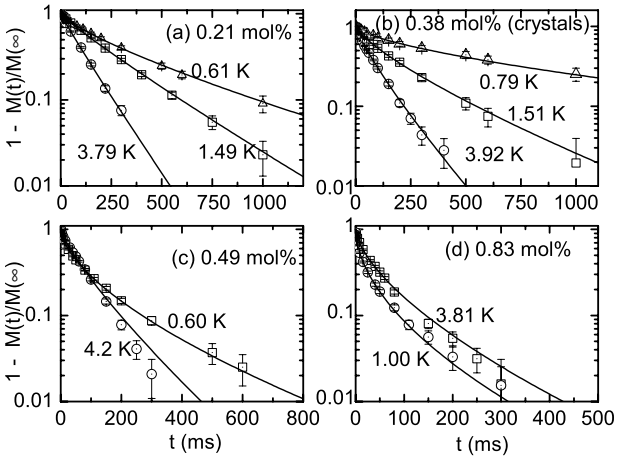

Figure 4.6 Recovery of ^{7}Li nuclear magnetization $M(t)$ after time delay t following a sequence of saturation pulses. Note that the nuclear magnetization $M(t)$ is different from the electronic spin magnetization in Fig. 4.1. The data points were obtained in applied magnetic field $H = 1.06$ T at the indicated temperatures and with rf frequency $\nu = 17.6$ MHz for samples with (a) 0.21 mol%, (b) 0.38 mol% (crystals), (c) 0.49 mol%, and (d) 0.83 mol% magnetic defects. The solid curves are fits to the data by Eq. (4.5).

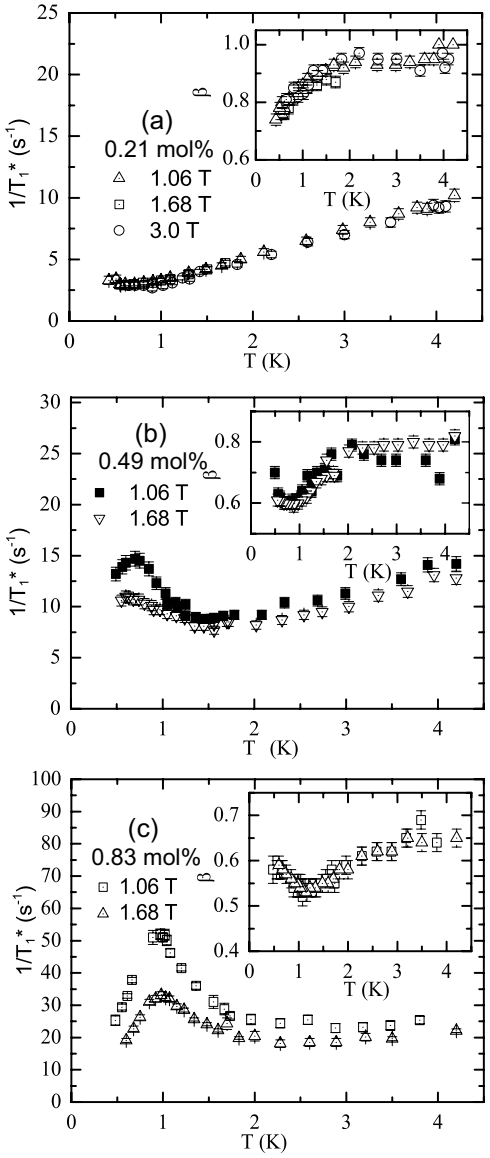

Figure 4.7 $1/T_1^*$ and β vs temperature T obtained by fitting data as in Figs. 4.6(a), (c), and (d) by Eq. (4.5), of (a) powder sample 6b with $n_{\rm defect} = 0.21$ mol% at external magnetic fields $H = 1.06$, 1.68, and 3.0 T, (b) powder sample 7a with $n_{\rm defect} = 0.49$ mol% at $H = 1.06$, 1.68 T, and (c) powder sample 6a with $n_{\rm defect} = 0.83$ mol% at $H = 1.06$ and 1.68 T.

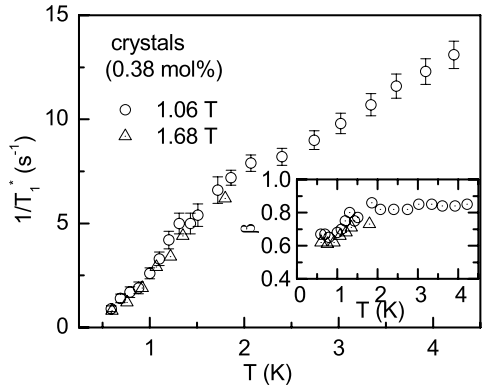

Figure 4.8 $1/T_1^*$ and β versus temperature T of the crystal sample 1 with $n_{\rm defect} = 0.38$ mol% in external magnetic fields $H = 1.06$ and 1.68 T, obtained by fitting data as in Fig. 4.6(b) by Eq. (4.5).

at the lowest experimental temperatures and might exhibit a peak with further decreasing temperature. The peak positions in sample 6a for $H = 1.06$ and 1.68 T are almost the same as the peak position in $\chi_{\rm ac}(T)$ for this sample at $H = 0$ in Fig. 4.2. We conclude that the peaks in $1/T_1^*$ originate from the spin freezing of the magnetic defects. In the crystal sample, $1/T_1^*(T)$ in Fig. 4.8 decreases monotonically with decreasing temperature with a $1/T_1^*$ value at 0.5 K much smaller than in the powder samples, and there is no sign of spin freezing.

Before ending this subsection, we comment about the effect of inhomogeneous broadening on the relaxation measurements. Because of the increasing inhomogeneous broadening with decreasing temperature, some of the ^{7}Li nuclei may be shifted out of the NMR spectrometer response window ($\Delta f \sim 200$ kHz) and excluded from the relaxation measurements. The number of observed ^{7}Li nuclei can be estimated from the product of fully recovered echo height $M(\infty)$ and the temperature, which is proportional to the nuclear Curie constant C in the Curie law for $M(\infty) = C/T$. These data are shown for $H = 1.06$ T versus temperature T in Fig. 4.9. For powder samples 6b ($n_{\rm defect} = 0.21$ mol%) and 7a ($n_{\rm defect} = 0.49$ mol%), the decrease of $M(\infty)T$ is less than 10% when the temperature decreases from 4.2 K to the lowest temperature (≈ 0.5 K). In contrast, for sample 6a ($n_{\rm defect} = 0.83$ mol%), $M(\infty)T$ starts to decrease below $T \approx 3.5$ K and at the lowest temperature ($T \approx 0.5$ K), $M(\infty)T$ is about 50% of that at 4.2 K. As we will show below, the nuclei at the wings of the spectrum have

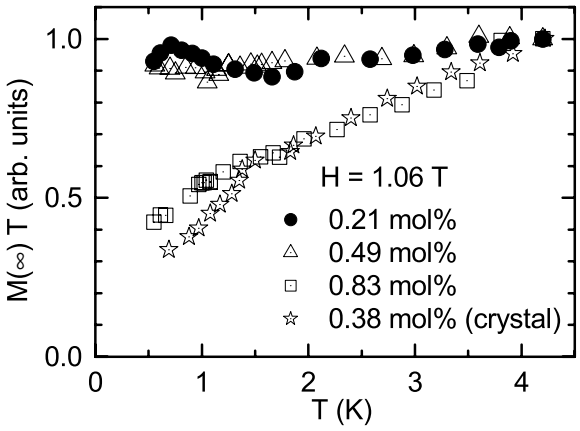

Figure 4.9 The fully recovered echo intensity $M(\infty)$, which is the total equilibrium nuclear magnetization, times temperature T versus T in the nuclear spin-lattice relaxation rate measurements of the four LiV_2O_4 samples in an applied field $H = 1.06$ T.

an average relaxation rate larger than those at the center of the spectrum. Exclusion of those nuclei in sample 6a can thus result in a smaller measured relaxation rate in that sample.

In the crystals, the normalized signal intensity $M(\infty)T$ also decreases with decreasing temperature. Since the line width in the crystals is less than in powder sample 7a (see Fig. 4.5), where no significant signal loss is observed, we attribute the signal loss to the effect of rf field skin depth. Here, only the ^{7}Li nuclear spins within the skin depth contribute to the NMR signal. Setting $K_m = 1$, $\sigma = 5 \times 10^6\ \Omega^{-1}\ \mathrm{m}^{-1}$ (the value of σ at 1.8 K in Ref. [17]), and $\nu = 17.6$ MHz, Eq. (4.3) gives $\delta = 0.054$mm, which is less than the typical size (0.2 mm) of the crystals. However, there is an unexplained kink in the data for the crystals at $T \approx 1.4$ K in both Figs. 4.8 and 4.9.

4.3.5 Relaxation at Different Positions in the Spectra

The observation of a stretched exponential relaxation behavior indicates the presence of a distribution of nuclear spin-lattice relaxation rates $1/T_1$. In order to study the origin of the $1/T_1$ distribution, we performed the following "hole burning" experiment. This experiment extends our previous hole burning experiment briefly described in Ref. [12]. We also studied the relaxation behavior at different positions of the NMR absorption line.

Figures 4.10(a) and (b) display the recovery of a "hole" in the echo spectrum in applied magnetic field $H = 1.06$ T, obtained from Fourier transform of half the Hahn echo signal generated by two strong rf pulses following a weak $\pi/2$ pulse in samples 6a ($n_{\rm defect} = 0.83$ mol%) and 6b ($n_{\rm defect} = 0.21$ mol%), respectively. The weak $\pi/2$ pulse has a width of 56 μs and most of its power is distributed within a narrow frequency window of width ≈ 40 kHz. Such a weak $\pi/2$ pulse only saturates the central part of the spectrum. It is clear that the hole recovery process does not affect the rest of the line and thus spectral diffusion does not occur in our time scale. That is, nuclei with different Larmor frequencies are not coupled to each other over the NMR measurement time scale of $T_1 \sim 100$ ms.

Lack of spectral diffusion as observed above allows us to investigate the nuclear spin-lattice relaxation at different positions of the spectrum. Due to the strong ^{7}Li NMR signal at low temperatures, we were able to study the relaxation of ^{7}Li far out on the wings of the spectrum although the signal intensity is much weaker than at the peak. Figure 4.11 displays the nuclear spin-lattice relaxation curves of powder sample 7a ($n_{\rm defect} = 0.49$ mol%) in $H = 1.68$ T with the rf pulse frequency equal to, 400 kHz higher than, or 400 kHz lower than, the peak frequency of the line. All three recovery curves are nonexponential. It is clear from Fig. 4.11 that the nuclei close to the peak of the line have an average relaxation rate lower than those away from the peak. As will be discussed below, the behavior in Fig. 4.11 is consistent with an inhomogeneous local magnetic field induced by the magnetic defects. It is noted that the temperatures at which the three relaxation curves were taken are slightly different. However, such small temperature differences should be negligible compared to the large difference of relaxation rates between these three curves.

4.4 Analysis

4.4.1 Introduction

The microscopic nature of the magnetic defects has to be assumed in order to analyze the NMR results. We will examine the following model concerning the nature of the defects. In our model, the defects are treated as identical localized paramagnetic moments. In this model,

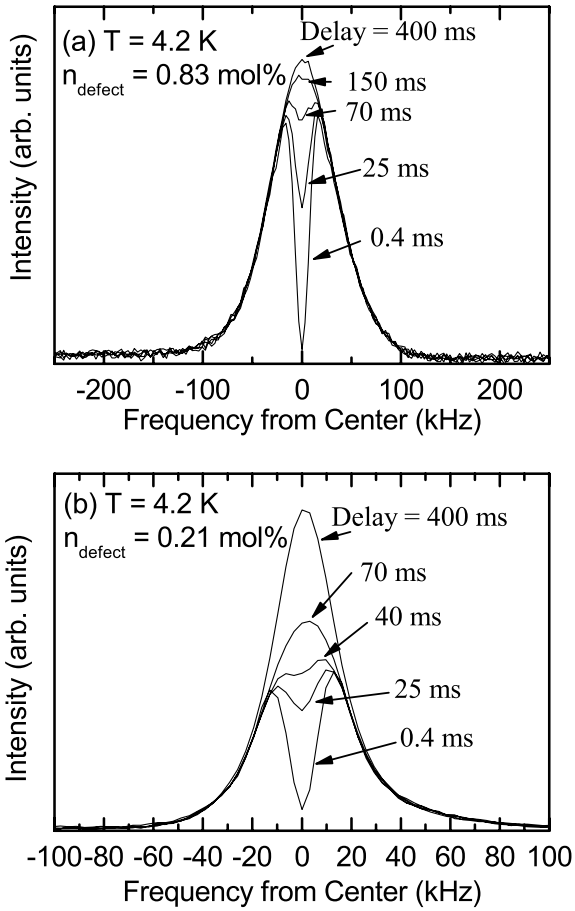

Figure 4.10 Recovery at 4.2 K of a "hole" in the absorption spectrum produced by a weak $\pi/2$ pulse with pulse length of 56 μs at delay = 0 in sample (a) 6a ($n_{\text{defect}} = 0.83$ mol%) and (b) 6b ($n_{\text{defect}} = 0.21$ mol%). The applied magnetic field H is 1.06 T and the center frequency is 17.6 MHz. The delay times after which the spectra were measured by two strong rf pulses are given in the figures. Note the different abscissa scales in (a) and (b).

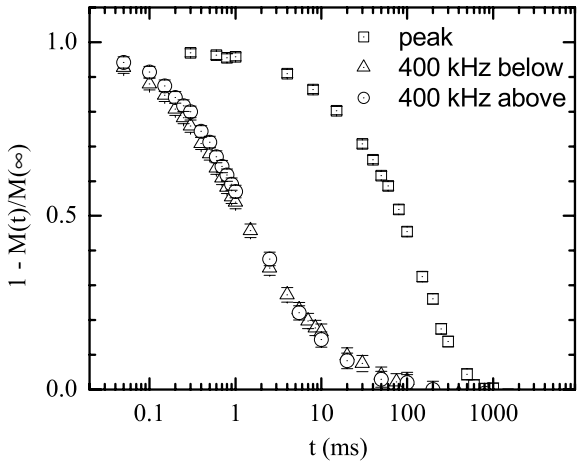

Figure 4.11 Recovery at 4.2 K of ^{7}Li longitudinal nuclear magnetization $M(t)$ following a saturation sequence at $t = 0$ measured at different positions of the spectrum in powder sample 7a ($n_{\text{defect}} = 0.49$ mol%) under external magnetic field $H = 1.68$ T. The recovery curves, which are nonexponential, were measured with rf pulse frequency: (⊡) equal to the peak of the spectrum (27.8 MHz) and at $T = 1.56$ K, (△) 400 kHz lower than the peak and at $T = 1.53$ K, and (○) 400 kHz higher than the peak and at $T = 1.77$ K, respectively.

the distribution of nuclear spin-lattice relaxation rates and the inhomogeneous broadening of the line are entirely due to the local field inhomogeneity, which arises from a distribution of positions of the ^{7}Li nuclei relative to the magnetic defects. Furthermore, we assume that the measured ^{7}Li relaxation rates consist of the sum of two contributions. The first comes from the underlying Fermi liquid via the interaction of nuclei with the conduction electrons and the second comes from the magnetic defects. The first (homogeneous) contribution is described by the $1/T_1 \propto T$ Korringa behavior.[24] The separation of these two contributions is supported by previous transport and magnetization measurements. Transport measurements in LiV_2O_4 crystals without magnetic defects show that the system remains metallic down to temperature $T \approx 0.3$ K.[3, 4] With the addition of small concentrations of magnetic defects, the metallic behavior is assumed to be preserved in most, if not all, parts of the sample volume. An indication for the presence of a heavy Fermi liquid in samples with magnetic defects also comes from magnetization measurements. The magnetization as expressed in Eq. (4.2) contains a contribution $\chi_0 H$ almost independent of the defect concentrations (see

Table 4.1). This contribution is most likely due to the same heavy Fermi liquid present in magnetically pure LiV_2O_4.

4.4.2 Line Width

First we will analyze the line width within the first model. Dilute paramagnetic centers give rise to a broadening of the NMR spectrum through inhomogeneous dipolar and RKKY interactions and in the limit of great dilution the line shape approaches a Lorentzian with full width at half maximum ($\mathrm{FWHM_b}$) intensity given by [25]

$$\begin{aligned} \mathrm{FWHM_b} &= A\frac{8\pi\rho_N n_{\mathrm{defect}}}{9\sqrt{3}} g\mu_{\mathrm{B}}\gamma_{\mathrm{Li}}\langle S_z\rangle \\ &= 4.5An_{\mathrm{defect}}SB_S(x)\ \mathrm{MHz}, \end{aligned} \tag{4.6}$$

where $\rho_N = 1.44\times10^{22}\ \mathrm{cm}^{-3}$ is the density of LiV_2O_4 formula units, $A = 1$ for purely dipolar interactions and $A > 1$ if the RKKY interaction is also important, $\langle S_z\rangle$ is the thermal average value of magnetic defect spin polarization along the direction of the applied magnetic field and is equal to $SB_S(x)$ with $x = gH\mu_{\mathrm{B}}S/k_{\mathrm{B}}(T-\theta)$ [see Eq. (4.2)]. The line shape due to the dilute magnetic defects is Lorentzian[25] while the line shape due to the first two contributions in Eq. (4.4) is Gaussian.[21, 22] In order to obtain the final FWHM value, we convolute a Gaussian distribution with FWHM = 1 with a Lorentzian distribution that has FWMH = x and the same mean value as the Gaussian distribution. We find that the FWHM of the convoluted distribution can be approximated by $(1+x^{8/5})^{5/8}$ to within 10% for all values of x. We estimate the total FWHM by combining Eqs. (4.4) and (4.6) according to

$$\begin{aligned} \mathrm{FWHM} &= (\mathrm{FWHM_a}^{\frac{8}{5}} + \mathrm{FWHM_b}^{\frac{8}{5}})^{\frac{5}{8}} \\ &= \left\{\mathrm{FWHM_a}^{\frac{8}{5}} + [4.5An_{\mathrm{defect}}SB_S(x)\ \mathrm{MHz}]^{\frac{8}{5}}\right\}^{\frac{5}{8}}. \end{aligned} \tag{4.7}$$

By using values of n_{defect}, S, θ, and χ_0 from Table 4.1 and the results for $\mathrm{FWHM_a}$ in Fig. 4.5, Eq. (4.7) was used to simultaneously fit the measured FWHM data for all four samples with a common A as the only fitting parameter. All data points in Fig. 4.5 are used in the fit

except for the single crystal data below 1.5 K, where the nuclear spin-lattice relaxation rates in Fig. 4.8 indicates a possible screening of the magnetic defects. The best fit value of A is $A = 1.4$. The best fits are displayed as the solid curves in Fig. 4.5. The good fits show that the inhomogeneous broadening of the spectrum can be explained within the first model.

4.4.3 Nuclear Spin-Lattice Relaxation

In our model, the distribution of ^{7}Li $1/T_1$ arises from the local field inhomogeneity due to the dependence of fluctuating local fields on the positions of the nuclei relative to the magnetic defects. Since the relative positions of ^{7}Li nuclei with respect to the defects are fixed, the shape of the $1/T_1$ distribution due to the defects should be temperature independent. This would give rise to a temperature independent β value in the stretched exponential function[26] if there were no additional contributions to the ^{7}Li nuclear spin-lattice relaxation.

The observed temperature dependent stretching exponent β in the insets of Figs. 4.7 and 4.8 is explained in this model by the additional Korringa contribution to $1/T_1$ that is proportional to the temperature. Since the nuclear spin-lattice relaxation rate due to itinerant conduction electrons is assumed to be homogeneous across the sample, the nuclear spin recovery due to the conduction electrons alone should be a single exponential. As discussed above, the recovery due to the defects alone is a stretched exponential function with a temperature-independent β. The observed temperature dependent β arises in our model from different temperature dependences of the Korringa and magnetic defect contributions to the nuclear spin-lattice relaxation. Different temperature dependences result in different weights of these two contributions at different temperatures and accordingly different β values are seen at different temperatures when the total recovery is fitted by a stretched exponential function Eq. (4.5).

Thus to identify the contribution of the magnetic defects to the nuclear spin-lattice relaxation, one has to first remove the Korringa contribution by multiplying the original relaxation curves by an exponential function $\exp(t/T_{1\mathrm{K}})$,[27] yielding the decay curve $p(t)$ associated with

relaxation by magnetic defects,

$$p(t) = \left[1 - \frac{M(t)}{M(\infty)}\right] \exp\left(\frac{t}{T_{1\mathrm{K}}}\right), \tag{4.8}$$

where we assume a concentration independent Korringa contribution $1/T_{1\mathrm{K}} = (2.2\ \mathrm{s}^{-1}\mathrm{K}^{-1})T$ and the coefficient of T is taken to be the value in a magnetically pure sample.[12] Figures 4.12 and 4.13(a) show the logarithm of $p(t)$ vs $t^{1/2}$ in $H = 1.06$ T and at different temperatures for powder and single crystals, respectively. In powder samples 7a ($n_{\mathrm{defect}} = 0.49$ mol%) and 6a ($n_{\mathrm{defect}} = 0.83$ mol%), $p(t)$ can be fitted with a root exponential function [i.e., $\beta = 0.5$ in Eq. (4.5) for the magnetic defect contribution]

$$p(t) = \exp[-(t/T_{1\mathrm{d}}^{*})^{1/2}] \tag{4.9}$$

at all temperatures, as shown by the linear fits in Figs. 4.12(b) and (c), respectively. In powder sample 6b with a small $n_{\mathrm{defect}} = 0.21$ mol% in Fig. 4.12(a), $p(t)$ follows root exponential behavior only at short times. The deviation at longer times might be due to the effect of spin diffusion, which will be discussed later. In the crystals, $p(t)$ in Fig. 4.13(a) follows root exponential decay only above 1.3 K and at lower temperature $p(t)$ instead shows an unphysical increase at later times. This indicates that Eq. (4.8) overestimates the conduction electron contribution to the nuclear spin-lattice relaxation at temperatures below 1.3 K.

We extract $1/T_{1\mathrm{d}}^{*}$ values in Eq. (4.9) by fitting the single exponential $p(t)$ versus $t^{1/2}$ data by Eq. (4.9). The best fit results of $1/T_{1\mathrm{d}}^{*}$ are displayed in Figs. 4.13(b) and 4.14 for the single crystal and powder samples, respectively. The $1/T_{1\mathrm{d}}^{*}$ versus temperature T in powder samples 7a and 6a in Figs. 4.14(b) and (c) show an almost field independent peak, similar to the peaks in $1/T_1^{*}$ versus T in Figs. 4.7(b) and (c). As discussed above, the peaks are related to the spin freezing of the magnetic defects. For the single crystals, we only extract $1/T_{1\mathrm{d}}^{*}$ values above 1.3 K and a decrease of $1/T_{1\mathrm{d}}^{*}$ is observed in Fig. 4.13(b) below 2 K.

The above root exponential relaxation behavior has been reported previously in systems where the nuclear spin-lattice relaxation rate is proportional to $1/r^6$, where r is the distance between a nucleus and a nearby paramagnetic center, and no nuclear spin diffusion takes place.[27, 28] Nuclear spin-lattice relaxation due to fluctuations of both dipolar and RKKY

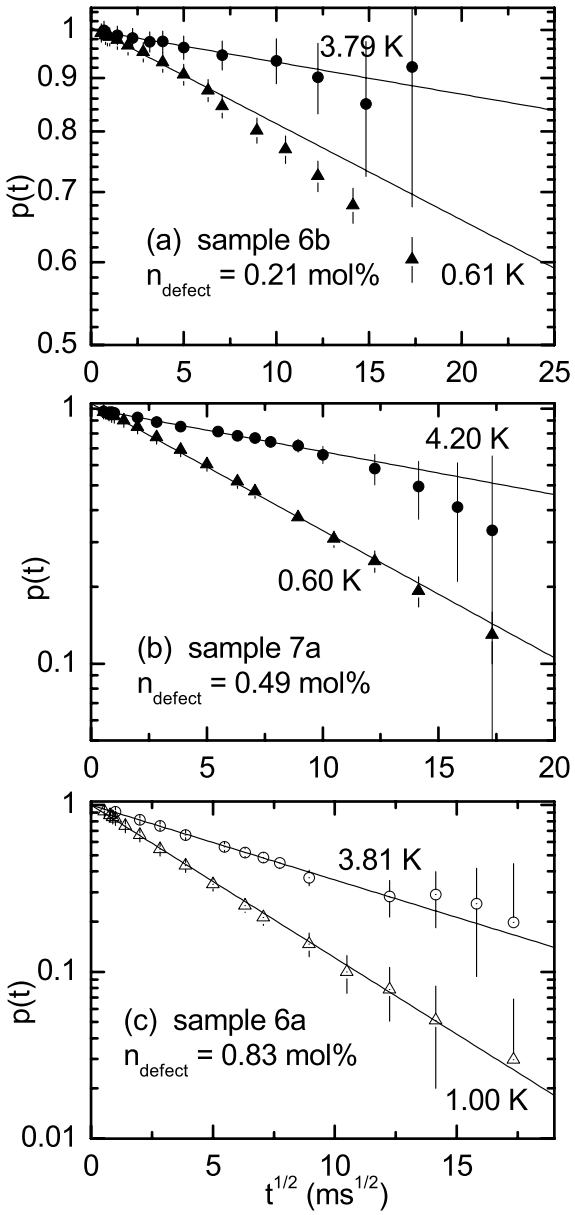

Figure 4.12 Semilog plot of $p(t)$ in Eq. (4.8) versus the square root of the delay time $t^{1/2}$ for the powder samples (a) 6b with $n_{\rm defect} = 0.21$ mol%, (b) 7a with $n_{\rm defect} = 0.49$ mol%, and (c) 6a with $n_{\rm defect} = 0.83$ mol% at applied magnetic field $H = 1.06$ T and different temperatures. The straight lines are best fits of the data by Eq. (4.9), with parameters $1/T_{\rm 1d}^{*}$ given in Fig. 4.14.

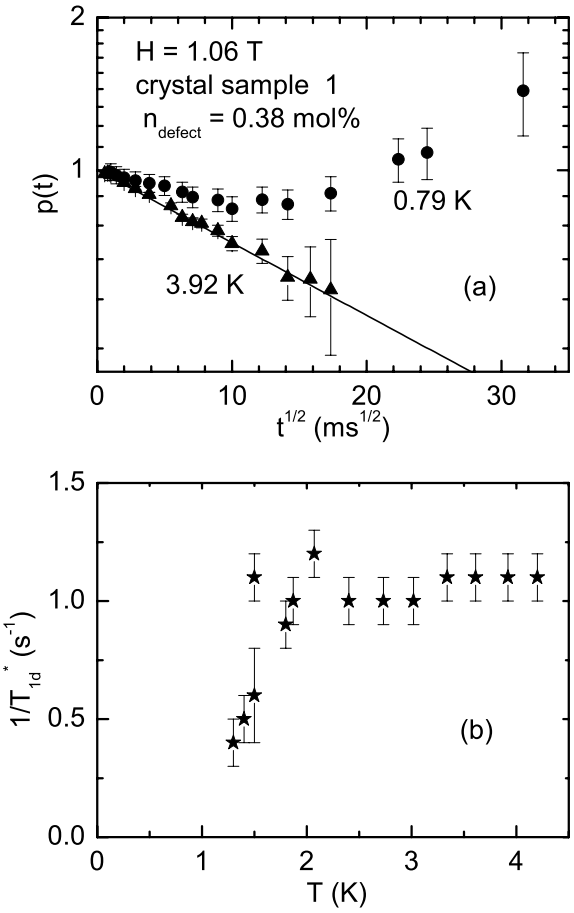

Figure 4.13 (a) Semilog plot of the relaxation function $p(t)$ in Eq. (4.8) versus the square root of the delay time $t^{1/2}$ for the crystal sample 1 with $n_{\rm defect} = 0.38$ mol% at applied magnetic field $H = 1.06$ T and at two different temperatures. The upturn in the 0.79 K data at large times shows that the assumption of a homogeneous Korringa contribution is not valid at $T \lesssim 1.3$ K in the crystals. The straight line is a best fit of the 3.92 K data by Eq. (4.9). (b) $1/T^*_{\rm 1d}$ in Eq. (4.9) versus temperature T in $H = 1.06$ T and above 1.3 K, where the upturn seen for $T = 0.79$ K in (a) is absent.

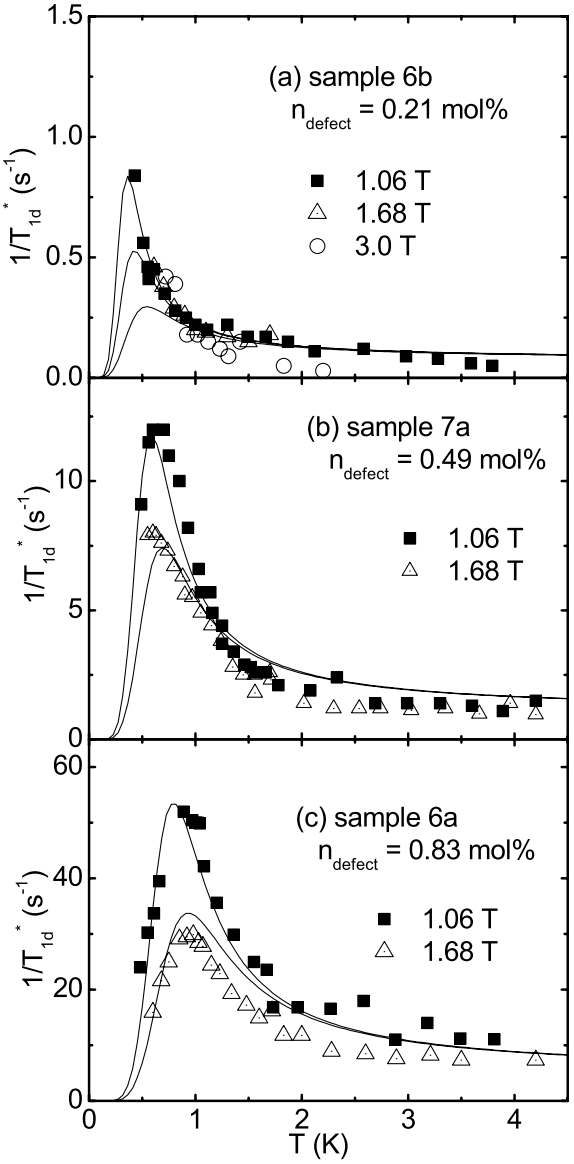

Figure 4.14 $1/T_{1\mathrm{d}}^{*}$ versus temperature T at applied magnetic fields H = 1.06, 1.68, and 3.0 T for the powder samples (a) 6b with $n_{\mathrm{defect}} = 0.21$ mol% (b) 7a with $n_{\mathrm{defect}} = 0.49$ mol% and (c) 6a with $n_{\mathrm{defect}} = 0.83$ mol%. The solid lines are fits to the data by Eqs. (4.17) and (4.19).

interactions have such $1/r^6$ dependences. The authors of Refs. [27] and [28] obtained an expression for the nuclear spin recovery averaged over all the observed nuclear spins and showed that it is indeed a root exponential at long times. In the Appendix, we show that instead of solving for the relaxation curve, we can understand the occurrence of a root exponential relaxation as arising from our calculated probability distribution of nuclear $1/T_1$ values.

In general, one can write the nuclear spin-lattice relaxation rate due to a nearby paramagnetic center as

$$\frac{1}{T_1}(\boldsymbol{r}) = C\frac{f(\theta)}{\overline{f}}r^{-6}, \tag{4.10}$$

where $\boldsymbol{r}$ is the vector connecting the paramagnetic center and nuclear spin, θ is the angle between $\boldsymbol{r}$ and the external field, $\overline{f}$ is the average of the function $f(\theta)$ over all directions, and C is a parameter proportional to the spectral density of spin fluctuations at the nuclear Larmor frequency.[27] $1/T_{1\mathrm{d}}^*$ in Eq. (4.9) is then given by[27, 28]

$$1/T_{1\mathrm{d}}^* = \frac{16\pi^3}{9}(\rho_N n_{\mathrm{defect}})^2 C, \tag{4.11}$$

where ρ_N is the number density of LiV_2O_4 formula units. We will discuss the temperature and field dependences of $1/T_{1\mathrm{d}}^*$ when we study the dynamics of the magnetic defects in Sec. 4.4.6.

4.4.4 Hole Burning Experiment and the Dependence of Relaxation on the Position in the Spectrum

Bloembergen and coworkers[29] have considered the problem of spin diffusion in the frequency domain (spectral diffusion) in a spectrum with the same kind of inhomogeneous broadening as in the first model. The time for a hole to diffuse through the whole spectrum by two-spin mutual spin flip is estimated to be T_2^4/T_2^{*3}, where T_2 is the intrinsic nuclear spin-spin relaxation time and T_2^* is the half width at half maximum of the transient echo signal. In the powder sample 6a ($n_{\mathrm{defect}} = 0.83$ mol%), $T_2 \approx 200$ μs and $T_2^* \approx 5$ μs, so $T_2^4/T_2^{*3} = 32$ s. In the powder sample 6b ($n_{\mathrm{defect}} = 0.21$ mol%), $T_2 \approx 200$ μs and $T_2^* \approx 20$ μs which give $T_2^4/T_2^{*3} = 200$ ms. Both diffusion times are much longer than the values of T_1^* at 4.2 K in each sample in Figs. 4.7 and 4.8, and are thus consistent with the lack of spectral diffusion in Fig. 4.10.

The higher relaxation rates at the wings of the spectrum compared to that at the peak of the spectrum as shown in Fig. 4.11 can also be qualitatively explained by our model. For concreteness of discussion, we assume that the local field is purely dipolar. Denote the angle between the applied magnetic field and the direction from a magnetic defect to a nuclear spin by θ and the distance between the defect and the nuclear spin by r. The NMR frequency shift depends on θ and r through $(1 - 3\cos^2\theta)/r^3$, while the nuclear spin-lattice relaxation rate depends on θ and r through $\sin^2\theta\cos^2\theta/r^6$.[20] The higher relaxation rates observed at the wings compared to that at the peak of the spectrum is due to the monotonic decrease of both the frequency shift and the nuclear spin-lattice relaxation rates with increasing distance r. The nuclear spins with larger frequency shift will also have a higher probability of having larger $1/T_1$ values.

4.4.5 ^{7}Li Nuclear Spin Diffusion

The $p(t)$ of powder sample 6b ($n_{\rm defect} = 0.21$ mol%) in Fig. 4.12(a) deviates from a root exponential decay at $t \gtrsim 100$ ms at $T = 0.61$ K. This can be attributed to the effect of spin diffusion.[30] Spin diffusion tries to establish a common spin temperature (i.e., the same longitudinal magnetization) among nuclear spins at different distances from the defects and results in a single exponential relaxation at long t. Figure 4.15 displays $p(t)$ versus t of the same data as in Fig. 4.12(a) at $T = 0.61$ K, but on a semilog scale, which suggests a single exponential decay at $t \gtrsim 100$ ms. A fit by $p(t) = A\exp(-t/T_1)$ to the data at $t \geq 110$ ms gives $1/T_1 = 1.1$ s^{-1} and $A = 0.86$. The best fit is shown as the straight line in Fig. 4.15.

A crossover from a root exponential to a single exponential decay occurs in the case of diffusion limited relaxation as discussed first by Blumberg in Ref. [30]. The time $t_{\rm c}$, at which the crossover from a root exponential to a single exponential decay takes place, is related to the spin diffusion constant D through[30]

$$t_{\rm c} = C^{1/2}D^{-3/2}, \tag{4.12}$$

where C is defined in Eq. (4.10). The diffusion constant D is related to the rate W of mutual

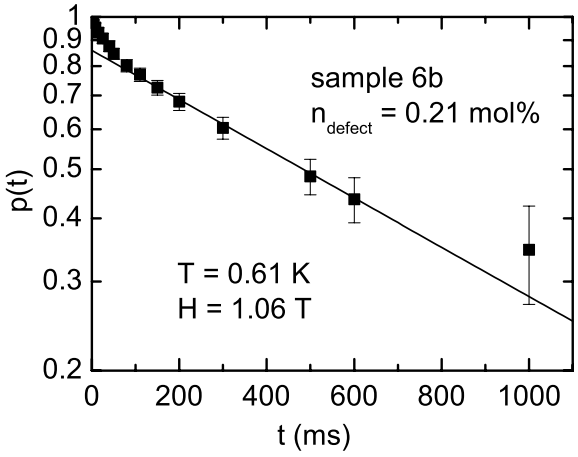

Figure 4.15 Semilog plot of the nuclear spin relaxation function $p(t)$ in Eq. (4.8) versus time t after saturation for powder sample 6b with $n_{\rm defect} = 0.21$ mol% at $H = 1.06$ T and $T = 0.61$ K. The straight line is a single exponential fit to the data at $t \geq 110$ ms.

flips of nearest neighbor nuclear spins through[20]

$$D = Wa^2, \tag{4.13}$$

where a is the distance between the two spins. The rate of the single exponential decay at long times in Fig. 4.15 is given by[30]

$$\frac{1}{T_1} = 8.5\rho_N n_{\rm defect} C^{1/4} D^{3/4}, \tag{4.14}$$

where ρ_N is the density of LiV_2O_4 formula units.

In order to confirm the spin diffusion interpretation, below we will show that the estimated crossover time $t_{\rm c}$ and $1/T_1$ are of the same order of magnitude as the observed $t_{\rm c} \sim 100$ ms and $1/T_1 = 1.1$ s^{-1}, respectively. The mutual spin-flip is due to nuclear dipolar interactions and the value of W can be estimated using Fermi's golden rule. For nuclear spins having $I = 1/2$, after averaging over the angular dependence, one obtains[20]

$$W = \frac{2}{5}\pi \frac{\gamma_{\rm n}^4 \hbar^2}{4a^6} \rho(0), \tag{4.15}$$

where $\rho(0)$ is the spectral density of the two spin system at zero Zeeman energy and $\gamma_{\rm n}$ is the gyromagnetic ratio of the nuclear spins. The ^{7}Li nuclei have spin $I = 3/2$, but an expression

for W when $I = 3/2$ is not available, and the above equation for W should provide at least a rough estimate of W. Approximating $\rho(0)$ by $1/\sqrt{2\pi\langle\Delta\omega^2\rangle}$,[20] where $\langle\Delta\omega^2\rangle = 288$ kHz^2 is the Van Vleck second moment of the ^{7}Li nuclei,[23] and taking $a = 3.57$ Å, which is the nearest-neighbor ^{7}Li-^{7}Li distance in LiV_2O_4, we find $W = 46\,\mathrm{s}^{-1}$ from Eq. (4.15) and $D = 5.9 \times 10^{-14}\mathrm{cm}^2/\mathrm{s}$ from Eq. (4.13).

The value of C in Eq. (4.12) can be obtained from Eq. (4.11) where $1/T_{1\mathrm{d}}^*$ is measured using Eq. (4.9) from the initial root exponential part of $p(t)$ in Fig. 4.12(a) for powder sample 6b. At $T = 0.61$ K and $H = 1.06$ T, one obtains $1/T_{1\mathrm{d}}^* = 0.7\ \mathrm{s}^{-1}$, so one has $C = 1.4 \times 10^{-41}\ \mathrm{cm}^6\ \mathrm{s}^{-1}$. Using the above $D = 5.9 \times 10^{-14}\ \mathrm{cm}^2/\mathrm{s}$ and $n_{\mathrm{defect}} = 0.21$ mol%, Eq. (4.12) yields the crossover time $t_{\mathrm{c}} = 220$ ms and Eq. (4.14) yields long time decay rate $1/T_1 = 1.9\ \mathrm{s}^{-1}$. Due to the uncertainty in our estimate of the parameter D and the approximate nature of Eq. (4.12), the estimated t_{c} and $1/T_1$ values should be considered to be consistent with the observed $t_{\mathrm{c}} \sim 100$ ms and $1/T_1 = 1.1\ \mathrm{s}^{-1}$, respectively.

The absence of a deviation from root exponential behavior in samples 7a ($n_{\mathrm{defect}} = 0.49$ mol%) and 6a ($n_{\mathrm{defect}} = 0.83$ mol%) as shown in Figs. 4.12(b) and (c) may be due to the effect of inhomogeneous broadening, which decreases the probability of overlap of Zeeman level splittings of neighboring ^{7}Li nuclei and results in a decrease in the spin diffusion constant D. Furthermore, due to the higher concentrations of the defects, values of $p(t)$ at $t \gtrsim 100$ ms in these two samples are much smaller than in the 0.21 mol% sample, making such a deviation more difficult to observe.

4.4.6 Magnetic Defect Spin Dynamics

In this section, we discuss the relation of the nuclear spin-lattice relaxation rate to the dynamics of the magnetic defects in the powder samples. In the weak collision limit $h \ll H$, where h is the magnitude of the local fluctuating field at the nuclear site, the nuclear spin-lattice relaxation rate $1/T_1$ due to an electronic magnetic defect spin at the origin is given by[20]

$$\frac{1}{T_1}(\boldsymbol{r}) = \frac{1}{\hbar^2} \sum_{\alpha=x,y,z} A_\alpha^2(\boldsymbol{r}) \int_{-\infty}^{\infty} \langle S_\alpha(0) S_\alpha(t) \rangle \exp(i\omega_{\mathrm{n}} t) dt, \tag{4.16}$$

where $\boldsymbol{r}$ is the position of the nuclear spin with respect to the magnetic defect, $A_\alpha(\boldsymbol{r})$ is the hyperfine coupling constant between the nuclear spin and a magnetic defect, $\omega_{\rm n} = H\gamma_{\rm Li}$, and $\langle S_\alpha(0)S_\alpha(t)\rangle$ $(\alpha = x, y, z)$ are the magnetic defect spin autocorrelation functions.

As indicated in the ac susceptibility measurements, the peaks in $1/T_{1\rm d}^*$ versus T are related to spin freezing of the magnetic defects. As a first attempt, we assume a single exponential decay for the magnetic defect spin autocorrelation functions and assume that the freezing process is due to an energy barrier so that the correlation time τ follows

$$\tau = \tau_0 \exp\left(\frac{\Delta}{T}\right), \tag{4.17}$$

where τ_0 is the fluctuation rate of the paramagnetic defects at high temperature and Δ is the energy barrier in temperature units. For simplicity, we will assume that all the magnetic defect spins in a sample have the same correlation time τ. For dipolar or RKKY interactions, the nuclear spin-lattice relaxation rate of a ^{7}Li nucleus due to a nearby defect at distance r is[20]

$$\frac{1}{T_1}(r) = \frac{2R\mu_{\rm B}^2\gamma_{\rm Li}^2 S(S+1)}{5r^6}\frac{\tau}{1+\omega_{\rm n}^2\tau^2}, \tag{4.18}$$

where the angular dependence is ignored and the prefactor is written in such a way that $R = 1$ would correspond to relaxation due solely to the fluctuating dipolar field of the longitudinal component of the magnetic defect spin. The presence of additional relaxation channels would increase the value of R. Combining Eqs. (4.11) and (4.18), the measured relaxation rates $1/T_{1\rm d}^*$ can be written as

$$\frac{1}{T_{1\rm d}^*} = R\frac{32\pi^3}{45}\mu_{\rm B}^2\gamma_{\rm Li}^2 S(S+1)\rho_N^2 n_{\rm defect}^2\frac{\tau}{1+\omega_{\rm n}^2\tau^2}. \tag{4.19}$$

At high temperatures, τ is generally much shorter than the inverse of the nuclear Larmor frequency $1/\omega_{\rm n}$. As τ increases with decreasing temperature T, a peak appears in $1/T_{1\rm d}^*$ versus T at the temperature where $\tau = 1/\omega_{\rm n}$.

We fit the $1/T_{1\rm d}^*$ data in Fig. 4.14 on all three powder samples simultaneously by the combination of Eqs. (4.17) and (4.19). Possible field and temperature dependences of the parameter R are ignored in the fit. There are seven free parameters in the fit, R and Δ for each sample and τ_0 which is assumed to be sample independent. The fitting results are displayed in Fig. 4.14 by the solid curves. The best fit value of τ_0 is 4.1×10^{-10} s and the best fit

Table 4.2 Best fit values of prefactor R and energy barrier Δ obtained through fitting $1/T_{1\,\mathrm{d}}^{*}$ data in Fig. 4.14 by a combination of Eqs. (4.17) and (4.19). In order to see the correlation between defect concentrations and R and Δ, the values of n_{defect} and $n_{\mathrm{defect}}\sqrt{S(S+1)}$ are also listed.

Sample	n_{defect} (mol%)	$n_{\mathrm{defect}}\sqrt{S(S+1)}$ (mol%)	R	Δ (K)
6b	0.21	0.85	0.04(4)	1.1(1)
7a	0.49	1.9	0.17(6)	1.8(2)
6a	0.83	3.6	0.24(4)	2.5(2)

values of R and Δ for each sample are listed in Table 4.2. The energy barrier Δ increases with increasing concentration of magnetic defects, which indicates that the dynamic slowing down with decreasing temperature originates from the interaction between the magnetic defects. Interaction between magnetic defects should increase with increasing concentration of the magnetic defects since the average nearest-neighbor distance decreases.

The values of R in all three samples are much less than unity, a fact which cannot be explained by the presence of other nuclear spin-lattice relaxation mechanisms since additional relaxation mechanisms would increase R. Such small values of R might be related to the spin-glass like freezing as observed in the ac magnetic susceptibility measurements. In spin glass systems, the spin autocorrelation functions are highly nonexponential,[31, 32] which reduces the spectral density of the magnetic defect spin fluctuations at ω_{n} as compared to the Lorentzian in Eq. (4.19). The reduction in spectral density thus results in a reduction in the fitted value of R in Eq. (4.19).

4.5 Discussion and Conclusions

Our study shows that there can be different kinds of magnetic defects in the LiV_2O_4 system. As shown by the nuclear spin lattice relaxation rates and ac magnetic susceptibility measurements at 14 MHz, the magnetic defects in the powder samples undergo a spin glass-like freezing below 1 K, while the magnetic defects in the single crystals exhibit a different behavior at such low temperatures. The magnetic defects present in the powder LiV_2O_4 samples in Ref. [13] are similar to the magnetic defects in our powder samples since they

show similar temperature dependences of $1/T_1^*$. The different kinds of magnetic defects must be associated with different types of structural defects in the system, which result in different coupling between the defects and the conduction electrons and thus give rise to different ground states of the defects. Different types of magnetic defects were also found in an annealing study of the magnetic defects in single crystals,[17] where heat treatment at 700 °C was found to remove the magnetic defects in one but not other single crystals.

Our model gives a sufficient description of most of our NMR results. This model assumes (i) a random distribution of magnetic point defects and (ii) that the heavy Fermi liquid in magnetically pure LiV_2O_4 survives in samples containing up to ~ 0.8 mol% magnetic defects. This model can explain the inhomogeneous broadening of the ^{7}Li NMR spectrum, the nonexponential nuclear spin-lattice relaxation versus time behavior, and the lack of spectral diffusion in the hole burning experiments. It can also explain the smaller nuclear spin lattice relaxation rate at the peak of the spectrum as compared to that at the wings. However, it is hard to reconcile the picture of magnetic point defects with the high magnetic moments for the defects (spins of 3–4) deduced here (see Table 4.1) and in Refs. [14] and [17] from magnetization measurements. Thus one cannot rule out the possibility that the magnetic defects are associated with magnetic droplets with a distribution of sizes.

Thus our analysis of our NMR data indicates that the Fermi liquid is still preserved even in the presence of magnetic defects in the powder samples. However in the single crystals, the Fermi liquid property might be modified by its coupling to the magnetic defects at $T < 1.3$ K. Other measurements at low temperatures ($T < 1.5$ K) are needed in order to further understand the nature of the electronic state in the single crystals with magnetic defects. In addition, static and low frequency ac susceptibility studies are desired to further confirm the spin glass freezing in the powder samples.

Acknowledgements

We are grateful to B. J. Suh for numerous beneficial suggestions. Work at the Ames Laboratory was supported by the Department of Energy-Basic Energy Sciences under Contract

No. DE-AC02-07CH11358.

Appendix

In this appendix, we show that the probability distribution of $1/T_1$ due to dipolar interaction of nuclear spins with dilute magnetic defects corresponds to the $1/T_1$ distribution underlying a root exponential relaxation in Eq. (4.5) with $\beta = 1/2$, which is given by (with $s \equiv T_{1\mathrm{d}}^*/T_1$)[26]

$$P(s, 1/2) = \frac{e^{-\frac{1}{4s}}}{\sqrt{4\pi} s^{3/2}}. \tag{4.20}$$

This distribution is proportional to $s^{-3/2}$ for large s, and has a low-s cutoff since $e^{-1/4s}$ rapidly approaches zero at small s values. The $s^{-3/2}$ dependence of the $1/T_1$ distribution follows from a r^{-6} dependence of $1/T_1$ as in Eq. (4.10) as follows. Ignoring the angular dependence in Eq. (4.10), in the single paramagnetic center limit, the distribution of s arising from such a geometric distribution with a continuum description of nuclear spins around a magnetic defect is

$$P_{\mathrm{geo}}(s) \propto r^2 \frac{\mathrm{d}r}{\mathrm{d}s}\Big|_{r=\left(\frac{CT_{1\mathrm{d}}^*}{s}\right)^{\frac{1}{6}}} \propto s^{-\frac{3}{2}}. \tag{4.21}$$

This distribution diverges as $1/T_1$ approaches zero. This divergence is caused by the single impurity approximation. Nuclei with $1/T_1$ approaching zero correspond to those far away from the paramagnetic center. Due to the finite distance between different paramagnetic centers, the probability of finding a nuclear spin with $1/T_1 \to 0$ should instead vanish, so a low $1/T_1$ cutoff has to be applied, resulting in a distribution function well approximated by Eq. (4.20) and observation of a root exponential relaxation behavior.

The above qualitative arguments are supported by the following numerical simulation. In the simulation, we calculated the $1/T_1$ distribution of ^{7}Li nuclei due to a random distribution of dilute paramagnetic defects in the LiV_2O_4 spinel structure. The defects randomly occupy the vanadium sites with a probability of 0.25% ($n_{\mathrm{defect}} = 0.5$ mol%) and the configuration of the random defects repeats every 80 unit cells in all crystallographic axis directions. The $1/T_1$

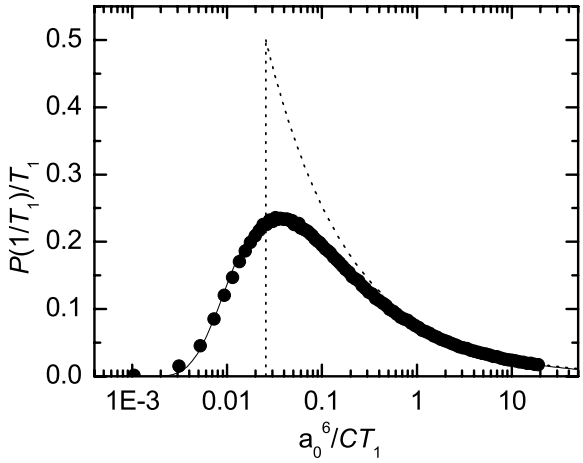

Figure 4.16 $1/T_1$ probability distributions $P(1/T_1)$, normalized by T_1, due to dilute point-like paramagnetic defects. The circles are results obtained from computer simulation. The solid line is the best fit by Eq. (4.20) with $1/T_1^* = 0.067(1)$ s^{-1} and the dotted line is a plot of $p(x) = 0.8x^{-3/2}$ with a small x cutoff $x_c = 0.0256$, where $x \equiv a_0^6/CT_1$. The lower cutoff is chosen so that $\int_{x_c}^{\infty} P(x)\,dx = 1$.

of each ^{7}Li nucleus is calculated using[20]

$$\frac{1}{T_1} = C \sum_i \frac{15 \sin^2\theta_i \cos^2\theta_i}{2} \frac{1}{r_i^6}, \tag{4.22}$$

where r_i is the distance between paramagnetic center i and the ^{7}Li nucleus and θ_i is the angle between the applied magnetic field and the vector from paramagnetic center to the ^{7}Li nucleus. The applied magnetic field was arbitrarily chosen to be along the $\langle 001 \rangle$ direction. Equation (4.22) has the same angular and distance dependences as the nuclear spin-lattice relaxation due to the dipolar field fluctuation from the longitudinal spin component of the paramagnetic defects.[20] In the presence of a strong applied magnetic field, the transverse spin fluctuation is often modulated by the Larmor frequency of the electronic spins and thus has negligible contribution to $1/T_1$.[20] The summation over i in Eq. (4.22) includes all defects with $r_i < 20a_0$, where $a_0 = 8.24$ Å is the lattice constant of LiV_2O_4. It was checked that changing the summation range to $r_i < 10a_0$ gave negligible difference in the final $1/T_1$ distribution.

The distribution of $1/T_1$ resulting from the above simulation is displayed as the circles in Fig. 4.16. The simulated $1/T_1$ distribution can be fitted very well by Eq. (4.20) with

$1/T_{1d}^* = 0.067(1)C/a_0^6$, as shown by the solid curve in Fig. 4.16. $1/T_{1d}^*$ calculated from Eq. (4.11) is equal to $0.088C/a_0^6$, close to the simulated result. The difference may be due to the neglected angular dependence in deriving Eq. (4.11). For comparison, a simple power law distribution $P(x \equiv a_0^6/CT_1) = 0.8x^{3/2}$ with a small x cutoff of $x_c = 0.0256$ is also displayed in Fig. 4.16. The prefactor 0.8 is chosen to make the distribution overlap with the simulated result at large x and the cutoff $x_c = 0.0256$ is determined by the normalization condition $\int_{x_c}^{\infty} P(x)\,dx = 1$.

References

[1] S. Kondo, D. C. Johnston, C. A. Swenson, F. Borsa, A. V. Mahajan, L. L. Miller, T. Gu, A. I. Goldman, M. B. Maple, D. A. Gajewski, E. J. Freeman, N. R. Dilley, R. P. Dickey, J. Merrin, K. Kojima, G. M. Luke, Y. J. Uemura, O. Chmaissem, and J. D. Jorgensen, Phys. Rev. Lett. **78**, 3729 (1997).

[2] G. R. Stewart, Rev. Mod. Phys. **56**, 755 (1984).

[3] H. Takagi, C. Urano, S. Kondo, M. Nohara, Y. Ueda, T. Shiraki, and T. Okubo, Mater. Sci. Eng. B **63**, 147 (1999).

[4] C. Urano, M. Nohara, S. Kondo, F. Sakai, H. Takagi, T. Shiraki, and T. Okubo, Phys. Rev. Lett. **85**, 1052 (2000).

[5] K. Kadowaki and W. B. Woods, Solid State. Commun. **71**, 1149 (1989).

[6] P. Fulde, J. Phys.: Condens. Matter **16**, S591 (2004).

[7] R. Arita, K. Held, A. V. Lukoyanov, and V. I. Anisimov, Phys. Rev. Lett. **98**, 166402 (2007).

[8] V. Yushankhai, A. Yaresko, P. Fulde, and P. Thalmeier, Phys. Rev. B **76**, 085111 (2007).

[9] A. V. Mahajan, R. Sala, E. Lee, F. Borsa, S. Kondo, and D. C. Johnston, Phys. Rev. B **57**, 8890 (1998).

[10] D. C. Johnston, J. Low Temp. Phys. **25**, 145 (1976).

[11] M. Dalton, D. P. Tunstall, J. Todd, S. Arumugam, and P. P. Edwards, J. Phys.: Condens. Matter **6**, 8859 (1994).

[12] D. C. Johnston, S.-H. Baek, X. Zong, F. Borsa, J. Schmalian, and S. Kondo, Phys. Rev. Lett. **95**, 176408 (2005).

[13] H. Kaps, M. Brando, W. Trinkl, N. Büttgen, A. Loidl, E.-W. Scheidt, M. Klemm, and S. Horn, J. Phys.: Condens. Matter **13**, 8497 (2001).

[14] S. Kondo, D. C. Johnston, and L. L. Miller, Phys. Rev. B **59**, 2609 (1999).

[15] M. D. Vannette, A. Safa-Sefat, S. Jia, S. A. Law, G. Lapertot, S. L. Bud'ko, P. C. Canfield, J. Schmalian, and R. Prozorov, J. Mag. Mag. Mater. (2007), in press.

[16] S. Das, X. Ma, X. Zong, A. Niazi, and D. C. Johnston, Phys. Rev. B **74**, 184417 (2006).

[17] S. Das, X. Zong, A. Niazi, A. Ellern, J. Q. Yan, and D. C. Johnston, Phys. Rev. B **76**, 054418 (2007).

[18] D. Corson and P. Lorrain, *Introduction to Electromagnetic Fields and Waves* (W. H. Freeman and Company, San Francisco, 1962).

[19] E. Fukushima and S. B. W. Roeder, *Experimental Pulse NMR: A Nuts and Bolts Approach* (Perseus Books, Cambridge, 1981).

[20] A. Abragam, *Principles of Nuclear Magnetism* (Oxford University Press, Oxford, 1982).

[21] J. H. Van Vleck, Phys. Rev. **74**, 1168 (1948).

[22] L. E. Drain, Proc. Phys. Soc. London **80**, 1380 (1962).

[23] M. Onoda, H. Imai, Y. Amako, and H. Nagasawa, Phys. Rev. B **56**, 3760 (1997).

[24] C. P. Slichter, *Principles of Magnetic Resonance* (Springer, Berlin, 1990), 3rd ed.

[25] R. E. Walstedt and L. R. Walker, Phys. Rev. B **9**, 4857 (1974).

[26] D. C. Johnston, Phys. Rev. B **74**, 184430 (2006).

[27] M. R. McHenry, B. G. Silbernagel, and J. H. Wernick, Phys. Rev. B **5**, 2958 (1972).

[28] D. Tse and S. R. Hartmann, Phys. Rev. Lett. **21**, 511 (1968).

[29] N. Bloembergen, S. Shapiro, P. S. Pershan, and J. O. Artman, Phys. Rev. **114**, 445 (1959).

[30] W. E. Blumberg, Phys. Rev. **119**, 79 (1960).

[31] A. T. Ogielski, Phys. Rev. B **32**, 7384 (1985).

[32] A. P. Murani, J. Magn. Magn. Mater. **22**, 271 (1981).

CHAPTER 5. ^{17}O and ^{51}V NMR Study of the Frustrated Zig-Zag Spin-1 Chain Compound CaV_2O_4

(This chapter is based on an article submitted to Phys. Rev. B by X. Zong, B. J. Suh, A. Niazi, J. Q. Yan, D. L. Schlagel, T. A. Lograsso, and D. C. Johnston)

Abstract

^{51}V NMR studies on CaV_2O_4 single crystals and ^{17}O NMR studies on ^{17}O-enriched powder samples are reported. The temperature dependences of the ^{17}O NMR line width and nuclear spin-lattice relaxation rate give strong evidence for a long-range antiferromagnetic transition at $T_N = 78$ K in the powder. Magnetic susceptibility measurements show that $T_N = 69$ K in the crystals. A zero-field ^{51}V NMR signal was observed at low temperatures ($f \approx 237$ MHz at 4.2 K) in the crystals. The field swept spectra with the field in different directions suggest the presence of two antiferromagnetic substructures. Each substructure is collinear, with the easy axes of the two substructures separated by an angle of 19(1)°, and with their average direction pointing approximately along the b-axis of the crystal structure. The two spin substructures contain equal number of spins. The temperature dependence of the ordered moment, measured up to 45 K, shows the presence of an energy gap E_G in the antiferromagnetic spin wave excitation spectrum. Antiferromagnetic spin wave theory suggests that E_G/k_B lies between 64 and 98 K.

5.1 Introduction

Frustrated magnetic systems have attracted a lot of research interest because such systems often exhibit interesting low temperature properties.[1] The zig-zag spin chain with antiferro-

magnetic interactions between nearest- and next-nearest-neighbors is about the most simple frustrated system. In a zig-zag spin chain system with spin $S = 1$, the ground state phase diagram (at temperature $T = 0$) as a function of XXZ anisotropy and ratio between nearest-neighbor (NN) and next-nearest-neighbor (NNN) interactions exhibits six different phases.[2, 3] In addition to two Néel ordered phases and two phases with a Haldane gap, there exists a large phase region called a gapless chiral phase where the chirality exhibits long range order without accompanying spin order, and a small phase region where there is a gapped chiral phase.

CaV_2O_4 is a possible candidate for a zig-zag spin $S = 1$ chain system.[4, 5] It has an orthorhombic crystal structure (space group *Pnam*) at room temperature. Vanadium moments at two crystallographically inequivalent sites respectively form two inequivalent zig-zag spin chains along the *c*-axis. In one of the two chains, the distances between NN and NNN vanadium atoms are 3.01 and 3.08 Å, respectively, while in the other chain, these two distances are 3.01 and 3.06 Å, respectively. The smallest interchain vanadium distances are 3.58 and 3.62 Å.[6] Thus one might expect a much smaller interchain coupling as compared to NN and NNN interactions within the chain.

Previous magnetization and ^{51}V NMR studies of CaV_2O_4 suggested that the ground state of the system might be a gapless chiral phase.[4, 5] However, this finding contradicts earlier powder neutron diffraction studies which showed that the system is in an antiferromagnetic state at 4.2 K.[7] The neutron measurements indicated a magnetic unit cell in which the *b* and *c* lattice constants are doubled and the spin directions in each chemical unit cell are reversed relative to their orientations in neighboring chemical unit cells along the *b*- and *c*-axes. Each chemical unit cell contains 8 vanadium spins and the magnetic spin structure within each chemical unit cell could not be uniquely determined. The neutron diffraction pattern was found to be consistent with three different collinear models with spins parallel to the *b*-axis. By assuming the same spin moment at all vanadium sites, the magnetic moment of each vanadium spin was determined to be 1.06(6) μ_B, only about half the value expected for a vanadium spin with *g*-factor $g \approx 2$ and $S = 1$.[7] The presence of a low temperature antiferromagnetic phase is also supported by recent magnetization measurements on annealed

CaV_2O_4 single crystals, which showed a clear signature of an antiferromagnetic phase transition at temperature $T_N = 69$ K.[6]

In order to obtain further evidence of the magnetic phase transition and to study the magnetic properties in the ordered state, we performed ^{17}O and ^{51}V NMR studies on ^{17}O-enriched powder and single crystal samples, respectively. The ^{17}O NMR spectrum and the nuclear spin-lattice relaxation rate measurements give strong evidence for a magnetic transition at $T_N = 78$ K in the powder sample. In contrast to early ^{51}V NMR measurements,[4, 5] we could not detect a ^{51}V NMR signal in the powder sample around the normal Larmor frequency in an applied field of 1.67 T in the temperature range of 4.2 K $< T <$ 296 K. Instead, we observed a *zero-field* ^{51}V NMR signal at $T < 45$ K ($f \approx 237$ MHz at 4.2 K).

The zero-field ^{51}V NMR signal is observed because of a strong local field at ^{51}V nuclear sites ($H_{loc} = 21.2$ T at 4.2 K) in the ordered state. The local field arises mainly from interaction between nuclei and vanadium core electrons, which are polarized by the ordered $3d$ electronic spins.[8, 9] This local field points antiparallel to the direction of the local electronic spin moment. By studying how the resonance frequency changes as a function of the direction and magnitude of the applied magnetic field, one can obtain information on the vanadium spin structure, as will be demonstrated below. We measured the temperature dependence of the ordered moment to study the anisotropy gap of the antiferromagnetic spin wave excitations. We also attempted to measure the temperature dependence of the ^{51}V nuclear spin-lattice relaxation rate $1/T_1$. However, due to the very broad line and the presence of nuclear quadrupole splitting (the nuclear spin of ^{51}V is $I = 7/2$), the relaxation curves are highly nonexponential and depend strongly on the saturation condition. Thus, a reliable measurement of the ^{51}V $1/T_1(T)$ was not achieved.

The remainder of the chapter is organized as follows. Experimental details are explained in Sec. 5.2. ^{17}O and ^{51}V NMR results are presented in Secs. 5.3 and 5.4, respectively. In Sec. 5.5, we give a summary of the main results of the chapter.

5.2 Experimental Details

Polycrystalline single phase CaV_2O_4 (sample an-2-116) was synthesized via the solid-state route by reacting V_2O_3 (99.995%, MV Labs) with CaO obtained by calcining $CaCO_3$ (99.995%, Aithaca Chemicals) at 1100 °C. The chemicals were ground inside a He glove-box, then pressed and sintered at 1200 °C for 96 hours in flowing 4.5% H_2-He with intermediate grindings. Phase purity was confirmed by powder X-ray diffraction (XRD) on a Rigaku Geigeflex diffractometer using Cu Kα radiation in the 2θ range of 10°–90°.[6] 72.1 atomic% ^{17}O-enriched oxygen (MSD Isotopes) was used for ^{17}O-enrichment. About 1 g of the precursor CaV_2O_4 was placed in a Pt foil-lined alumina boat in an evacuated furnace tube, which was then preheated to 750 °C under dynamic vacuum. The pumping line was then closed and the tube backfilled with the ^{17}O-enriched O_2. The mass gain on oxidation indicated a nominal composition of $CaV_2O_{5.94}$. This was placed in flowing 4.5% H_2-He and reduced as before to CaV_2O_4 (sample an-2-180E). The final ^{17}O content of the enriched CaV_2O_4 was about 25%. Powder XRD was used to confirm that the sample was single phase.

^{17}O NMR measurements were performed utilizing a phase-coherent pulse spectrometer in applied fields of 3.0 and 4.7 T. The typical $\pi/2$ pulse length is 6 μs. The echo signal was produced by a sequence of a $\pi/2$ and a $\pi/3$ pulse, which produce the maximum echo signal intensity. The separation between these two echo generating pulses was 40 μs. The ^{17}O NMR spectra were measured by either Fourier transform of half the echo signal or by plotting the area of the echo as a function of the rf frequency (frequency sweep). The nuclear spin-lattice relaxation rates were measured by monitoring the recovery of the echo intensity following a comb sequence of $\pi/2$ saturation pulses. Static magnetization versus temperature was measured in a Quantum Design SQUID magnetometer in a field of 1 T and in the temperature range 5–100 K to confirm the low temperature magnetic behavior and the ordering temperature $T_N = 78$ K. The magnetic susceptibility of the powdered ^{17}O-enriched sample is shown in Fig. 5.1. The transition temperature is revealed by a small kink in the $\chi(T)$ data at T_N.

Two CaV_2O_4 crystals were used in ^{51}V NMR measurements. Crystal #1 was grown in an optical floating zone furnace while crystal #2 was grown using a tri-arc crystal pulling

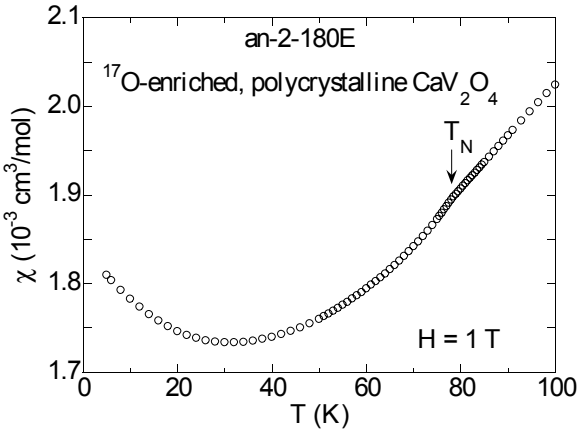

Figure 5.1 Magnetic susceptibility χ versus temperature T of the ^{17}O-enriched CaV_2O_4 powder sample measured in a field of $H = 1$ T. The vertical arrow indicates the position of the antiferromagnetic transition temperature $T_N = 78$ K.

method.[6, 10] Both crystals were annealed at 1200 °C under 4.5% H_2-He flow and the antiferromagnetic phase transition temperatures of the annealed crystals were found from magnetic susceptibility and heat capacity measurements to be 69 K.[6] The sizes of the crystals #1 and #2 are about $5 \times 5 \times 10$ mm^3 and $1 \times 1 \times 2$ mm^3, respectively. The magnetic susceptibility of crystal #2 is shown in Fig. 5.2 with the field along a and b directions. The antiferromagnetic transition temperature T_N is clearly seen as a bifurcation in the susceptibilities along the two directions. We note that, when the field is along the b direction, a splitting between zero-field-cooled and field-cooled susceptibility is observed below $T = 20$ K.

A search for a zero-field ^{51}V NMR echo signal was performed at 4.2 K and was found to be located close to a frequency of 237 MHz at that temperature. The echo was produced by a sequence of two pulses with the same pulse length, which was typically 4 μs and about half the length a $\pi/2$ pulse. The separation between the pulses was fixed to 16 μs. ^{51}V NMR spectra were measured by plotting the echo intensity as a function of the magnetic field. A variable magnetic field from 0 to 2.0 T was produced by an electromagnet. The value of the magnetic field was measured by a Hall magnetometer attached to one of the two magnet pole caps. The difference between the measured field and the field at the position of the sample (measured by the resonance frequency of protons in water) was less than 0.005 T over the whole field

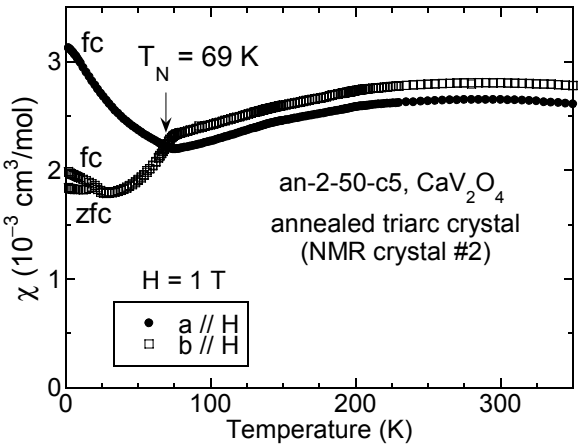

Figure 5.2 Magnetic susceptibility χ versus temperature T of CaV_2O_4 crystal #2 measured with the applied field $H = 1$ T along the a and b directions. The vertical arrow indicates the antiferromagnetic transition temperature $T_N = 69$ K. The measurements were carried out under either field-cooled (fc) or zero–field-cooled (zfc) conditions, as indicated.

range. Individually, the crystals were placed inside copper solenoid coils with the crystal c-axis parallel to the coil axis. Measurements of crystal #1 involved rotation of the field in the a-b and b-c planes. Measurements of crystal #2 involved rotation of the field in the a-b plane. The rotation of the field was achieved by rotating the cryostat together with the crystal about the crystallographic axes perpendicular to the field plane. The misalignment between the rotation axis and the intended crystallographic axis is estimated to be less than 5°.

5.3 ^{17}O NMR in Powder Sample of CaV_2O_4

Figure 5.3 displays the ^{17}O NMR spectra for the ^{17}O-enriched powder sample of CaV_2O_4 in $H = 3$ T at three different temperatures. The spectrum at $T = 296$ K was obtained via Fourier transform of half the echo signal while the spectra at $T = 80$ and 77 K were obtained by frequency sweep. ^{17}O nuclei have spin 5/2 and thus possess a nonzero electric quadrupole moment. Since the local environments of all oxygen sites do not possess cubic symmetry (point group m), one expects a quadrupole splitting of the ^{17}O resonance frequencies. We attribute the lack of a powder pattern of the first order quadrupole splitting in the observed spectra to a smaller quadrupole splitting compared to the magnetic broadening of the spectra. The

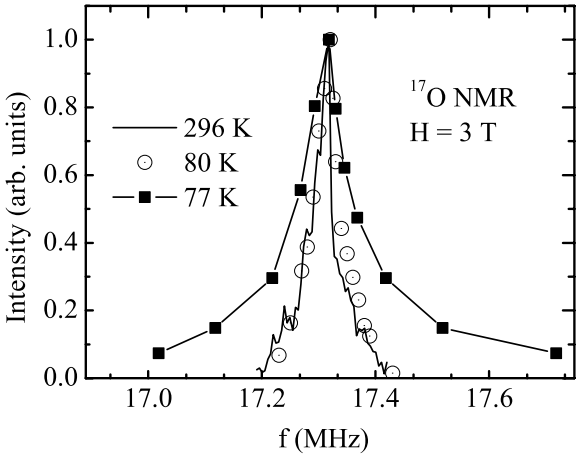

Figure 5.3 Absorption spectrum of the ^{17}O NMR signal for an ^{17}O-enriched powder sample of CaV_2O_4 at three different temperatures in an applied magnetic field $H = 3.0$ T. A strong inhomogeneous broadening is observed close to the magnetic transition temperature $T_N = 78$ K. The solid line at 77 K is a guide to the eye.

absorption line at $T = 77$ K exhibits large broadening compared to the lines at $T = 80$ and 296 K. As will be further shown below, this broadening is a signature of an antiferromagnetic phase transition at $T_N = 78$ K, where the nuclear spin-lattice relaxation rate $1/T_1$ exhibits a peak. As the temperature approaches the phase transition temperature, the electronic vanadium spins slow down dramatically and thus induce an inhomogeneous static (on the NMR time scale) dipolar field on neighboring ^{17}O sites and broaden the ^{17}O NMR line.

The recovery of the ^{17}O longitudinal nuclear magnetization $M(t)$ following the saturation pulses is a single exponential function at $T > 100$ K. Below 100 K, deviation from single exponential behavior is observed, indicating a distribution of $1/T_1$ values. In order to extract a characteristic relaxation rate at all temperatures, we fitted the recovery curves to a stretched exponential function

$$1 - \frac{M(t)}{M(\infty)} = \exp\left[-(t/T_1^*)^\beta\right]. \tag{5.1}$$

The relation of the parameters $1/T_1^*$ and β to the $1/T_1$ distribution underlying a stretched exponential function has been discussed in a recent paper.[11] Figure 5.4 shows the temperature dependence of $1/T_1^*$ and β in $H = 3.0$ and 4.7 T. At $T > 100$ K, the relaxation rate is almost

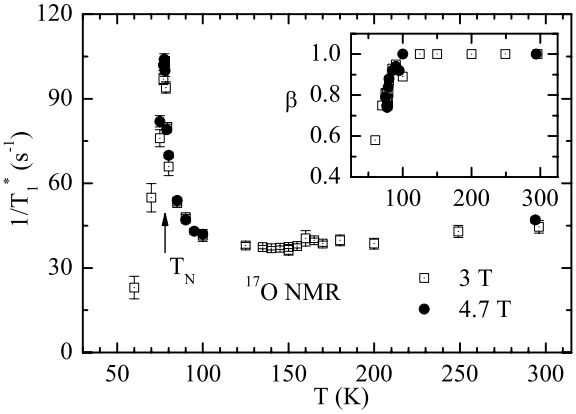

Figure 5.4 Temperature T dependence of the ^{17}O nuclear spin-lattice relaxation rate $1/T_1^*$ [see Eq. (5.1)] of ^{17}O-enriched powder CaV_2O_4 in applied magnetic fields $H = 3.0$ and 4.7 T. A strong peak is observed close to the antiferromagnetic transition temperature $T_N = 78$ K, as labeled by the arrow. Inset: the stretching exponent β versus T.

temperature independent. Below 100 K, $1/T_1^*$ exhibits a strong enhancement and reaches a peak at $T_N = 78$ K. Combining the above NMR results with magnetization studies of powder and single crystals,[6] and with the magnetic susceptibility data in Fig. 5.1, we identify the $1/T_1^*$ peak temperature as the temperature of an antiferromagnetic phase transition T_N. The peak in the nuclear spin-lattice relaxation rate at T_N results from an enhancement and slowing down of the electronic spin fluctuations at wave vectors close to the antiferromagnetic ordering vector as the temperature approaches T_N from either side.[12]

5.4 ^{51}V NMR Below T_N in single crystals of CaV_2O_4

5.4.1 Spin Structure at 4.2 K

In an external magnetic field $\boldsymbol{H}$, the resonance frequency f of the ^{51}V nuclear spins is given by

$$f = |A\langle \boldsymbol{S} \rangle + \boldsymbol{H}|\gamma_v/2\pi, \tag{5.2}$$

where A is the hyperfine coupling constant between the nuclear spin and the vanadium electronic spins $\boldsymbol{S}$, γ_v is the gyromagnetic ratio of ^{51}V nuclear spins, and $\langle \boldsymbol{S} \rangle$ denotes the average electronic spin value in thermal equilibrium. In our experiments, the local field is much larger

than the applied field: $A|\langle \boldsymbol{S} \rangle| \gg H$. Depending on whether the applied field component along $\langle \boldsymbol{S} \rangle$ is parallel or antiparallel to $\langle \boldsymbol{S} \rangle$, the resonance frequency shifts to higher or lower values, respectively. If CaV_2O_4 is a collinear antiferromagnet at low temperatures, where opposite spin directions exist, upon application of an external field along the ordering axis, the zero-field spectrum should split into two peaks. These peaks should be symmetrically displaced above and below the zero-field peak frequency.

Figure 5.5 shows the field-swept spectra with the field at different angles in the a-b plane, measured with rf frequencies both higher and lower than the zero-field peak frequency $f_0 =$ 236.7 MHz. All measurements in this subsection were performed on CaV_2O_4 crystal #1. In contrast to a single peak above and a single peak below the zero-field peak frequency f_0 when an applied field is present, as expected for a collinear antiferromagnet, instead we see two peaks above f_0 and two peaks below f_0 in applied fields as shown by the vertical arrows in Fig. 5.5. Whether each set of two peaks is resolved depends on the angle of the applied field in the a-b plane as shown. We infer below that the spectra in Fig. 5.5 (and 5.6) are consistent with a magnetic structure at 4.2 K that consists of two antiferromagnetic substructures, each of which is a collinear antiferromagnetic arrangement where the angle between the ordering axes of the two substructures is $19(1)^\circ$. The angle labeled in each panel of Fig. 5.5 is the angle between the applied field and the axis $\boldsymbol{S}'_m$, which is the average of the projections onto the a-b plane of the two spin ordering directions (see Fig. 5.8 below). $\boldsymbol{S}'_m$ is approximately parallel to the b-axis and is determined by fitting the peak positions versus angle, as will be explained below.

In our discussions of the ^{51}V NMR results, we assume that the applied magnetic field only shifts the NMR frequency without affecting the electronic spins. In fact, the ordered electronic moments can be tilted by the applied field due to the presence of a torque. However, we can show that the tilting angle is indeed negligibly small. From the magnetization measurements,[6] at 4.2 K, the susceptibility χ of single crystal CaV_2O_4 with applied field in the a, b or c directions is $\chi \sim 0.003$ cm^3/mol, which corresponds to an induced moment of 0.005 μ_B for each vanadium spin in a 2 T field. The tilting angle required to produce such a moment is only

0.3°, assuming an ordered moment of 1.06 $\mu_{\rm B}$.[7] Both this angle and the induced moment are negligible to our studies.

The spectra in Fig. 5.5 exhibit a two-peak structure when the field points away from the $\boldsymbol{S}'_m$ axis. When measured by field sweep at a fixed frequency f, each peak i (= 1, 2) should appear at the field value

$$H_{\mathrm{peak}\,i} = \left| -f_0 \cos\alpha_i + \sqrt{f^2 - f_0^2 \sin^2\alpha_i} \right| / (\gamma_{\rm v}/2\pi), \tag{5.3}$$

where α_i is the angle between the field and the respective electronic spin ordering direction of a magnetic substructure noted above. The observed two-peak structures for $f > f_0$ and $f < f_0$ strongly indicate the presence of these two different antiferromagnetic spin ordering directions in the system. The ability to resolve the two peaks at the larger angles in Fig. 5.5 (and 5.6) is related to the larger partial derivative of $|\partial H_{\mathrm{peak}\,i}/\partial\alpha_i|$ of Eq. (5.3) at the larger α_i values for $\alpha_i < \pi/2$ rad.

The two peaks in the same spectrum have different heights, as can be clearly seen in Fig. 5.5 (b), (d), (g), and (i). The reason behind this difference is currently not understood. It may be due to the change of the nuclear spin-spin relaxation times at different field values, since we fix the separation between the two rf pulses for echo generation to be 16 μs. We note that the difference cannot be attributed to the different percentage of spins in the two spin substructures. In such a scenario, the spins contributing to the left peaks in Figs. 5.5(b) and (g) should contribute to the right peaks in Figs. 5.5(d) and (i) (see Fig. 5.9), and the left peaks should be higher in one orientation while lower in the other in Figs. 5.5(b) and (d), and in Figs. 5.5(g) and (i), respectively. However, the spectra in Figs. 5.5(b) and (d), and in Figs. 5.5(g) and (i) are almost the same. The symmetry in the spectra with the field on opposite sides of $\boldsymbol{S}'_m$, such as in Figs. 5.5(b) and (d) and in Figs. 5.5(g) and (i), indicates that the number of spins in the two substructures are the same.

Since the above two-peak structure is observed with the field in the *a*-*b* plane, these measurements can only detect the difference of the spin projections of the two substructures onto the *a*-*b* plane. In order to determine whether or not the projections onto the *b*-*c* plane are also different, we also measured the spectra with the field in the *b*-*c* plane. Some representative

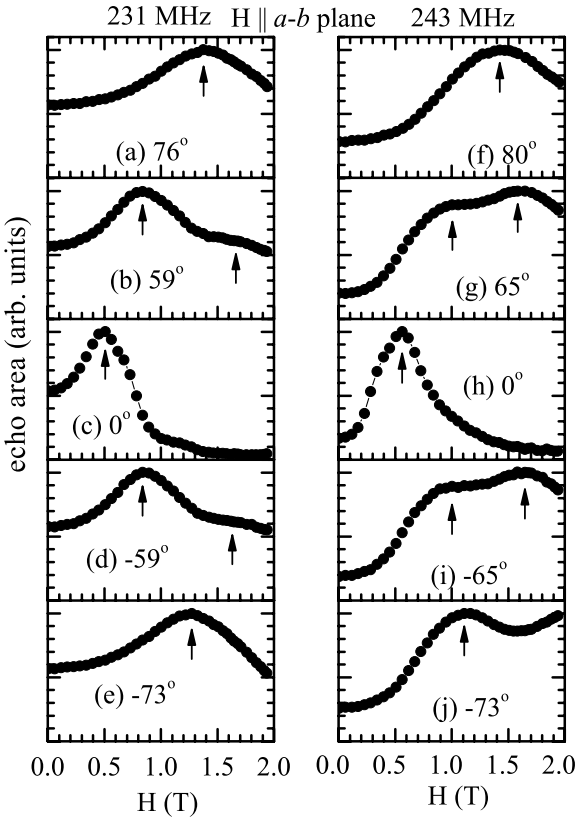

Figure 5.5 Field swept spectra with the applied magnetic field parallel to the a-b plane at rf frequencies of 231 MHz (left panels) and 243 MHz (right panels). The angles between the field and the average of the two projections of the two spin directions onto the a-b plane ($\boldsymbol{S}'_m$ in Fig. 5.8) are labeled in each panel. The arrows indicate the positions of the peaks. $\boldsymbol{S}'_m$ is approximately parallel to the crystallographic b-axis. The spectra were measured at 4.2 K on crystal #1.

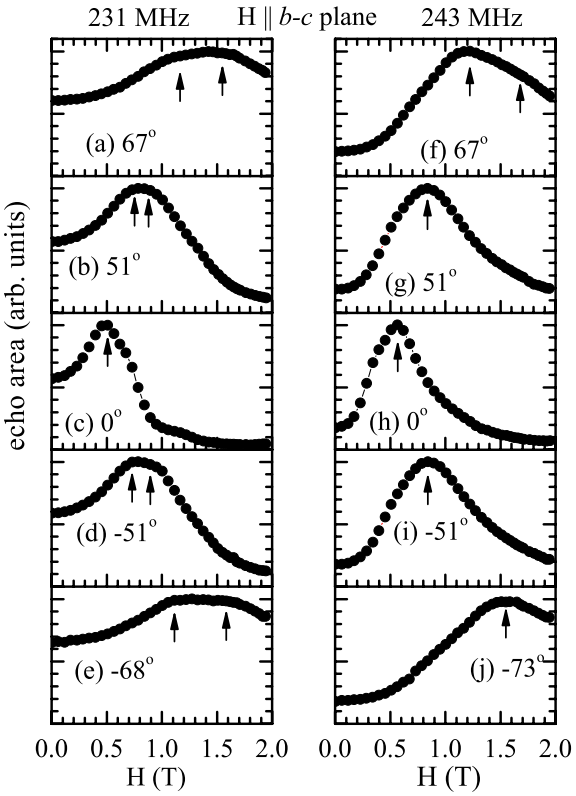

Figure 5.6 Field swept spectra with the applied magnetic field parallel to the b-c plane at rf frequencies of 231 MHz (left panels) and 243 MHz (right panels). The angles between the field and the average of the two projections of the two spin directions onto the b-c plane ($\boldsymbol{S}''_m$ in Fig. 5.8) are labeled in each panel. The arrows indicate the positions of the peaks. The spectra were measured at 4.2 K on crystal #1.

spectra with the field in different directions are displayed in Fig. 5.6, where the angles listed are described in the caption. As one can see, a two peak structure is still observed when the field is at a large angle from the $\boldsymbol{S}''_m$ axis. However, the separations between the two peaks are smaller than in Fig. 5.5, indicating a smaller angle between the two easy axis projections onto the b-c plane than onto the a-b plane.

In order to study whether there exists canting and/or an imbalance in the number of spins in opposite directions for each of the two ordered magnetic substructures, we compared the spectra with those measured with the field rotated by 180°. Figure 5.7 displays two spectra measured at $f = 222$ MHz with the field parallel to the a-b plane and $-31°$ and 149° away

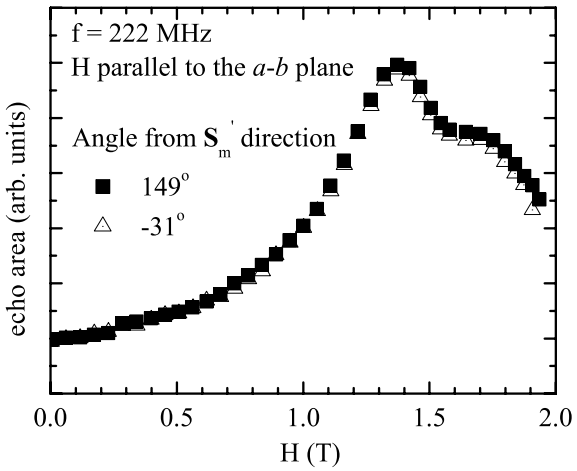

Figure 5.7 Comparison of two spectra measured at rf frequency $f = 222$ MHz with and without the field direction reversed. The fields are parallel to the a-b plane and form angles of $-31°$ and $149°$ from the $\boldsymbol{S}'_m$ direction, respectively. The spectra were measured at 4.2 K on crystal #1.

from the $\boldsymbol{S}'_m$ direction, respectively. These two spectra are identical within experimental error, indicating the absence of spin canting and the same number of spins in opposite directions within each magnetic substructure.

Thus we propose a model of the spin structure as shown in Fig. 5.8. Various notations used in the model are explained in the caption of Fig. 5.8. There are equal numbers of spins in the two antiferromagnetic substructures, each of which consists of collinear antiparallel spins also with equal number. The plane defined by the two ordering directions is parallel neither to the a-b nor the b-c plane. The average ordered moment direction $\boldsymbol{S}_m$ is approximately parallel to the b-axis. This is consistent with single crystal anisotropic magnetization measurements versus temperature which showed that below $T_{\rm N}$, the average easy axis of the magnetic structure is approximately the b-axis.[6] Note that in our NMR study, we cannot determine the location in the lattice of the two different magnetic substructures.

To extract the angle between the spin ordering directions of the two substructures, we measured the dependence of the peak positions versus the field directions at rf frequencies of 231 and 243 MHz. The results are shown in Fig. 5.9. For small angles between $\boldsymbol{H}$ and $\boldsymbol{S}'_m$ or $\boldsymbol{S}''_m$, only one peak is observed. At larger angles, the positions of two peaks can be resolved.

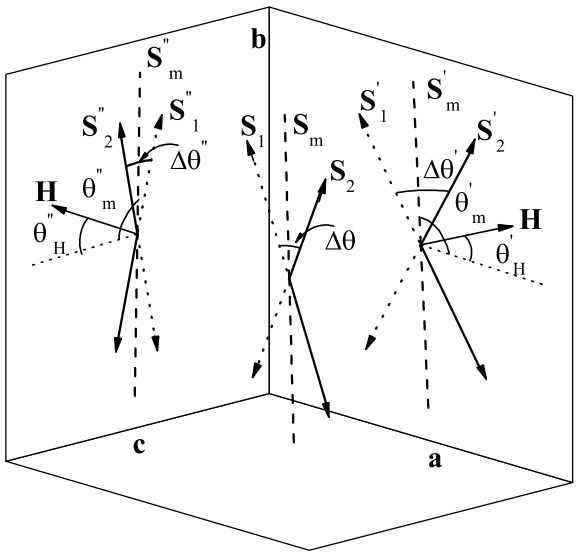

Figure 5.8 The proposed ordered spin structure in CaV_2O_4. There are two different antiferromagnetic ordering substructures with equal numbers of spins, each of which has a collinear antiferromagnetic spin arrangement. $\Delta\theta$, $\Delta\theta'$, and $\Delta\theta''$ are the angles between these two directions, and their projections on a-b and b-c planes, respectively. $\boldsymbol{S}_m$, $\boldsymbol{S}'_m$, and $\boldsymbol{S}''_m$ are the average of the two directions and their projections on a-b and b-c planes, respectively. θ'_H (θ''_H) and θ'_m (θ''_m) are the angles formed between a fixed arbitrary experimental reference direction in the a-b (b-c) plane and the applied field $\boldsymbol{H}$ and $\boldsymbol{S}'_m$ ($\boldsymbol{S}''_m$), respectively.

Two different symbols are used to represent the two different spin substructures, while for spectra with single peaks, a third symbol is used. Since the angle between the spin direction and the b-axis is much less than one radian, $\cos\alpha_i$ in Eq. (5.3) for the field in the a-b plane can be approximated by

$$\cos\alpha_{1,2} \approx \cos(\theta'_m \pm \Delta\theta'/2 - \theta'_H), \tag{5.4}$$

where $\alpha_{1,2}$ are the angles between the field and the two spin directions $\boldsymbol{S}_1$ and $\boldsymbol{S}_2$, respectively. Similarly, for the field in the b-c plane, one has

$$\cos\alpha_{1,2} \approx \cos(\theta''_m \pm \Delta\theta''/2 - \theta''_H). \tag{5.5}$$

We fitted Eq. (5.3) with $\cos\alpha_{1,2}$ given by Eqs. (5.4) and (5.5) to the data in Fig. 5.9. The free parameters in the fit were f_0, θ'_s, θ''_s, $\Delta\theta'$, and $\Delta\theta''$. The best fit results are $f_0 = 236.7(2)$ MHz, $\Delta\theta' = 18(1)^\circ$, and $\Delta\theta'' = 6(1)^\circ$. The fits are shown in Fig. 5.9. Since the angles between the spins and the b-axis are much less than one radian, we have

$$\sin\Delta\theta \approx \sqrt{\sin^2\Delta\theta' + \sin^2\Delta\theta''}, \tag{5.6}$$

from which one obtains the angle between the easy axes of the two magnetic substructures to be $\Delta\theta = 19(1)^\circ$.

In addition to the study of the angular dependence of the peak positions, we also measured their frequency dependences to further confirm the proposed spin structure. Figures 5.10(a) and (b) show the field swept spectra with the field $\boldsymbol{H}$ pointing along the $\boldsymbol{S}''_m$ direction, at rf frequencies lower and higher than $f_0 = 236.7$ MHz, respectively. Note that when $\boldsymbol{H} \parallel \boldsymbol{S}''_m$, the two magnetic substructures have the same peak positions of the spectra (see the zero-angle data in Fig. 5.9). The peaks in Figs. 5.10(a) and (b) both shift to higher fields when the frequency shifts further away from f_0, respectively. The peak positions $H_{\rm peak}$ versus rf frequency are plotted in Fig. 5.10(c). The two sets of data points can be well fitted by the two linear equations

$$f = f_0 \pm H_{\rm peak}\gamma/2\pi, \tag{5.7}$$

where f_0 is the peak frequency of the spectrum at zero applied field. A fit of Eq. (5.7) to the data gives $\gamma/2\pi = 11.4(2)$ MHz/T, and $f_0 = 236.7(1)$ MHz. Assuming $\boldsymbol{S}_m$ to be parallel to the

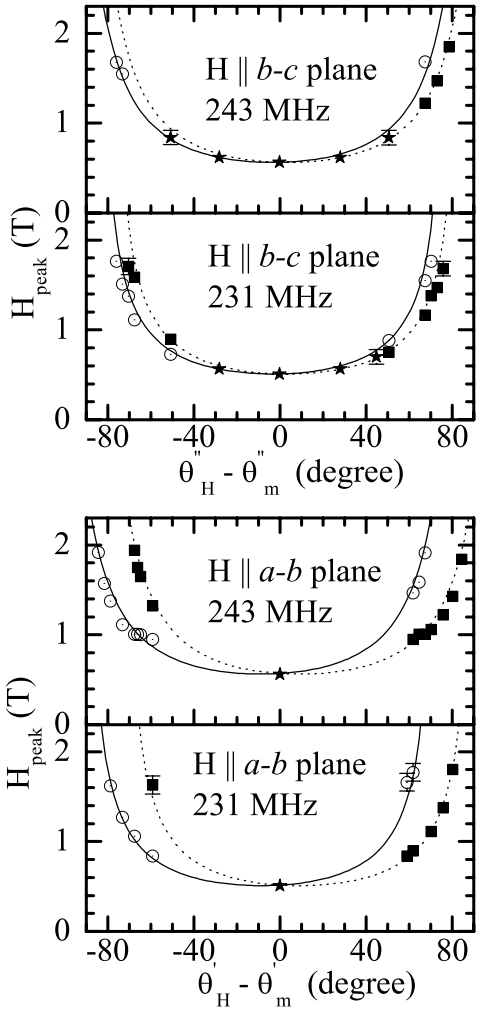

Figure 5.9 Dependence of the peaks in the spectra at 4.2 K on the direction of the applied magnetic field, with the field in the b-c (top two panels) and a-b (bottom two panels) planes of crystal #1, where the rf frequencies are equal to 231 and 243 MHz, respectively. For definitions of the angles θ'_H, θ'_m, θ''_H, and θ''_m, see Fig. 5.8. Circles and filled squares correspond to the two different spin ordering directions of the two magnetic substructures, respectively. The symbol $\star$ is used when the two peaks from the two spin directions overlap and only a single peak can be observed. The error in $H_{\rm peak}$ is comparable to the size of the symbols unless shown explicitly. The solid and dotted lines represent the fits by the theoretical prediction in Eq. (5.3).

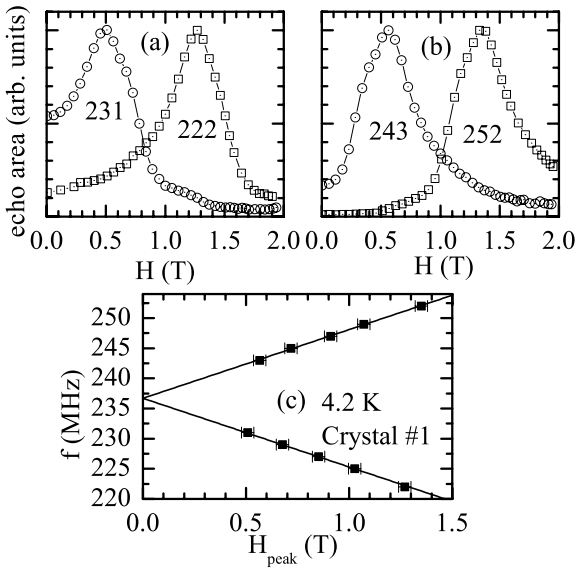

Figure 5.10 (a) and (b): Field-swept ^{51}V NMR spectra at four different frequencies at 4.2 K. The frequencies are given under each spectrum in units of MHz. The field is applied parallel to the $\boldsymbol{S}''_m$ direction. (c): The frequency versus the peak field of the spectra. The solid lines are linear fits by Eq. (5.7). The measurements were done on crystal #1 at 4.2 K.

b-axis, the value of γ should be $\gamma/2\pi = (\gamma_{\rm v}/2\pi)\cos(\Delta\theta/2) = 11.07$ MHz/T, where $\Delta\theta = 19^\circ$ is the above angle between the ordering directions of the two magnetic substructures. This value of $\gamma/2\pi$ is very close to the above fitting result.

5.4.2 Ordered Moment and Its Temperature Dependence

In this subsection, we will study the temperature dependence of the vanadium ordered moment, which provides evidence for an energy gap in the antiferromagnetic spin wave excitation spectrum, arising from anisotropy effects. Then we will discuss the value of the saturation vanadium spin moment at low temperatures. Measurements in this subsection were performed on crystal #2. The experiment was set up to allow field rotation in the a-b plane. By rotating the field in the a-b plane, the $\boldsymbol{S}'_m$ direction (see Fig. 5.8) is identified as the direction along which the peak position in the spectrum is at a minimum applied field at a fixed rf frequency away from f_0 (see Fig. 5.9). After identifying the $\boldsymbol{S}'_m$ direction, all subsequent measurements of the spectra were performed versus H at fixed rf frequencies with the field along the $\boldsymbol{S}'_m$

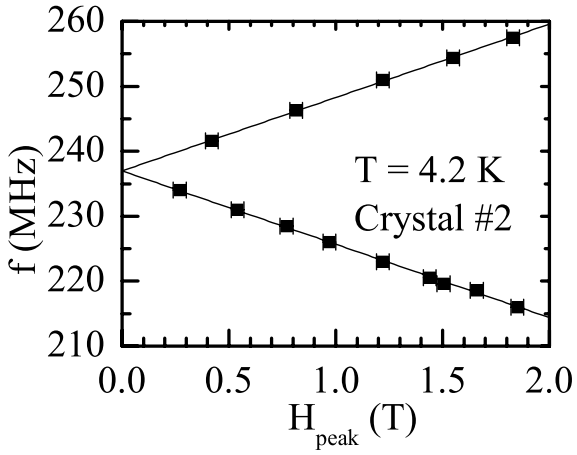

Figure 5.11 rf frequency f versus peak $H_{\rm peak}$ in field swept spectrum in crystal #2 at 4.2 K. The field is applied along the S'_m direction. The solid lines are fits with Eq. (5.7).

direction.

With the field along $\boldsymbol{S}'_m$, only a single peak is observed in the spectrum at each frequency (see Fig. 5.10). In Fig. 5.11, we display the frequency dependence of the peak position at 4.2 K. Similar to the case of crystal #1 (Fig. 5.10), the data points can be well fitted by two straight lines. A fit of Eq. (5.7) to the data gives $f_0 = 236.98(8)$ MHz and $\gamma/2\pi = 11.3(1)$ MHz/T. This value of γ is in agreement with the fitting value in crystal #1. However, the value of f_0 is slightly larger than in crystal #1. This slight difference may be due to sample-dependent differences.

Figure 5.12 displays representative spectra measured at four different temperatures. For comparison between the different spectra, the x-axis has been converted to the quantity $f + H\gamma/2\pi$, with $\gamma/2\pi = 11.3$ MHz/T. As the temperature increases, the signal intensity decreases rapidly and the spectra can only be measured below 45 K. In order to more accurately determine the peak position of the spectra, we fitted the original field swept spectra (with the x-axis being H) by a Gaussian function

$$I(H) = A + B\exp[-2(H - H_{\rm peak})^2/\sigma^2], \tag{5.8}$$

with A, B, $H_{\rm peak}$, and σ as fitting parameters. The zero field peak frequency f_0 is then

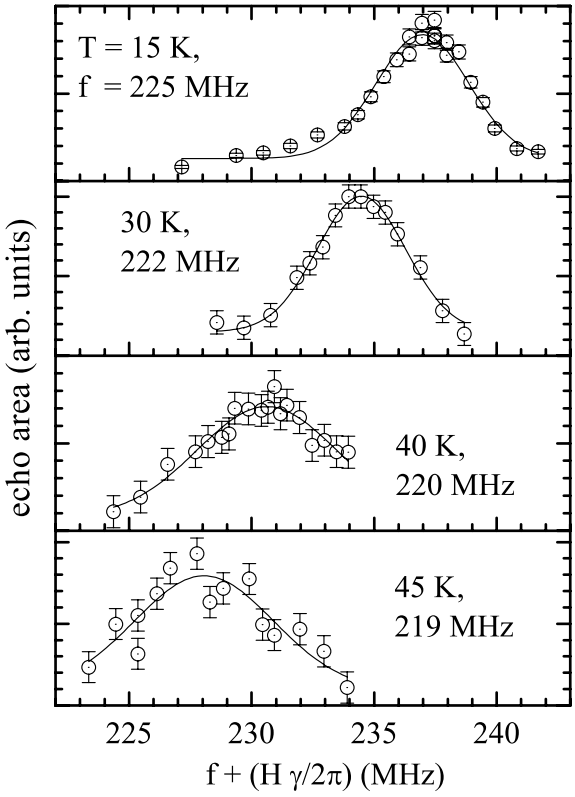

Figure 5.12 Field swept spectra at different temperatures on crystal #2. The temperature and the rf frequency for each measurement are labeled in each panel. The solid lines are fits by Eq. (5.8) to extract the peak positions.

determined from

$$f_0 = f \pm H_{\rm peak}\gamma/2\pi,$$

where $\gamma/2\pi = 11.3$ MHz/T and the $+$ and $-$ signs correspond to the cases of $f < f_0$ and $f > f_0$, respectively. In order to determine whether $f < f_0$ or $f > f_0$, spectra were measured with at least two different frequencies at each temperature. With the correct choices of the $+$ or $-$ signs, the obtained f_0 values for different spectra as in Fig. 5.12 are the same within experimental error at each temperature. The final f_0 value is an average over all calculated f_0 values for various spectra at the same given temperature.

Figure 5.13 shows the temperature dependence of f_0. Since the temperature dependence of the hyperfine coupling constant can be ignored,[13] $f_0(T)$ is directly proportional to the ordered local moment. The ordered moment is almost temperature independent at $T < 15$ K.

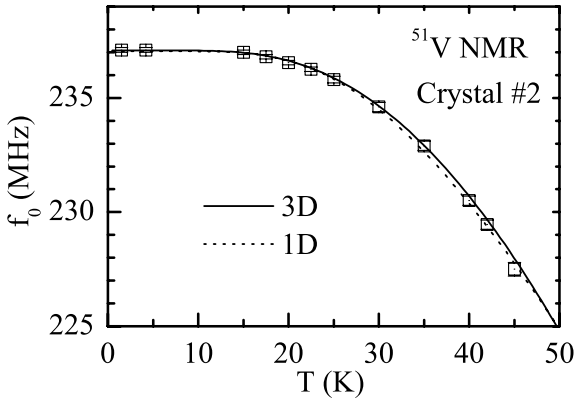

Figure 5.13 Temperature dependence of the ^{51}V NMR spectra peak position in zero applied field in CaV_2O_4 crystal #2. The dotted and solid curves are fits by Eqs. (5.19) with one-dimensional spin wave dispersion and (5.20) with three-dimensional dispersion, respectively.

In the spin wave theory of a three-dimensional antiferromagnet *without anisotropy*, the initial decrease of the ordered moment with temperature T should follow a T^2 dependence.[14] Fitting the data by a power law gives an exponent ≥ 3.5, an unphysically large value (not shown). The temperature independence below $T < 15$ K thus indicates the presence of an anisotropy-induced energy gap for spin wave excitations.[15]

Before estimating the gap energy, we will first estimate the value of the saturation moment at $T = 0$ K. The local moments reach their saturation value at $T < 15$ K. From the value of $f_0 = 237$ MHz at $T < 15$ K, one obtains a local field value of $H_{\rm loc} = f_0/(\gamma_{\rm v}/2\pi) = 21.2$ T. In order to infer the value of local moment from the local field value, the hyperfine coupling constant A and the g-factor have to be determined. With known values of A and g, the ordered moment $\langle\mu_z\rangle$ is $|\langle\mu_z\rangle| = g\mu_{\rm B}H_{\rm loc}/A$. The local field is dominated by the contact interaction through the polarized core electrons, which is approximately proportional to the number of unpaired electronic spins in the $3d$ orbitals with a proportionality constant of 12.5 T per unpaired electron to within 20%.[8] However, beside the contact interaction, orbital effects[9] and transfered hyperfine coupling with the neighboring V^{3+} ions[16] may also contribute significantly to the local field at the ^{51}V nuclear site.

In the absence of a knowledge of the orbital effects and transfered interactions, we will

estimate a possible range of the $A/(g\mu_B)$ value in CaV_2O_4 using the known values of $A/(g\mu_B)$ in other V^{3+} compounds. The values of $A/(g\mu_B)$ in $LaVO_3$, YVO_3, and V_2O_3 are 16.8, 20.8, and 15.5 T/μ_B, respectively.[17] For V^{3+} in Al_2O_3, EPR measurements gave $A/(g\mu_B) =$ 13.3 T/μ_B.[18] The range of $A/(g\mu_B)$ in the above four compounds is between 13.3 and 20.8 T/μ_B. Assuming $A/(g\mu_B)$ in CaV_2O_4 lies in the same range, the low temperature ordered vanadium moment in CaV_2O_4 is thus in the range of 1.02–1.59 μ_B. This $|\langle\mu_z\rangle|$ range is consistent with the value 1.06(6) μ_B extracted from the previous neutron powder diffraction study.[7]

Next we estimate the energy gap for the spin wave excitations. From the neutron diffraction studies,[7] we know that the spins reverse their ordering direction upon moving along the c-axis. Therefore the spin structure in the ordered state within a zig-zag chain should look as in Fig. 5.14, where we ignore the possible small misalignment of 19° between spins in the two magnetic substructures discussed above. Because each spin in one leg of the chain couples by the same exchange constant J_1 to two spins in the other leg that are ordered in opposite directions, we expect that the effective coupling between the two legs within a zig-zag chain is greatly reduced in the ordered state. As a result, we will consider the nearest-neighbor interactions within the leg J_2 as the only dominant magnetic interaction and treat the effect of interleg interaction within a zig-zag chain as a weak interchain interaction. For simplicity, we will use a single exchange constant J' to characterize the effect of the interchain interactions. To include the effect of anisotropy, we assume a single ion anisotropy in the system with a single direction of easy axis. Then, the Hamiltonian can be written as

$$H = \sum_i \left(2J_2 \boldsymbol{S}_i \cdot \boldsymbol{S}_{i+1} - \frac{1}{2} K S_{iz}^2 \right) + 2 \sum_{\langle i,j \rangle} J' \boldsymbol{S}_i \cdot \boldsymbol{S}_{j+1}, \tag{5.9}$$

where K is the anisotropy constant, the index i runs through the spins in one leg of the chain, and the summation $\langle i, j \rangle$ runs through all interleg and interchain nearest-neighbor pairs.

The Fourier transform of the exchange interactions is

$$\mathcal{J}(q) = \sum_j J(\boldsymbol{r}_{ij}) \exp(-iq \cdot \boldsymbol{r}_{ij}),$$

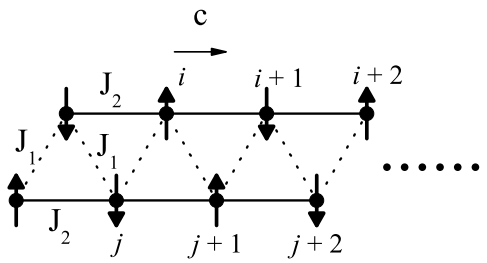

Figure 5.14 Zig-zag spin structure in CaV_2O_4. Due to the alternation of the spin directions along the c-aixs, the interaction between the spins in the two legs of the zig-zag chain are essentially decoupled. The possible misalignment of 19° between spins in the two legs of the zig-zag chain is ignored. J_1 and J_2 are the nearest-neighbor interleg and intraleg exchange interactions, respectively.

where $\boldsymbol{r}_{ij}$ connects two spins in opposite sublattices, $J(\boldsymbol{r}_{ij}) > 0$ is the nearest-neighbor exchange constant, and the index j runs through all the nearest-neighbor spins of spin i in the opposite sublattice (each sublattice consists of spins in the same direction). The spin wave dispersion relation is given by[19]

$$E_q = \left\{[2S\mathcal{J}(0) + KS]^2 - [2S\mathcal{J}(q)]^2\right\}^{1/2}, \tag{5.10}$$

where we ignored interactions between spins in the same sublattice. The spin wave gap value is given by the value of E_q at $q = 0$. In the limit of small anisotropy $K \ll 2\mathcal{J}(0) \approx 4J_2$, the gap energy is given by

$$E_G = 2S[\mathcal{J}(0)K]^{1/2} \approx 2^{3/2}S[J_2K]^{1/2}. \tag{5.11}$$

In the spin wave theory, the decrease of sublattice magnetization is due to the thermal activation of spin wave excitations. In the above bipartite antiferromagnetic system,[19]

$$\langle S_z(0)\rangle - \langle S_z(T)\rangle = \frac{V}{(2\pi)^3}\int \langle n_q\rangle \frac{2\mathcal{J}(0)S + KS}{E_q} d^3q, \tag{5.12}$$

where the integral is limited to the first Brillouin zone of one sublattice, V is the sample volume per sublattice site, and

$$\langle n_q\rangle = \frac{1}{e^{E_q/k_{\mathrm{B}}T} - 1}$$

is the number of thermally excited antiferromagnetic magnons.

The dispersion relation in Eq. (5.10) depends on the spin lattice structure and the exchange interactions $J(\boldsymbol{r})$. For a quasi one-dimensional chain with interchain coupling J', at temperatures $T \gg J'/k_{\rm B}$, one can ignore the dispersion perpendicular to the chain direction. Then for small values of q_c, which is the $\boldsymbol{q}$ vector component along the chain, one can perform a Taylor series expansion of $|\mathcal{J}(q)|^2$ as

$$|\mathcal{J}(q)|^2 \approx |\mathcal{J}(0)|^2 \left[1 - l^2 q_c^2\right], \tag{5.13}$$

where l is the nearest-neighbor distance within the leg.

At $T \ll J_2/k_{\rm B}$, only spin waves at small q_c values have significant contributions to the integral in Eq. (5.12), so one can change the limits of integral for q_c in Eq. (5.12) to $\pm\infty$. The small q approximation is valid only at temperatures where $1 - |\langle S_z(T)\rangle|/|\langle S_z(0)\rangle| < 0.1$,[15] which is satisfied within our experimental temperature range. Substituting Eq. (5.13) into Eq. (5.10), and changing the limits of integral for q_c in Eq. (5.12) to $\pm\infty$, one obtains in the limit of small anisotropy $K \ll 2\mathcal{J}(0)$ and $T \ll E_G$

$$1 - \frac{\langle S_z(T)\rangle}{\langle S_z(0)\rangle} \approx B e^{-E_G/k_{\rm B}T} (E_G/k_{\rm B}T)^{-1/2}, \tag{5.14}$$

where

$$B \approx \frac{2}{\sqrt{2\pi}} \approx 0.80. \tag{5.15}$$

Equation (5.14) is valid at temperatures $J'/k_{\rm B} \ll T \ll J_2/k_{\rm B}$. In CaV_2O_4, $J'/k_{\rm B}$ might fall within the experimental temperature range in Fig. 5.13 ($1.5 \leq T \leq 45$ K). Therefore, it is useful to consider the other limit of $T \ll J'/k_{\rm B} \ll J_2/k_{\rm B}$, where a three dimensional dispersion is more appropriate. Applying a small q approximation, one obtains

$$|\mathcal{J}(q)|^2 \approx |\mathcal{J}(0)|^2 \left\{1 - \eta^2 (V/2)^{2/3} \left[q_c^2 + j'(q_a^2 + q_b^2)\right]\right\}, \tag{5.16}$$

where for simplicity, we assumed an isotropic dispersion in the a-b plane, η is a geometrical factor of order one which depends on the spin structure,[20] and j' is of the order of J'/J_2. By combining Eqs. (5.10), (5.12), and (5.16), and changing the three limits of integrations to $\pm\infty$ in Eq. (5.12), then instead of Eq. (5.14), we have in the limit of small anisotropy $K \ll 2\mathcal{J}(0)$

and $T \ll E_G$[15]

$$1 - \frac{\langle S_z(T)\rangle}{\langle S_z(0)\rangle} \approx Be^{-E_G/k_{\rm B}T}(E_G/k_{\rm B}T)^{-3/2}, \tag{5.17}$$

where

$$B \approx \frac{\sqrt{2}\alpha}{\pi^{\frac{3}{2}}\eta^3 j'} \tag{5.18}$$

with $\alpha \equiv K/[2\mathcal{J}(0)]$.

Using Eqs. (5.14) and (5.17) and the relation

$$f_0(T)/f_0(0) = |\langle S_z(T)\rangle|/|\langle S_z(0)\rangle|,$$

one obtains the variation of the zero-field ^{51}V NMR resonance frequency f_0 as (for 1D)

$$f_0(T) = f_0(0)\left[1 - Be^{-E_G/k_{\rm B}T}(E_G/k_{\rm B}T)^{-1/2}\right] \tag{5.19}$$

or (for 3D)

$$f_0(T) = f_0(0)\left[1 - Be^{-E_G/k_{\rm B}T}(E_G/k_{\rm B}T)^{-3/2}\right], \tag{5.20}$$

depending on whether a one-dimensional (1D) or three-dimensional (3D) dispersion is used for E_q. We fitted Eqs. (5.19) and (5.20) to the $f_0(T)$ versus T data in Fig. 5.13 at $T \leq 45$ K with $f_0(0)$, B, and E_G as free parameters. The best fit results are $f_0(0) = 237.04(5)$ MHz, $E_G = 98(5)$ K, $B = 0.51(7)$ for the 1D dispersion with Eq. (5.19), and $f_0(0) = 237.08(6)$ MHz, $E_G = 64(5)$ K, and $B = 0.27(6)$ for the 3D dispersion with Eq. (5.20). The best fit curves are shown as the dotted and solid curves in Fig. 5.13, respectively. Since Eqs. (5.19) and (5.20) are derived under the two limiting conditions of $T \gg J'/k_{\rm B}$ and $T \ll J'/k_{\rm B}$, respectively, one can expect that the actual E_G value might lie somewhere between 64 and 98 K. Given a value of E_G, we can make a rough estimate of the anisotropy constant K. From the magnetization study, one estimates that the intrachain nearest-neighbor exchange constant to be of the order of $J_2/k_{\rm B} \sim 200$ K.[6] Taking $S = 1$, $E_G = 81$ K, and $\mathcal{J}(0) \approx 2J_2$, we thus have from Eq. (5.11) that $K/k_{\rm B} \sim 4$ K.

The above fitting value of $B = 0.51(7)$ from 1D dispersion is similar to the calculated value of 0.80. The fitting value of $B = 0.27(6)$ from the 3D dispersion constrains the value of J' in the 3D model. Taking $\alpha \approx K/4J_2 \sim 0.01$, $\eta \sim 1$, and $B = 0.27$, then from Eq. (5.18)

one has $j' \sim 0.01$ and $J'/k_{\rm B} \sim j'J_2/k_{\rm B} \sim 2$ K. However, this value of J' seems inconsistent with the initial assumption of $T \ll J'/k_{\rm B}$ required for the three-dimensional model to be valid. Therefore, Eq. (5.19) of the 1D model might provide a better approximation to the $f_0(T)$ data.

5.5 Summary and Conclusions

We have presented ^{17}O and ^{51}V NMR results on the zig-zag spin chain compound CaV_2O_4. The strong inhomogeneous broadening and a peak in the nuclear spin-lattice relaxation rate versus temperature of ^{17}O NMR confirm the presence of an antiferromagnetic phase transition at 78 K in a powder sample. The crystals we studied have $T_{\rm N} = 69$ K. ^{51}V NMR in the ordered state of crystals reveals the presence of two antiferromagnetic substructures at 4.2 K, each of which is collinear and which form an angle of 19(1)° between them with the average direction approximately parallel to the b-axis. The location in the lattice of the different spin substructures is unknown. However, we speculate that the two magnetic substructures are associated with the two inequivalent V^{3+} $S = 1$ zig-zag spin chains in the orthorhombic crystal structure, respectively. The temperature dependence of the zero-field resonance frequency at low temperatures suggests the presence of an energy gap in the spin wave excitation spectrum. The energy gap is estimated from spin wave theory to be between 64 and 98 K.

Acknowledgements

We acknowledge F. Borsa, B. Lake, and A. Kreyssig for useful discussions. Work at the Ames Laboratory was supported by the Department of Energy-Basic Energy Sciences under Contract No. DE-AC02-07CH11358.

References

[1] H. T. Diep, *Frustrated Spin Systems* (World Scientific, Hackensack, New Jersey, 2004).

[2] T. Hikihara, M. Kaburagi, H. Kawamura, and T. Tonegawa, J. Phys. Soc. Jpn. **69**, 259 (2000).

[3] A. Kolezhuk, R. Roth, and U. Schollwöck, Phys. Rev. Lett. **77**, 5142 (1996).

[4] H. Kikuchi, M. Chiba, and T. Kubo, Can. J. Phys. **79**, 1551 (2001).

[5] H. Fukushima, H. Kikuchi, M. Chiba, Y. Fujii, Y. Yamamoto, and H. Hori, Prog. Theor. Phys. Supp. **145**, 72 (2002).

[6] A. Niazi, S. Bud'ko, A. Honecker, J. Q. Yan, D. L. Schlagel, T. A. Lograsso, and D. C. Johnston, (unpublished); A. Niazi, D. C. Johnston, S. Bud'ko, D. L. Schlagel, T. A. Lograsso, and A. Honecker, Bull. Am. Phys. Soc. **51**, 192 (2006), Abstract B23.6.

[7] J. M. Hastings, L. M. Corliss, W. Kunnmann, and S. La Placa, J. Phys. Chem. Solids **28**, 1089 (1967).

[8] G. C. Carter, L. H. Bennett, and D. J. Kahan, *Metallic Shifts in NMR*, Progress in Materials Science Vol. 20 (Pergamon Press, New York, 1977).

[9] A. J. Freeman and R. E. Watson, in *Magnetism*, edited by G. T. Rado and H. Suhl (Academic Press, New York, 1963).

[10] Crystals were grown in the Materials Preparation Center, Ames Laboratory-USDOE, Ames, IA, USA. See <www.mpc.ameslab.gov>.

[11] D. C. Johnston, Phys. Rev. B **74**, 184430 (2006).

[12] F. Borsa and A. Rigamonti, in *Magnetic Resonance of Phase Transitions*, edited by F. J. Owens, C. P. Poole, and H. A. Farach (Academic Press, New York, 1979).

[13] E. A. Turov and M. P. Petrov, *Nuclear Magnetic Resonance in Ferro- and Antiferromagnets* (Halsted Press, New York, 1972).

[14] R. Kubo, Phys. Rev. **87**, 568 (1952).

[15] V. Jaccarino, in *Magnetism*, edited by G. T. Rado and H. Suhl (Academic Press, New York, 1979), vol. IIA, p. 322.

[16] J. Kikuchi, H. Yasuoka, Y. Kokubo, Y. Ueda, and T. Ohtani, J. Phys. Soc. Jpn. **65**, 2655 (1996).

[17] J. Kikuchi, H. Yasuoka, Y. Kokubo, and Y. Ueda, J. Phys. Soc. Jpn. **63**, 3577 (1994).

[18] G. M. Zverev and A. M. Prokhorov, Soviet Phys. JETP **11**, 330 (1960).

[19] S. W. Lovesey, *Theory of Neutron Scattering from Condensed Matter*, vol. 2 (Clarendon Press, Oxford, 1984).

[20] T. Moriya, Prog. Theor. Phys. **16**, 23 (1956).

CHAPTER 6. Structure, Magnetization, and NMR of the Spin Glass Compound $(Li_xV_{1-x})_3BO_5$ (x ≈ 0.40 and 0.33)

(This chapter is based on a paper published in Phys. Rev. B by X. Zong, A. Niazi, F. Borsa, X. Ma, and D. C. Johnston[1])

Abstract

Structural and magnetic properties of $(Li_xV_{1-x})_3BO_5$ powders ($x = 0.33$) and single crystals ($x = 0.40$) were studied by x-ray diffraction, magnetization and NMR measurements. Both powder and single crystal x-ray diffraction data are consistent with the previously reported structure of the system. Magnetization measurements show an overall antiferromagnetic interaction among vanadium spins and reveal a transition into a spin glass state at a sample and magnetic field dependent temperature below ~ 10 K. The high temperature ($T > 20$ K) susceptibility is analyzed using a linear spin trimer model suggested in the literature but such a model is found to be insufficient to explain the data. ^{7}Li and ^{11}B NMR studies indicate an inhomogeneous dynamics close to the zero field spin glass transition temperature. The distribution of electronic spin relaxation times is derived using a recently proposed method and the broad temperature-dependent distribution obtained gives a consistent description of the NMR results. The temperature dependence of the distribution indicates a strong slowing down of the local moment spin dynamics as the system cools toward the zero field spin glass transition temperature even in the presence of a strong applied magnetic field up to 4.7 T.

6.1 Introduction

Spin glasses have attracted continuous research interest for more than 30 years. However, some fundamental questions remain controversial. For example, recent debate focuses on whether an isotropic three-dimensional Edward-Anderson Heisenberg spin glass has a finite transition temperature.[2–7] Another important question concerns whether a spin glass transition can occur in a finite magnetic field. An answer to this second question would allow one to distinguish between two main scenarios concerning the nature of the spin glass phase: the "droplet"[8] and "replica symmetry breaking"[9] scenarios. Magnetization measurements on the Ising spin glass $Fe_xMn_{1-x}TiO_3$ indicated that the spin glass state is destroyed by a nonzero magnetic field and lend support to the droplet picture.[10–12] On the other hand, the persistence of a frozen spin glassy phase in an applied magnetic field in different Heisenberg systems that show spin glass transitions in zero field was inferred through magnetization and torque measurements.[13–16]

The origin of the nonexponential spin autocorrelation functions[17–20] in spin glasses is also an issue of continuous debate. It was often assumed that the nonexponential correlation function arises from the sum of a distribution of single exponential correlation functions of different magnetic entities in the system. Under such an assumption, a distribution of relaxation times could be derived from muon spin depolarization, magnetization and neutron spin echo experiments.[17, 21–23] Such a viewpoint was supported by numerical simulations, which showed that the spin autocorrelation functions are spatially inhomogeneous close to the spin glass transition temperature.[24–27] Another viewpoint claims that the nonexponential spin autocorrelation function is an intrinsic, homogeneous feature of spin glasses.[18, 28] One argument to support such a view is that the different relaxation times are associated with different excitation modes in the system that overlap in space. Since a spin can take part in different modes simultaneously, the relaxation for each spin is nonexponential.[28] An additional homogeneous relaxation mechanism is hierarchical relaxation where the relaxation pathway at a specific time depends on relaxation occurring in previous pathways.[29]

$(Li_xV_{1-x})_3BO_5$ is a Heisenberg spin glass system first synthesized and studied by Onoda.[30]

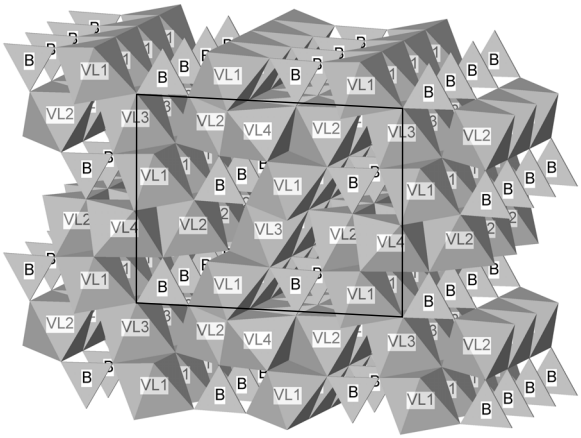

Figure 6.1 The crystal structure of $(Li_xV_{1-x})_3BO_5$. B represents boron sites and VL1–VL4 are the 4 sites occupied by vanadium or lithium atoms. Oxygen atoms occupy the vertices of the triangles and octahedra. The rectangle indicates the size of a unit cell in the plane of the page. The crystallographic a, b axes are along the vertical and horizontal directions in the plane of the page, respectively. The c-axis is perpendicular to the page.

It has an orthorhombic crystal structure (space group *Pbam*) as shown in Fig. 6.1, where Li or V statistically occupy to varying extents four inequivalent sites VL1–VL4 that are octahedrally coordinated by oxygen atoms. Transport studies in the temperature region between 80 and 300 K showed insulating behavior. The high temperature magnetic susceptibility χ followed the Curie-Weiss law with a negative Weiss temperature, indicating an overall antiferromagnetic interaction among vanadium magnetic moments. The magnetization M deviates from being proportional to the applied magnetic field H at temperatures $T < 25$ K and a transition to a spin glass state at lower T was suggested.[30] The inverse magnetic susceptibility $\chi^{-1}(T)$ data showed negative curvature below ~ 100 K [see also Fig. 6.3(a) below], which was attributed by Onoda to the occurrence of antiferromagnetic clusters or spin trimers.[30] However, additional experimental studies are necessary to further characterize the magnetic state of the system at low temperatures.

In this chapter we report further structure, magnetization and NMR studies of this new compound $(Li_xV_{1-x})_3BO_5$. The crystal structure in Ref. [30] is confirmed by x-ray diffraction studies on powder and single crystal samples. In particular, the presence of disorder and

frustration, the two ingredients usually considered necessary for a spin glass state, will be discussed. A study of the linear spin trimer model suggested by Onoda will be carried out and compared with the high temperature susceptibility results. The low temperature spin glass state is confirmed by the presence of magnetic irreversibility, slow relaxation of thermal remnant magnetization, and memory and rejuvenation effects. Furthermore, we also study the effect of magnetic field on the spin glass behavior by measuring the change of magnetization irreversibility as a function of magnetic field strength. It is found that the onset of irreversibility is suppressed to lower temperature at higher magnetic field.

NMR has proved a useful microscopic tool to study the local spin dynamics in spin glass systems.[31–35] In recent NMR studies in heavy fermion LiV_2O_4 containing a small amount of magnetic defects (~ 0.73 mol%), we found a stretched exponential behavior $1-M(t)/M(\infty) = \exp[-(t/T_1^*)^\beta]$ for the recovery of the ^{7}Li nuclear magnetization versus time $M(t)$ following a saturation pulse sequence in the temperature range 0.5–4.2 K.[36] Earlier μSR studies showed that LiV_2O_4 with 0.13 mol% magnetic defects undergoes a spin glass freezing below ~ 0.7 K.[37] The stretched exponential recovery is in strong contrast to a single exponential behavior observed in pure LiV_2O_4 samples, where no spin glass behavior was observed down to 20 mK. In order to better understand the relation between the stretched exponential recovery and the dynamics in spin glasses, it is highly desirable to study the nuclear spin-lattice relaxation behavior in other spin glass systems. We have found that the ^{7}Li nuclear spin lattice relaxation in $(Li_{0.33}V_{0.67})_3BO_5$ indeed follows a temperature dependent stretched exponential behavior.

It was previously shown[36, 38] that a unique distribution of nuclear spin lattice relaxation rates $1/T_1$'s can be obtained from the observed stretched exponential recovery with given fitted values of $1/T_1^*$ and β. In this paper, by assuming the presence of dynamical heterogeneity in the system, we derive the temperature-dependent distribution of the vanadium electronic spin relaxation times from the ^{7}Li relaxation data. Our NMR results reveal the persistence of a continuous broadening and dramatic slowing down of the electronic spin dynamics even under a strong (4.7 T) magnetic field as the *zero field* spin glass transition temperature is approached, in strong contrast to the magnetization results which show a suppression of the long range spin

glass transition in a field.

This chapter is organized as follows. Experimental details are presented in Sec. 6.2. The results of our structural studies are given in Sec. 6.3. Magnetization and NMR studies are presented in Sec. 6.4 and 6.5, respectively. In Sec. 6.6, we conclude this chapter with a summary and discussion of the main results.

6.2 Experimental

Crystals of $(Li_xV_{1-x})_3BO_5$ were grown under high purity argon gas flow with a flux consisting of $LiBO_2$ (4N, Alpha Aesar) and LiV_2O_4 with molar ratio 14.5:1. The x value is 0.4, as determined from the refinement below of the single crystal x-ray diffraction pattern. The mixture was contained in a platinum crucible and soaked at 1100 °C for 48 hours, then cooled at 1 °C/hr to 825 °C at which point the furnace was turned off to cool. The flux was removed by dissolving in hot water at 80 °C. The typical dimensions of the crystals were $0.3 \times 0.3 \times 6$ mm^3. LiV_2O_4 was prepared using standard solid state reaction. The starting materials were Li_2CO_3 (5N, Alfa Aeser), V_2O_5 (4N, MV Labs), and V_2O_3 (4N, MV Labs). Details of the LiV_2O_4 synthesis procedure are described in Ref. [39]. We note that this crystal growth method is different from that used in Ref. [30], where the flux instead consisted of $LiBO_2$ and $LiVO_2$.

The polycrystalline samples of $(Li_xV_{1-x})_3BO_5$ were made from a mixture of V_2O_3 (4N, MV Labs) and $LiBO_2$ (4N, Alpha Aesar) with molar ratio 1:1. The nominal composition was $(Li_{0.33}V_{0.67})_3BO_5$. The mixture of starting materials was ground and pelletized and then sealed inside a quartz tube under vacuum. It was then heated at 800 °C for 4 days and then air-quenched to room temperature.

Single crystal x-ray diffraction measurements were carried out on a Bruker SMART diffractometer with a graphite monochromator and Mo Kα radiation at $T = 293(2)$ K. The x-ray powder diffraction data were obtained at room temperature using a Rigaku Geigerflex diffractometer with a curved graphite crystal monochromator and Cu Kα radiation. The 2θ scan range was 10°–90° with 0.02° step size. Full profile Rietveld analyses on the powder x-ray diffraction pattern were carried out using EXPGUI,[40] an graphical user interface for

GSAS.[41]

Magnetization measurements were carried out using a Quantum Design SQUID magnetometer in the temperature T range 1.8–350 K and applied magnetic field H range 0–5.5 T. The crystals were aligned along the crystallographic c–axis using Duco cement (a and b axes randomly oriented) on a plastic film. The Duco cement and the plastic film are diamagnetic and contribute less than 2% to the total magnetization. Their contributions were subtracted to obtain the sample magnetization.

^{7}Li and ^{11}B NMR measurements were performed on the powder sample $(Li_{0.33}V_{0.67})_3BO_5$ in the T range 1.5–295 K. The typical saturation recovery sequence was used for nuclear spin lattice relaxation measurements. Spin–spin relaxation rates were measured by varying the separation between $\pi/2$ and π pulses which generated an echo. The typical $\pi/2$ pulse length was $3\,\mu$s. ^{7}Li NMR spectra were measured at $H = 3$ T. The spectra with narrow full width at half maximum intensity FWHM ≤ 100 kHz were obtained via the Fourier transform of half the echo signal, while broader spectra were measured by sweeping the RF frequency and recording the echo area at each point.

6.3 Crystal Structure

X-ray diffraction studies confirm that both our single crystal and polycrystalline samples have the same structure and approximately the same composition as reported in Ref. [30] ($x = 0.31$, 0.33). The system has an orthorhombic crystal structure (space group *Pbam*) as shown in Fig. 6.1, where Li or V occupy four inequivalent sites VL1–VL4 in each unit cell that are octahedrally coordinated by oxygen atoms.

The single crystal x-ray diffraction data were collected in the Miller index ranges of $-12 \leq h \leq 12$, $-16 \leq k \leq 16$, $-3 \leq l \leq 3$. A total of 2887 reflections were observed, among which 464 are independent reflections with intensity $I > 2\sigma$. Full-matrix least square refinement on F^2 was performed on those 464 independent reflections and 62 parameters were refined. The final R ($I > 2\sigma$) indices are $R_1 = 0.089$ and $wR_2 = 0.0444$. Both the lattice parameters and atomic positions are in good agreement with those reported in Ref. [30]. The lattice parameters are

$a = 9.177(2)$ Å, $b = 12.152(2)$ Å, and $c = 2.9891(5)$ Å, where the numbers in the parentheses give errors on the last digit. The occupation probability of vanadium atoms at VL1–VL4 sites are 0.82(1), 0.51(1), 0.40(1), and 0.56(1) respectively, which corresponds to a calculated $x = 0.40(1)$.

Figure 6.2 shows the observed and calculated (from Rietveld refinement) powder x-ray diffraction patterns for a powder sample of $(Li_{0.33}V_{0.67})_3BO_5$. Bragg peak positions and the difference between the observed and calculated peak intensities are also displayed. Weak V_2O_3 impurity peaks are present in the pattern. The amount of V_2O_3 impurity is estimated from the 2–phase Rietveld refinement to be ≈ 5 mol%. Isotropic thermal displacement parameters U were used during Rietveld refinement and their values were fixed to be equal to the equivalent thermal displacement parameter values U_{eff} for a single crystal obtained from the above single crystal refinement. The final agreement factors were $R_p = 7.2\%$, $R_{wp} = 9.3\%$ and reduced $\chi^2 = 2.54$. The occupation probability of vanadium atoms at VL1–VL4 sites are 0.96(1), 0.52(1), 0.47(1), and 0.48(1), respectively, which corresponds to $x = 0.35(1)$, in reasonable agreement with nominal value $x = 0.33$. The lattice constants a, b, and c are 9.1820(2), 12.1540(3), and 2.9872(1) Å, respectively.

By applying Goodenough's rules, the sign and relative strength of magnetic interactions among neighboring vanadium moments can be inferred from the structure.[42] The vanadium atoms occupy octahedral interstices of the oxygen sublattice and the octahedra are connected by either edge or corner sharing. Table 6.1 lists the VL–VL nearest neighbor distances and VL–O–VL bond angles. Since the vanadium cation has less than four d–electrons in its outer shell, according to Table I in Ref. [43], all nearest-neighbor vanadium-vanadium spin interactions are expected to be antiferromagnetic. For the edge sharing configuration, the vanadium-oxygen-vanadium interaction is expected to be much smaller than the direct vanadium-vanadium interaction which increases with decreasing distance.[43] Since the distance between nearest-neighbor VL1 and VL4 sites is much smaller than other VL–VL distances, Onoda[30] pointed out that the largest exchange interaction could exist between these two sites. Since each VL4 site is connected to two VL1 sites on either side, a VL1–VL4–VL1 linear spin trimer can be

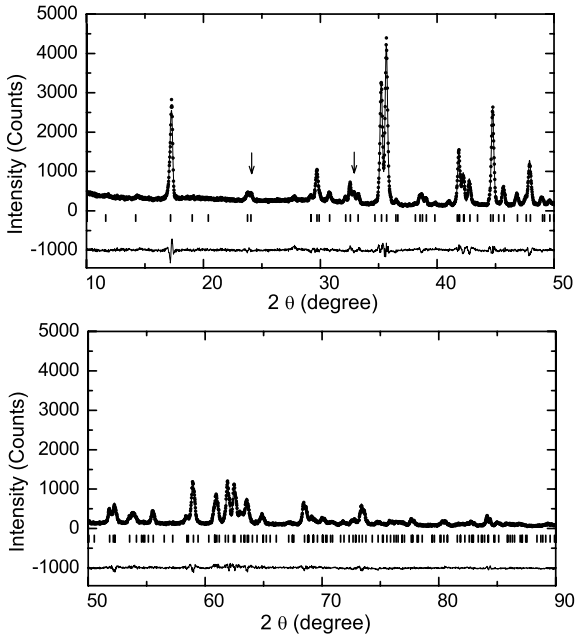

Figure 6.2 Observed and calculated x-ray diffraction patterns for $(Li_{0.33}V_{0.67})_3BO_5$ powder. The upper trace shows the observed data by dots and the calculated pattern by the solid line. The lower trace is a plot of the difference between the observed and calculated intensities. The vertical bars show the positions for the Bragg reflections of $(Li_{0.33}V_{0.67})_3BO_5$. The observed diffraction pattern indicates the presence of ≈ 5 mol% of V_2O_3 phase as estimated from the two-phase Rietveld refinement of the data. The arrows indicate the positions of the two strongest V_2O_3 peaks.

Table 6.1 Distances and bond angles of nearest neighbor VL–VL sites.

	Distance (Å)	VL–O–VL angle
Corner sharing		
VL1–VL2	3.3725	119.6°
VL2–VL3	3.4366	119.8°
Edge sharing		
VL1–VL2	3.0914	95.5° and 98.1°
VL1–VL3	2.9919	92.3° and 96.9°
VL1–VL4	2.7480	84.4° and 84.4°
VL2–VL4	3.0332	93.9° and 95.9°

formed. In the next section, a detailed study of the linear trimer model will be presented in an attempt to explain the high temperature susceptibility results.

Given antiferromagnetic interactions among all nearest neighbor vanadium spins, significant frustration for the magnetic interactions is expected. This is due to the presence of various triangles formed by nearest-neighbor VL sites, as one can see from Fig. 6.1. As a result, no spin configuration can minimize the exchange energy of all the vanadium–vanadium interactions. This geometric frustration effect is inherent in the structure and not induced by the disorder of the random Li and V occupation. The presence of both frustration and disorder is responsible for the low temperature spin glass phase at $T \lesssim 10$ K.

6.4 Magnetization

6.4.1 Magnetic Susceptibility

Figures 6.3(a) and 6.4(a) display the inverse susceptibility $(M/H)^{-1}$ versus temperature T in the T range 1.8–350 K and at applied magnetic field $H = 1$ T of the aligned crystals ($H \parallel c$) and the powder sample, respectively. Both sets of data were taken during field cooling. Measurements done on crystals with the c-axis parallel and perpendicular to the field gave almost the same results, indicating the absence of significant magnetic anisotropy in the system. As shown in Figs. 6.3(b) and 6.4(b), the magnetization M deviates from being proportional to H at low temperatures ($T \lesssim 20$ K for the powder sample). Such deviations are consistent with the appearance of a nonzero nonlinear susceptibility as the system approaches its spin glass

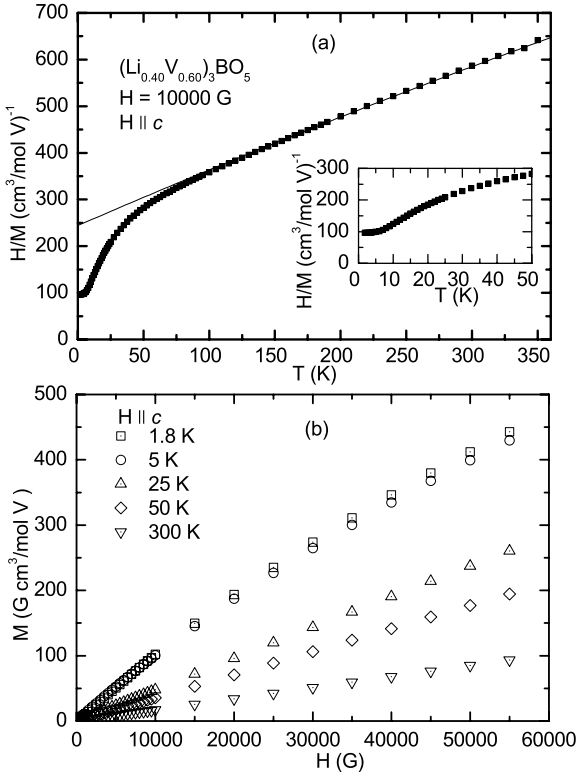

Figure 6.3 Magnetization of the aligned $(Li_{0.40}V_{0.60})_3BO_5$ crystals with magnetic field $H \parallel c$. (a) Inverse magnetization over field, H/M, measured at $H = 10000$ G. The data were taken during field cooling. The solid curve is a fit to the 200–350 K data by Eq. (6.1). Inset: expanded plot of the low temperature data. (b) $M(H)$ isotherms at $T = 1.8$, 5, 25, 50, and 300 K. A negative curvature was observed at 1.8 and 5 K.

transition temperature.[44] The evidences for a spin glass state at low temperatures ($T < 10$ K) will be discussed in detail below.

For both the single crystal sample and the powder sample, the high T ($T > 100$ K) region of the susceptibility can be described by a constant plus a Curie-Weiss term

$$\chi(T) = \chi_0 + \frac{C}{T - \theta}. \tag{6.1}$$

A fit to the susceptibility data of the single crystals in the T range 200–350 K gives $\chi_0 = 0.0002(1)$ cm^3/mol V, $C = 0.74(9)\,\mathrm{cm^3\,K/mol\,V}$ and $\theta = -190(27)$ K. The constant term χ_0 arises mainly from the diamagnetism of the ion cores and the paramagnetic Van Vleck susceptibility of the vanadium atoms. We estimate χ^{core} to be -4.3×10^{-5} cm^3/mol V, using

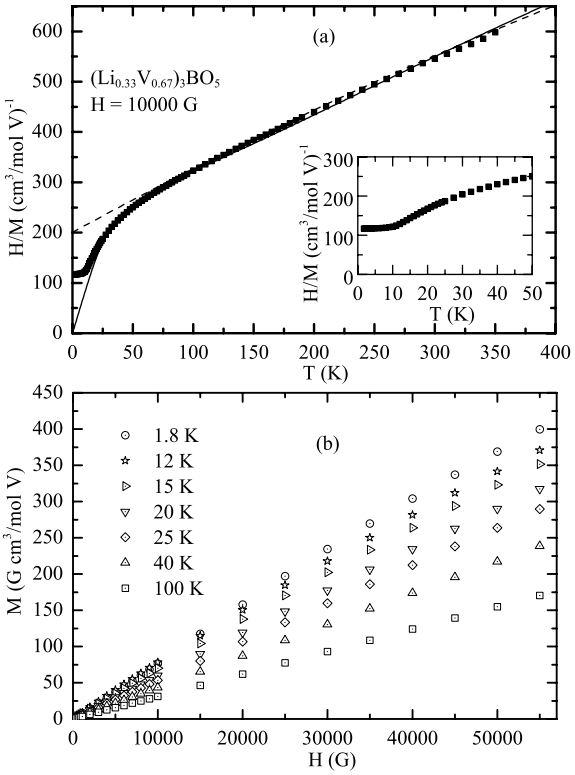

Figure 6.4 Magnetization M of the $(Li_{0.33}V_{0.67})_3BO_5$ powder sample. (a) Inverse M over field H, H/M, versus H, measured at $H = 10000$ G. The data were taken during field cooling. The dashed line is a fit to the 200–350 K data by Eq. (6.1) and the solid line is a fit to the 20–350 K data by Eq. (6.8). Inset: expanded plot of the low temperature data. (b) M versus H isotherms at different temperatures.

the values -0.6, -10, -7, -35, and -12×10^{-6} cm^3/mol for Li^+, V^{3+}, V^{4+}, $(BO_3)^{3-}$, and O^{2-} ions.[45] The Van Vleck susceptibility is thus $\chi^{VV} = \chi_0 - \chi^{core} = 0.0002(1)$ cm^3/mol V. This value is of the same order as the values of Van Vleck susceptibility of vanadium ions in LiV_2O_4, VO_2, and $LaVO_3$.[39] The value of the Curie constant C can be compared with that predicted by the molecular field theory.[46] Assuming the vanadium atoms in the crystals are in either +3 (spin $S = 1$) or +4 ($S = 1/2$) oxidation states, the Curie constant is given by

$$C = \frac{N_A \mu_B^2}{3k_B}\left[2fg_1^2 + \frac{3}{4}(1-f)g_2^2\right], \tag{6.2}$$

where f is the fraction of trivalent vanadium moments and g_1 and g_2 are g-factors for trivalent and tetravalent vanadium moments, respectively. $x = 0.4$ corresponds to $f = 0.8$. Equation (6.2) thus gives $C = 0.82$ cm^3 K/mol V assuming $g_1 = 1.93$ (Ref. [47]) and $g_2 = 1.97$,[48] respectively. This value is within the error bar of the observed Curie constant $C = 0.74(9)$ cm^3 K/mol V.

A fit of Eq. (6.1) to the data of the powder sample in the T range 200–350 K gives $\chi_0 = 0.0003(1)$ cm^3/mol V, $C = 0.67(5)$ cm^3 K/mol V and $\theta = -143(16)$ K. In the polycrystalline sample, all the vanadium atoms are in the +3 charge state, so Eq. (6.2) gives $C = 0.93$ cm^3 K/mol V assuming $f = 1$ and $g = 1.93$, which is much higher than the observed value. A second polycrystalline sample with the same composition $(Li_{0.33}V_{0.67})_3BO_5$ was made using the same procedure and a fit of Eq. (6.1) to its susceptibility data in the same temperature range gave $C = 0.56(6)$ cm^{3}K/mol V, $\chi_0 = 0.0005(1)$ cm^3/mol V, and $\theta = -99(6)$ K. The Curie constants between the two powder samples match within experimental error while there is a significant difference in the θ. The reason for the discrepancy in θ values is not known. We note that a lower than calculated Curie constant is also present in Ref. [30], where $C = 0.77$ cm^3 K/mol V and $\theta = -125$ K for a powder sample with the same x value as our powder samples.

To understand the difference between the measured and expected Curie constants in the powder samples, we will first discuss the effect of V_2O_3 and possible amorphous $LiBO_2$ impurities on the magnetization results. The above Rietveld refinement of the powder x-ray diffraction data indicates that our powder sample contains 5 mol% V_2O_3 impurity. V_2O_3 un-

dergoes a first order phase transition from paramagnetic metal to antiferromagnetic insulator at around 170 K. Above 170 K, it has an almost temperature independent susceptibility of 5×10^{-4} cm^3/mol V,[49] so this phase will not contribute to the high temperature Curie-Weiss term in Eq. (6.1). The contribution of 5 mol% of V_2O_3 to the constant term χ_0 in $(Li_{0.33}V_{0.67})_3BO_5$ is therefore about 0.25×10^{-4} cm^3/mol V,[49] which is within the error bar of the fitting result of χ_0. $LiBO_2$ is non-magnetic and its contribution to the susceptibility should also be negligible. The presence of 5 mol% V_2O_3 impurities leads to an overestimate of the $(Li_{0.33}V_{0.67})_3BO_5$ sample mass by 5%, assuming the same molar percentage of amorphous $LiBO_2$ impurity is present in the sample.

The above analysis shows that the presence of impurities is insufficient to explain our low observed Curie constants in the powder sample. The reason for this discrepancy is currently not understood. It is noted that molecular field theory predictions are generally valid only in the high temperature limit $T \gg |\theta|$, which is not satisfied in our temperature range 200–350 K due to the large values of $|\theta|$. However, this limitation should also apply to the single crystal case, where the discrepancy between observed and calculated Curie constants is much smaller, although the condition $T \gg |\theta|$ is even less satisfied due to the higher $|\theta|$ value in the crystals.

6.4.2 Linear trimer model

Below ~ 100 K, the slope of the H/M versus T curve in Fig. 6.3(a) increases with decreasing temperature. As proposed in Ref. [30], this could be due to the existence of spin trimers with antiferromagnetic nearest-neighbor interactions. A spin trimer has a low spin ground state, which is separated from the first excited state by an energy gap of the order of the exchange constant J. At temperatures $T \ll J$, the effective number of spins is reduced, which results in a reduction of the effective Curie constant. Therefore, the slope at low temperature increases in Figs. 6.3(a) and 6.4(a) since it is inversely proportional to the Curie constant. The possibility of trimer formation was indicated by the short distances between VL1 and VL4 sites as discussed in Sec. 6.3. The expected behavior of susceptibility versus temperature in this trimer model can be analyzed most easily when all the vanadium spins have the same spin value. This is

Table 6.2 Eigenstates, eigenvalues E, and degeneracies n of the linear trimer Hamiltonian Eq. (6.3).

E (J)	2	1	0	-1	-1	-2	-3
S_{T}	3	2	1	1	2	0	1
S_{13}	2	1	0	1	2	1	2
n	7	5	3	3	5	1	3

the case in the polycrystalline sample where all vanadium spins have $S = 1$.

The Hamiltonian for a linear trimer can be written as

$$\begin{aligned} \mathcal{H} &= J(\mathbf{S_1}\cdot\mathbf{S_2}+\mathbf{S_2}\cdot\mathbf{S_3}) \\ &= \frac{J}{2}[(\mathbf{S_1}+\mathbf{S_2}+\mathbf{S_3})^{\mathbf{2}}-(\mathbf{S_1}+\mathbf{S_3})^{\mathbf{2}}-\mathbf{S_2^2}] \\ &= \frac{J}{2}[\mathbf{S_T^2}-\mathbf{S_{13}^2}-\mathbf{2}], \end{aligned} \tag{6.3}$$

where $J > 0$ is the antiferromagnetic nearest-neighbor exchange coupling constant between vanadium moments at adjacent VL1 and VL4 sites, $\mathbf{S_1}$ and $\mathbf{S_3}$ are the spins at the two VL1 sites at the two ends of a trimer, $\mathbf{S_2}$ is the spin at the VL4 site in the middle of the trimer, and $\mathbf{S_T} \equiv \mathbf{S_1}+\mathbf{S_2}+\mathbf{S_3}$ and $\mathbf{S_{13}} \equiv \mathbf{S_1}+\mathbf{S_3}$. The different eigenstates of this Hamiltonian, as well as their corresponding energy eigenvalues and degeneracies are listed in Table 6.2. The partition function Z_{T} and molar spin susceptibility χ_{T} of the trimers are

$$Z_{\mathrm{T}} = \sum_i n_i \mathrm{e}^{-E_i/k_{\mathrm{B}}T} \tag{6.4}$$

and

$$\chi_{\mathrm{T}} = \frac{N_{\mathrm{A}} g^2 \mu_{\mathrm{B}}^2}{3k_{\mathrm{B}}TZ_{\mathrm{T}}} \sum_i n_i S_{\mathrm{T}i}(S_{\mathrm{T}i}+1)\mathrm{e}^{-E_i/k_{\mathrm{B}}T}, \tag{6.5}$$

where the index i runs over all the different states listed in Table 6.2.

One also needs to consider the presence of dimers. Dimers are formed when one of the VL1 sites at the two ends of the trimer is instead occupied by a Li atom. The molar spin susceptibility of dimers consisting of two spins 1 can be obtained in the same way and the result is

$$\chi_{\mathrm{D}} = \frac{N_{\mathrm{A}} g^2 \mu_{\mathrm{B}}^2}{k_{\mathrm{B}}TZ_{\mathrm{D}}}(10\mathrm{e}^{-3J/k_{\mathrm{B}}T}+2\mathrm{e}^{-J/k_{\mathrm{B}}T}), \tag{6.6}$$

where $Z_{\mathrm{D}} = 5\mathrm{e}^{-3J/k_{\mathrm{B}}T}+3\mathrm{e}^{-J/k_{\mathrm{B}}T}+1$ is the partition function of the dimer Hamiltonian. At temperatures much higher than the typical interactions between the dimer, trimer and isolated

spins, which is presumably of the order of the zero field spin glass transition temperature $T_g \lesssim 10$ K,[46] the total susceptibility of the system is

$$\chi = \frac{f_3}{3}\chi_T + \frac{f_2}{2}\chi_D + \frac{2N_A g^2 \mu_B^2}{3k_B T}(1 - f_2 - f_3) + \chi_0, \tag{6.7}$$

where f_2 and f_3 are the fractions of vanadium atoms belonging to dimers and trimers, respectively, and the third term gives the contribution from isolated $S = 1$ spins. Equation (6.7) with $g \approx 2$ does not fit the experimental data over any appreciable temperature range with f_2, f_3, J and χ_0 as free fitting parameters. However, a reasonable fit to the data can be achieved after scaling the temperature dependent part by a prefactor $b < 1$:

$$\chi = b\Big[\frac{f_3}{3}\chi_T + \frac{f_2}{2}\chi_D + \frac{2N_A g^2 \mu_B^2}{3k_B T}(1 - f_2 - f_3)\Big] + \chi_0. \tag{6.8}$$

The prefactor $b < 1$ is introduced as an attempt to isolate the unknown effects causing the difference between calculated and measured Curie constants discussed in section 6.4.1. Shown as the solid curve in Fig. 6.4(a) is the fitting result of Eq. (6.8). The best fit parameters are $f_2 = 0.76(18)$, $f_3 = 0.04(29)$, $J = 109(17)$ K, and $b = 0.61(1)$ with χ_0 fixed to 0.0003 cm^3/mol V and g fixed to 1.93. From the occupation probabilities of vanadium atoms at VL1–VL4 sites as determined from Rietveld refinement, one expects

$$f_2 = \frac{4p_1p_4(1 - p_1)}{2p_1 + 2p_2 + p_3 + p_4} = 0.02 \tag{6.9}$$

and

$$f_3 = \frac{3p_1^2p_4}{2p_1 + 2p_2 + p_3 + p_4} = 0.34, \tag{6.10}$$

where p_1 to p_4 are the occupation probabilities of vanadium atoms at the VL1 to VL4 sites, respectively. The expected values are in large discrepancy with the above fitting results of $f_2 = 0.76$ and $f_3 = 0.04$. We conclude that the above model of isolated monomers, dimers and trimers cannot explain the susceptibility data at high temperatures. Most likely, interactions between those spin objects need to be considered and antiferromagnetic spin clusters form as the temperature approaches the zero field T_g from above, which results in a reduction of the effective Curie constant and a negative curvature in inverse susceptibility versus temperature, qualitatively similar to the behavior expected from above spin trimer model.

6.4.3 Spin glass behavior

In order to confirm the spin glass state at low temperatures as proposed in Ref. [30], we first compare the magnetization results measured under zero-field-cooled (ZFC) and field-cooled (FC) conditions. Figure 6.5 shows the splitting of ZFC and FC magnetization at low temperatures at H = 10, 100, 1000, and 10000 G in the aligned single crystals. The FC magnetization was measured on cooling. For the polycrystalline sample, a similar splitting is observed below 8.5 K at H = 100 G as shown in Fig. 6.6. The ZFC–FC bifurcation is a signature for the presence of a spin glass state at low temperatures.[52] The onset temperature of ZFC and FC magnetization splitting at the lowest field is referred to as the zero field spin glass transition temperature $T_{\rm g}$ throughout this chapter. For the single crystals $T_{\rm g}$ = 5.5 K while for the powder sample $T_{\rm g}$ = 8.5 K. The ratio $|\theta|/T_{\rm g}$ is an empirical measure of geometric frustration in a system.[50] This ratio is 35(5) and 17(2) for our crystal and polycrystalline samples, respectively, indicating the presence of strong frustration in the system. It is noted in Fig. 6.5 that even above $T_{\rm g}$, there are slight differences between zero-field cooled and field-cooled magnetizations. However, these slight differences are within the experimental error and not related to the spin glass behavior. The magnitude of ZFC–FC bifurcation was gradually suppressed and the onset temperature of the strong bifurcation decreases with increasing magnetic field. This suggests that the spin glass transition temperature is suppressed to lower temperatures with increasing field. In the next section, we will apply NMR to further study the effect of magnetic fields on the spin dynamics of the system.

In a ferromagnetic sample, similar ZFC-FC splitting could arise due to the presence of domain walls between neighboring ferromagnetic domains.[51] In order to exclude such a possibility, we performed measurements of the magnetization versus applied magnetic field $M(H)$ hysteresis loops. Figure 6.7(a) displays M versus H in the aligned crystals as the field was cycled between -5.5 and 5.5 T at T = 1.8 and 4.2 K. The curves were taken immediately after the crystal was zero-field-cooled to 1.8 or 4.0 K from above 5.5 K. The hysteresis of the M versus H curves observed with field cycling is very small as shown in the inset of Fig. 6.7(a). The absence of significant hysteresis suggests that a ferromagnetic transition is not the origin

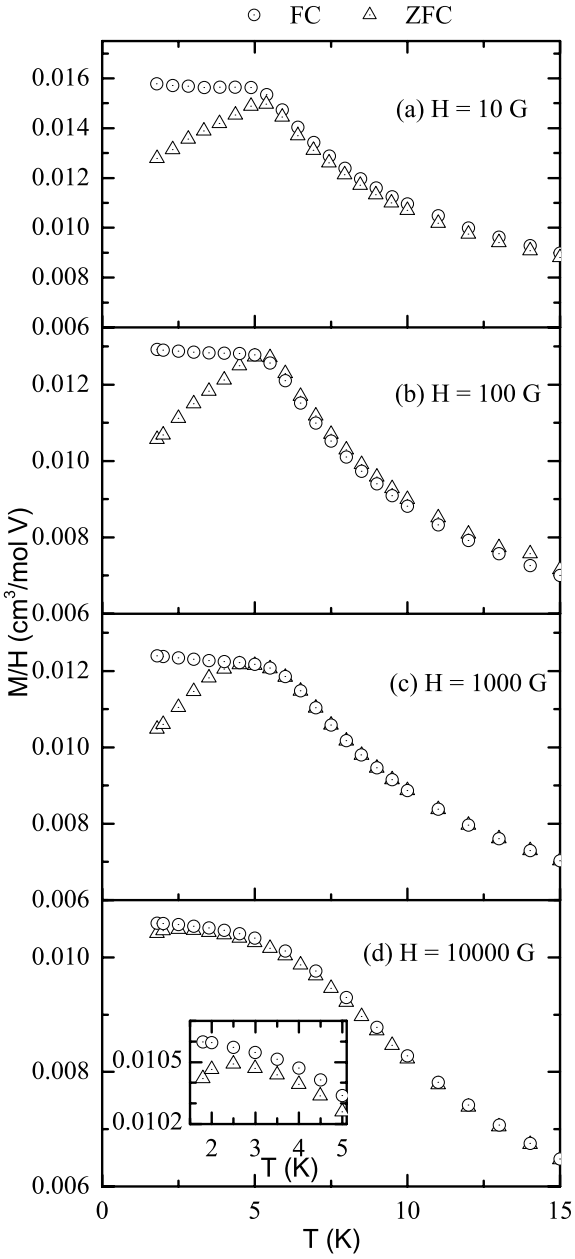

Figure 6.5 Splitting of field-cooled (FC) and zero-field-cooled (ZFC) magnetization M versus temperature T of $(Li_{0.40}V_{0.60})_3BO_5$ crystals at low temperatures and H = 10, 100, 1000, and 10000 G. The FC magnetizations were measured on cooling. The inset on the bottom panel is an expanded plot of the low temperature region.

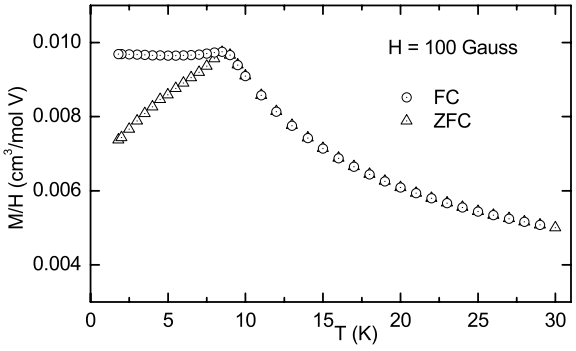

Figure 6.6 Splitting of field-cooled (FC) and zero-field-cooled (ZFC) magnetization M versus temperature T of the $(Li_{0.33}V_{0.67})_3BO_5$ powder sample below $T_g = 8.5$ K and at $H = 100$ G. The FC magnetization was measured on cooling.

of the ZFC–FC splitting.

Slow decaying of thermal remnant magnetization is considered as one of the defining properties of spin glass systems.[52] Figure 6.7(b) shows the decrease with time of the remnant magnetization after turning off a field $H = 1000\,\mathrm{G}$ at 2.0 K. The field was turned off immediately after the crystals were field-cooled to 2.0 K from above 5.5 K. The long time behavior can be fitted by a stretched exponential function,

$$M_R(t) = M_0 \cdot \exp[-(t/\tau)^{\beta}]. \tag{6.11}$$

The best fit to the data at $t > 18\,\mathrm{min}$ (solid line in Fig. 6.7) gave $M_0 = 3.24(6)\,\mathrm{G\,cm^3/mol\,V}$, $\tau = 7300(1400)$ min, and $\beta = 0.086(2)$. Relaxation as described by Eq. (6.11) with similar values of β was observed in other spin glass systems.[53, 54]

To further confirm the spin glass state of the system, we studied memory and rejuvenation effects in $(Li_xV_{1-x})_3BO_5$, following the method used by Sun et al.[55] The main panel of Fig. 6.8 shows the development of magnetization following application of a 50 G magnetic field immediately after the crystal was zero-field-cooled to 3.0 K from above 5.5 K. The crystal was then quickly cooled to 1.8 K after staying at 3.0 K for $t_1 \approx 260\,\mathrm{minutes}$. A sharp increase of magnetization was observed right after the cooling. However, after the temperature was increased back to 3.0 K after another $t_2 \approx 230\,\mathrm{minutes}$, the magnetization returned back to the value just before cooling to 1.8 K and the magnetization continued to evolve as if the t_2

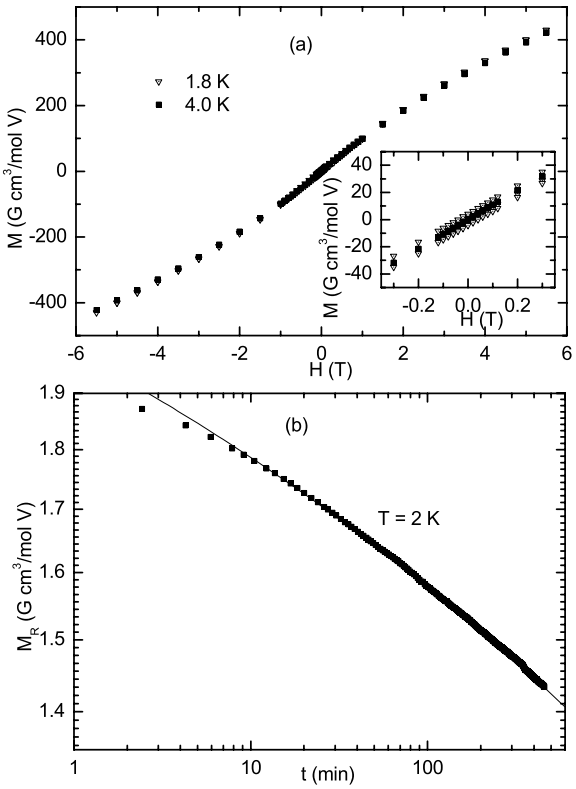

Figure 6.7 (a) Magnetization M versus the external magnetic field H in the aligned single crystals as H was cycled between 5.5 and -5.5 T at $T = 4.2$ and 1.8 K. The field was parallel to the c-axis. Inset: Expanded plot of the low field region. (b) Relaxation of remnant magnetization $M_{\rm R}$ of crystals versus time t after turning off a field of 1000 G at 2.0 K immediately after field-cooling from above 5.5 K. The solid curve is a fit by Eq. (6.11) to the data at $t > 18$ min.

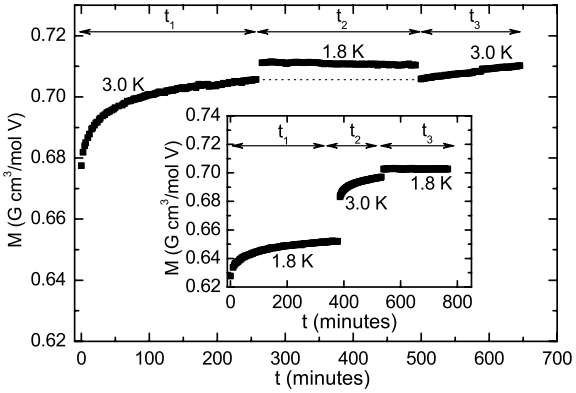

Figure 6.8 Memory and rejuvenation effects in the aligned single crystals of $(Li_{0.4}V_{0.6})_3BO_5$. The field was parallel to the c-axis. Main panel (inset): development of magnetization after turning on a field of 50 G immediately after the crystals were zero-field--cooled to 3.0 K (1.8 K). After time t_1, the temperature was quickly changed to 1.8 K (3.0 K) and kept at that temperature for time t_2. Then the temperature was changed back to 3.0 K (1.8 K). The field was kept at 50 G during the whole process.

stage did not take place. Such a memory effect was not observed if the temperature during the t_2 stage was higher than during t_1 and t_3. As displayed in the inset of Fig. 6.8, where the respective temperatures during t_2 and during t_1 and t_3 were switched, the magnetization at the beginning of t_3 did not return to the value right before the temperature change to 3.0 K took place. Instead, the rejuvenation effect was observed right after the temperature changed to 3.0 K (at the beginning of stage t_2): the magnetization reinitialized as if the t_1 stage did not take place. The asymmetry effects between heating and cooling during t_2 could be attributed to a hierarchical organization of the free energy landscape in the spin glass phase space.[55, 56] It is noted that recent studies demonstrate that the above memory and rejuvenation effects can also arise from a collection of isolated nanoparticles with a temperature dependent distribution of relaxation times.[57] However, considering the random distribution of Li and V atoms within the structure, the occurrence of isolated nanoclusters should have a very small probability.

6.5 NMR

6.5.1 Introduction

We carried out nuclear magnetic resonance (NMR) studies in order to further study the spin freezing properties in strong magnetic field of a material that has a spin glass transition in zero field. Furthermore, we investigated the dynamical inhomogeneities in the system and extracted the distribution of electronic spin relaxation times from nuclear spin lattice relaxation measurements.

A search for a ^{51}V NMR signal was performed in the frequency range 51.8–53.1 MHz at T = 295 K and H = 4.7 T (Larmor frequency = 52.6 MHz). The separation between the two RF pulses which could generate an echo was 20 μs. Considering the possibility of a strong quadrupole effect which could decrease the $\pi/2$ pulse length of the central transition,[58] various pulse length combinations were used at each frequency. However, no ^{51}V NMR signal could be detected under the above conditions. We thus performed NMR measurements on ^{7}Li and ^{11}B nuclei as follows. Both ^{7}Li and ^{11}B nuclei have spin $I = 3/2$. No observable quadrupole effect was observed for ^{7}Li while ^{11}B displayed clear quadrupole splitting in the spectrum. The difference is attributed to different local electric field gradients (EFG) of these two nuclei, since the quadrupole moment of ^{7}Li nucleus is 2.8 times that of ^{11}B.[59] All NMR measurements were performed on the powder sample of $(Li_{0.33}V_{0.67})_3BO_5$ which has a zero field spin glass temperature of 8.5 K as shown previously in Fig. 6.6.

6.5.2 ^{7}Li NMR Spectrum

The ^{7}Li NMR spectrum in the powder $(Li_{0.33}V_{0.67})_3BO_5$ sample shows a single line without an observable quadrupolar effect. A strong broadening of the spectrum is observed with decreasing temperature. Figure 6.9 displays the spectrum at H = 3 T at different temperatures. In contrast to the strong inhomogeneous broadening, the peak positions of the spectra remain almost temperature independent (shift $< 0.1\%$ of the resonant frequency), consistent with broadening due to dipolar interactions with vanadium local moments with weak g-factor anisotropy.[60, 61]

The temperature dependence of the full width at half maximum (FWHM) peak intensity of the spectra is plotted in Fig. 6.10. The FWHM vs T at $T > 8.5$ K can be well fitted by a Curie-Weiss law plus a constant,

$$\mathrm{FWHM} = C_0 + C_1/(T - \theta_1), \tag{6.12}$$

where the best-fit parameters are $C_0 = 38(3)$ kHz, $C_1 = 3.5(4)$ MHz and $\theta_1 = 5.5(7)$ K. This fit is plotted as the solid line in Fig. 6.10. The following analysis shows that the strong broadening of the spectrum at low temperatures must be due to inhomogeneity of static local magnetic fields (inhomogeneous broadening). The intrinsic line width of each ^{7}Li nuclear spin is of the order of $1/T_2$, the inverse of spin-spin relaxation time. As will be shown below in Table 6.3, the effective spin-spin relaxation time for the detected ^{7}Li nuclear spins is $\gtrsim 100$ μs at $T > 8.5$ K, which corresponds to an intrinsic line width of the order of 10 kHz, much smaller than the observed line width below ~ 50 K (see Fig. 6.10). The full width at half maximum at 4.2 K is approximately 2 MHz, corresponding to a local field distribution of width ~ 0.1 T. This width is of the same order as the root mean square (rms) values of the local dipolar fields at the ^{7}Li nuclear sites, as will be shown below [see Eqs. (6.17) and (6.20)].

The inset of Fig. 6.10 shows FWHM versus M/H at $H = 3.00$ T with temperature as the implicit variable. At $T \lesssim 30$ K, FWHM deviates strongly from being proportional to magnetization and increases much faster than the magnetization with decreasing temperature. One possible explanation of such deviation might be the occurrence of antiferromagnetically coupled clusters. In systems with dense paramagnetic moments, the inhomogeneous broadening is proportional to $\sqrt{n}\langle S_z\rangle$, where n and $\langle S_z\rangle$ are the concentration and field-induced spin polarizations of the paramagnetic moments, respectively.[59] On the other hand, the magnetization M is proportional to $n\langle S_z\rangle$. The concentration n of *effective* paramagnetic moments decreases in the system if small antiferromagnetic clusters (including the above mentioned spin dimers and trimers in their ground states) occur with decreasing temperature. Because of the above different dependences of FWHM and M on concentration n, the FWHM increases faster than M with decreasing temperature. We note that the formation of antiferromagnetic spin clusters is qualitatively consistent with the negative curvature in the inverse susceptibility versus

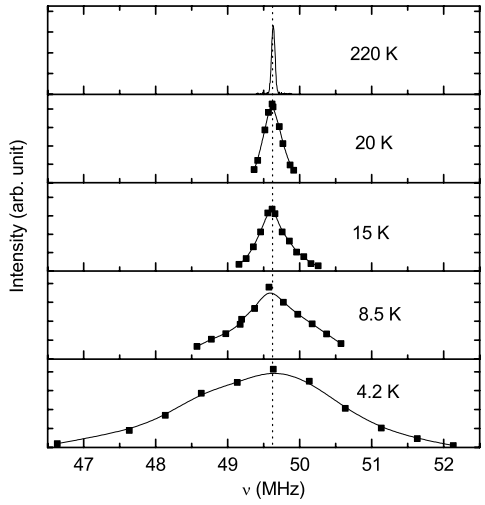

Figure 6.9 ^{7}Li NMR spectrum at temperatures $T = 220$, 20, 15, 8.5, and 4.2 K and an external magnetic field $H = 3$ T. The spectrum at 220 K was obtained by Fourier transform of half echo signal while spectra at low temperatures obtained by frequency sweep. The squares are data points and the solid lines are guides to the eye. The zero field spin glass transition temperature is $T_{\rm g} = 8.5$ K (see text). The vertical dotted line marks the position of the ^{7}Li resonance in aqueous lithium chloride solution.

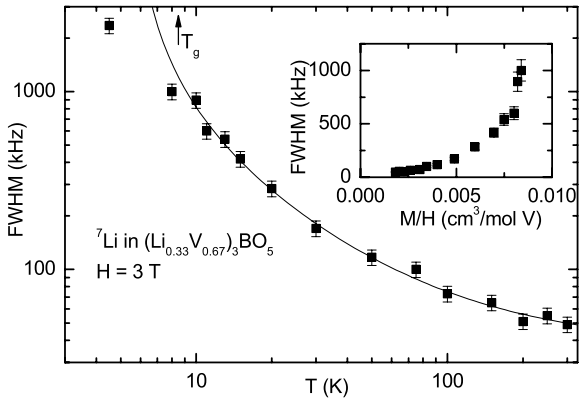

Figure 6.10 Full width at half maximum (FWHM) peak intensity of the ^{7}Li NMR spectrum versus temperature T at applied magnetic field $H = 3.00$ T. The vertical arrow indicates the zero field spin glass transition temperature $T_{\rm g} = 8.5$ K. The solid curve is a phenomenological fit by Eq. (6.12). Parameters for the fit are given in the text. Inset: FWHM vs magnetization divided by field M/H at $H = 3.00$ T with temperature as the implicit variable.

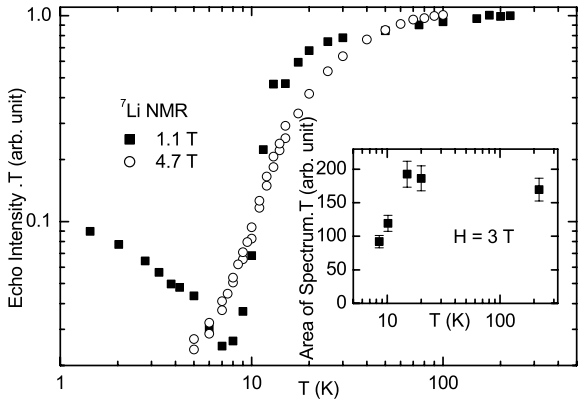

Figure 6.11 Temperature T dependence of normalized ^{7}Li NMR echo intensity at $H = 1.1$ and 4.7 T. Inset: T times area of the whole spectrum at $H = 3.0$ T after correction for the T_2 effect.

temperature below $T \sim 100$ K in Figs. 6.3(a) and 6.4(a) as discussed in Sec. 6.4 B above.

6.5.3 ^{7}Li NMR Signal Intensity

A minimum in normalized NMR signal intensity was observed long ago in metallic spin glass systems close to the zero-field spin glass transition temperature.[32, 35] The normalized echo intensity for ^{7}Li in $(Li_{0.33}V_{0.67})_3BO_5$ at $H = 1.1$ and 4.7 T shows similar behavior as displayed in the main panel of Fig. 6.11. The echo intensity was measured by the area under the absorption line obtained through Fourier transformation of half the echo signal and was normalized by multiplying by T to compensate for the nuclear Curie law for the equilibrium longitudinal nuclear magnetization. The resulting value should then be proportional to the number of ^{7}Li nuclei detected in the experiments. Two factors can contribute to the loss of this signal intensity. The first factor is the limited frequency window of the NMR spectrometer ($\Delta f \sim 200$ kHz). Due to the strong inhomogeneous broadening of the spectrum at low temperatures, the nuclei with a resonant frequency outside the NMR spectrometer window cannot be detected. The second factor is the shortening of the spin-spin relaxation times around the spin glass transition temperature. Since the $\pi/2$ and π pulse separation for echo generation was fixed to 20 μs, a reduction of T_2 to less than 40 μs can also result in a decrease of signal intensity.

Table 6.3 ^{7}Li nuclear spin-spin relaxation times at $H = 3.0\,\mathrm{T}$ and different temperatures. The parameters T_2 and $T_{2\mathrm{g}}$ are defined in Eq. (6.13).

T(K)	8.5	10.2	15	20	90	175	295
$T_2\,(\mu\mathrm{s})$	76(4)	88(5)	258(13)	442(22)	∞	∞	∞
$T_{2\mathrm{g}}\,(\mu\mathrm{s})$	∞	∞	712(35)	571(29)	359(18)	293(15)	307(15)

These two factors can be partly compensated by measuring the area of the whole absorption spectrum and then multiplying by a T_2 correction factor.[62] To carry out the compensation, we first integrate the spectra in Fig. 6.9, with the parts of the spectra further away from the measured parts estimated by linearly extrapolating the wings until zero intensity was reached. In order to determine the T_2 correction factor at each temperature, spin-spin relaxation rates were measured at a few temperatures as shown in Fig. 6.12. At high temperatures the ^{7}Li nuclear magnetization versus RF pulse separation follows square exponential decay (half Gaussian) while it crosses over to a single exponential decay with decreasing temperatures. We describe the decay of the spin-echo amplitude by the expression

$$A(t) = A_0 \cdot \exp[-(t/T_{2\mathrm{g}})^2 - t/T_2]. \tag{6.13}$$

Table 6.3 lists the values of $T_{2\mathrm{g}}$ and T_2 at different temperatures. It was found that the values of $T_{2\mathrm{g}}$ and T_2 at different parts of the spectrum are almost the same so that a single T_2 correction factor is used for the whole spectrum. The inset of Fig. 6.11 shows the T dependence of T times the area of the whole spectrum after multiplying by the T_2 correction factor $\exp[(t/T_{2\mathrm{g}})^2 + t/T_2]$ with $t = 40\,\mu\mathrm{s}$. The signal loss at high temperatures is now fully recovered. However, at $T \lesssim 15$ K, close to the zero-field spin glass transition temperature, signal intensity loss is still observed. This indicates that at $T \lesssim 15$ K, some of the nuclei have T_2 values much shorter than $40\,\mu\mathrm{s}$ so that their signal cannot be compensated by the above T_2 correction factor, rendering them unobservable [see Fig. 6.15 and the discussion following Eq. (6.19) below].

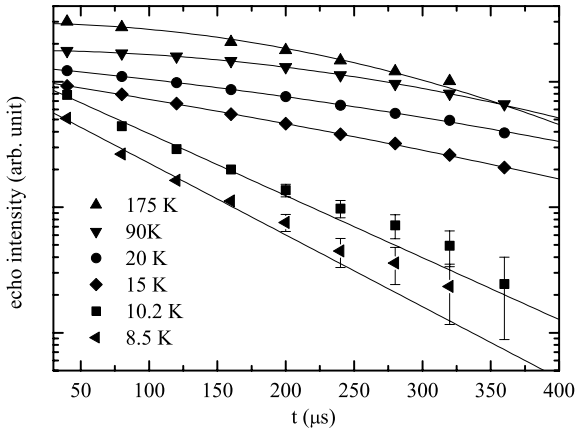

Figure 6.12 ^{7}Li NMR echo intensity versus twice the pulse spacing t between the $\pi/2$ and π pulses that generate an echo at different temperatures at $H = 3.0$ T. The solid lines are fits by Eq. (6.13) with parameter values listed in Table 6.3.

6.5.4 ^{7}Li Nuclear Spin Lattice Relaxation

The recovery of the longitudinal nuclear magnetization $M(t)$ following saturation changes from a single exponential to a stretched exponential function as the system approaches the zero-field spin glass transition temperature T_g from above as displayed in Fig. 6.13. Due to the strong inhomogeneous broadening of the spectrum, it became difficult to saturate the whole line with the RF comb pulses and only the central part of the spectrum can be saturated. A possible origin for the observed stretched exponential is thus spectral diffusion, i.e. transfer of Zeeman energy from saturated to unsaturated spins at other parts of the spectrum. In order to check such a possibility, the nuclear spin lattice relaxation measurements at 4.7 T and below 15 K were performed using two different saturation pulse sequences. The first saturation sequence consisted of 20 $\pi/2$ pulses with separation between neighboring pulses equal to 50 μs, while the second saturation sequence consisted of 10 $\pi/2$ pulses with separation between neighboring pulses of 300 μs. The duration of the $\pi/2$ pulses is equal to 4.7 μs in both cases. The recovery curves obtained in both conditions were the same at each temperature, which strongly suggests that the observed nonexponential recovery is intrinsic to the sample and is not related to artificial effects such as spectral diffusion. The effect of spectral diffusion depends on the degrees of saturation of the nuclear spins away from the center of the spectrum,

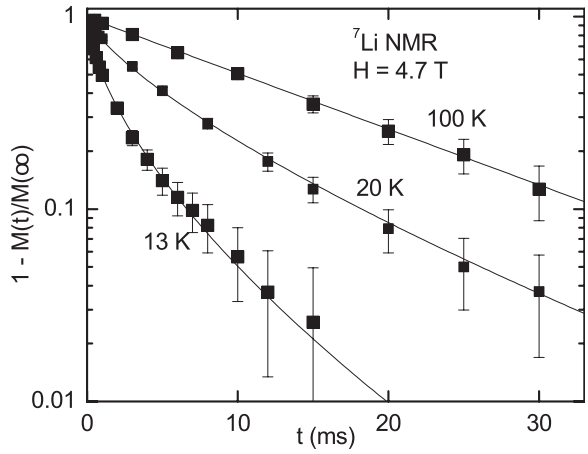

Figure 6.13 ^{7}Li NMR nuclear spin lattice relaxation versus time t in $(Li_{0.33}V_{0.67})_3BO_5$ powder sample following a saturation pulse sequence at $H = 4.7$ T and $T = 100$, 20, and 13 K. Solid curves are fits by Eq. (6.14).

which are expected to be different between the above two pulse sequences.

$M(t)$ can be fitted with a stretched exponential function with a variable $1/T_1^*$ and variable exponent β

$$1 - \frac{M(t)}{M(\infty)} = \exp[-(t/T_1^*)^\beta]. \tag{6.14}$$

The physical meanings of the parameters $1/T_1^*$ and β have been discussed in recent papers.[36, 38] Figure 6.14 shows the temperature dependence of $1/T_1^*$ and β at $H = 1.1$ and 4.7 T. Note that the results at low temperatures ($T < 20$ K) were obtained from measurements on only a small fraction of ^{7}Li nuclei in the system (see Fig. 6.11). The crossover from a single exponential to stretched exponential relaxation is represented by β decreasing below unity with decreasing T. $1/T_1^*(T)$ shows a sharp enhancement close to the zero field spin glass transition temperature T_g in both fields. While $1/T_1^*$ strongly depends on the field close to the transition temperature, $\beta(T)$ is almost temperature and field independent near and below T_g.

In the limit of small perturbation of nuclear Zeeman levels as is usual in NMR, one can apply the weak collision formula for the nuclear spin lattice relaxation rate (NSLR), where NSLR arises from the Fourier component at $\omega_n = \gamma_{Li}H$ of the fluctuating magnetic field

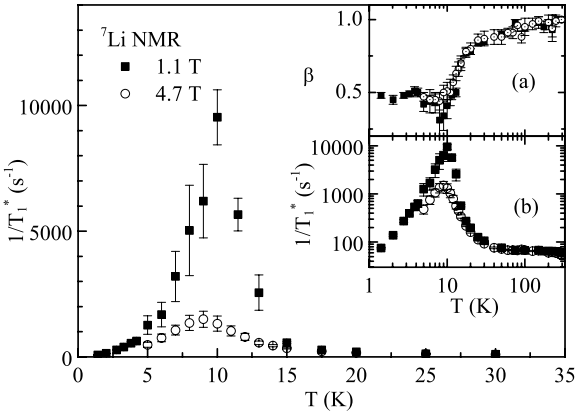

Figure 6.14 ^{7}Li nuclear spin lattice relaxation rates $1/T_1^*$ in Eq. (6.14) versus temperature T at $H = 1.1$ and 4.7 T. Inset (a): exponent β vs T. Inset (b): Log-log plot of $1/T_1^*$ versus T.

arising from the fluctuating electronic spins:[63]

$$\begin{aligned}\frac{1}{T_1} &= \frac{\gamma_{\rm Li}^2}{2}\int_{-\infty}^{\infty}\langle h_x(0)h_x(t)+h_y(0)h_y(t)\rangle\exp(-i\omega_{\rm n}t)\,{\rm d}t \\ &= \frac{1}{2}\gamma_{\rm Li}^2\langle h_x^2+h_y^2\rangle\int_{-\infty}^{\infty}f(t)\exp(-i\omega t){\rm d}t|_{\omega=\omega_{\rm n}} \\ &\equiv \frac{1}{2}\gamma_{\rm Li}^2\langle h_x^2+h_y^2\rangle J(\omega)|_{\omega=\omega_{\rm n}},\end{aligned} \tag{6.15}$$

where $\omega_{\rm n} = \gamma_{\rm Li}H$ is the nuclear Larmor angular frequency, $\langle\cdots\rangle$ denotes a thermal average,

$$f(t) \equiv \frac{\langle h_x(0)h_x(t)\rangle}{\langle h_x^2\rangle} = \frac{\langle h_y(0)h_y(t)\rangle}{\langle h_y^2\rangle}$$

is the reduced correlation function of the local fluctuation field, and $J(\omega)$ is the Fourier transform of $f(t)$. We assume the correlation function $f(t)$ to be isotropic in the x-y plane which is perpendicular to the external field.

As noted in the introduction, the occurrence of a stretched exponential relaxation may indicate the presence of a distribution of $1/T_1$ values. The distribution can arise from an inhomogeneity in the local fluctuating field $\langle h_x^2+h_y^2\rangle$ and/or an inhomogeneity in the dynamics seen by different nuclear spins. As discussed in the introduction, whether or not dynamical inhomogeneity exists in spin glasses is still an unsettled issue. However, based on the following two considerations, we believe that the dynamical inhomogeneity is relevant to explain our NMR results. First, the concentration of vanadium moments in the present system is very

high and most ^{7}Li nuclei are expected to have a few nearest neighbor vanadium moments that dominate their relaxation. As a result, the distribution of the local field is relatively narrow. Second, the value of β decreases continuously with decreasing temperature, which indicates an evolving $1/T_1$ distribution.[36, 38] Similar conclusions were previously reached on the same basis from muon spin depolarization measurements on metallic spin glasses.[21] This is consistent with a temperature dependent distribution of electronic spin relaxation times close to and above the spin glass transition temperature derived from earlier experiments.[17, 22, 23]

Under conditions discussed below, the distribution of electronic spin relaxation times can be derived from the $1/T_1$ distribution of the ^{7}Li spins. Numerical studies suggested that an individual electronic spin autocorrelation function is not a pure exponential.[24, 25] However, in order to make progress we assume an electronic spin autocorrelation function $f(t) = \mathrm{e}^{-|t|/\tau}$ as seen by a particular ^{7}Li nucleus, and then the nuclear spin-lattice relaxation rate of that ^{7}Li nucleus is

$$\frac{1}{T_1} = \gamma_{\mathrm{Li}}^2 \langle h_x^2 + h_y^2 \rangle \frac{\tau}{1 + \omega_n^2 \tau^2}. \tag{6.16}$$

In order to calculate the value of τ from $1/T_1$, the value for $\langle h_x^2 + h_y^2 \rangle$ has to be determined. To compute this value, we will use the spatial average $\overline{\langle h_x^2 + h_y^2 \rangle}$ over all the ^{7}Li nuclear positions and estimate the average with the following simplifying assumptions. First we assume an isotropic superexchange interaction among neighboring vanadium spins. In such a case, the fluctuation of the transverse components of a spin will be modulated by an oscillation with the electronic Larmor frequency and its spectral density at the frequency of the nuclear Larmor frequency is very small.[64] Thus one only needs to consider the local field fluctuation due to the longitudinal components of vanadium spins. Secondly, we ignore possible correlations between the fluctuations of local fields produced by different vanadium local moments. Then[59]

$$\langle h_x^2 + h_y^2 \rangle = \sum_i \frac{3\gamma_{\mathrm{s}}^2 \hbar^2}{r_i^6} \left(\sin^2 \theta_i \cos^2 \theta_i \right) S(S+1), \tag{6.17}$$

where $\hbar$ is Planck's constant divided by 2π, γ_{s} and S are respectively the gyromagnetic ratio and spin $S = 1$ of the vanadium moments, r_i the distance between vanadium moment i and the nuclear spin, and θ_i the angle between $\vec{r}_i$ and the external field. In the numerical calculation, the applied magnetic field direction is arbitrarily chosen to be along the c-axis. The four VL

sites are randomly assigned with either Li or V atoms with the probability for vanadium atoms to be at VL1–4 sites of 0.913, 0.535, 0.460 and 0.501, respectively, as determined from Rietveld refinement. Our numerical calculations then give $(\overline{\langle h_x^2 + h_y^2 \rangle})^{1/2} = 0.15$ T.

Now the distribution of electronic spin relaxation times τ can be calculated by using an algorithm similar to that recently discussed in Ref. [38] in order to extract the distribution of relaxation rate values from a given stretched exponential recovery. In fact, from a given value of β in the stretched exponential function one obtains a unique probability distribution $q(s, \beta)$ of $s = T_1^*/T_1$.[36, 38] According to Eq. (6.16), for $\omega_n \tau < 1$ (i.e., in the high temperature region above the zero field T_g), a given value of $1/T_1$ corresponds to a unique value of τ where we use the above $\overline{\langle h_x^2 + h_y^2 \rangle} = 0.0225$ T^2. The distribution of τ values can be expressed in the limit of $\omega_n \tau \ll 1$ (justified *post hoc* in Fig. 6.15) by

$$p(\tau) = \frac{\tau}{a} q\Big(\frac{\tau}{a}, \beta\Big), \tag{6.18}$$

where $p(\tau)\mathrm{d}\tau/\tau = p(\tau)\mathrm{d}\ln\tau$ is the probability that the relaxation time is between τ and $\tau + \mathrm{d}\tau$ and is normalized according to $\int_{-\infty}^{\infty} p(\tau) d\ln\tau = 1$, $q(s, \beta)$ is normalized according to $\int_0^{\infty} q(s, \beta) ds = 1$, and

$$a = \frac{1}{\gamma_{\mathrm{Li}}^2 \overline{\langle h_x^2 + h_y^2 \rangle} T_1^*}.$$

The determination of the distribution $p(\tau)$ is an important result of the NMR measurements. $p(\tau)$ is plotted in Fig. 6.15 at a few temperatures and at fields $H = 1.1$ and 4.7 T, where the β values at different temperatures are indicated in the figure caption. Because the fraction of ^{7}Li nuclei from which the $p(\tau)$ is determined becomes small as the temperature decreases below 15 K (see Fig. 6.11), the results should only be taken as an order of magnitude estimate. However, the trend of a slowing down and continuous broadening of the distribution is clearly seen as the zero-field spin glass transition temperature is approached from above. Such a temperature dependence is qualitatively similar to distributions derived earlier from ac susceptibility and neutron spin echo measurements.[17, 22, 23] One can see that even at 10 K, there still exists a significant amount of spins with very short correlation times: $\tau \sim 10^{-11}$ s. Such short τ values are in contradiction with the assumption $\gamma H \gg 1/\tau_{\min}$ made in Ref. [28], from which the authors ruled out the dynamic inhomogeneity as an adequate description of

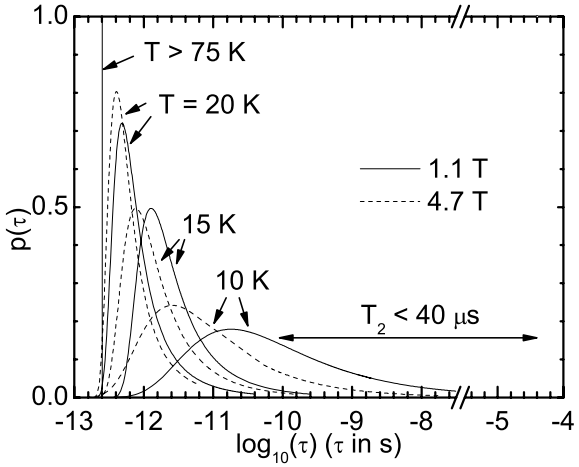

Figure 6.15 Plots of the distribution of electronic correlation times τ extracted from ^{7}Li nuclear spin-lattice relaxation measurements at different temperatures and at fields $H = 1.1$ and 4.7 T. At $H = 1.1$ T, the β values are equal to 1, 0.78, 0.7, and 0.41 at temperatures $T > 75$ K and $T = 20$, 15, and 10 K, respectively. While at $H = 4.7$ T, the β values are equal to 1, 0.8, 0.7, and 0.5 at temperatures $T > 75$ K and $T = 20$, 15, and 10 K, respectively. The range indicated by the double arrowed line corresponds to values of τ which give rise to $T_2 < 40$ μs, for which the ^{7}Li NMR signal is not observable.

the nonexponential spin correlation function. Furthermore, one finds that at higher magnetic field the overall relaxation rate tends to increase.

It is noted that the signal intensity loss (inset of Fig. 6.11) is consistent with the behavior of $p(\tau)$ in Fig. 6.15. In fact, the range indicated by the double arrowed line corresponds to values of τ with $T_2 \leq 40\,\mu$s. An NMR signal from nuclear spins with such short T_2 values cannot be detected because the pulse separation between the two pulses which generate an echo signal is 20 μs. The value of τ above which the NMR signal becomes unobservable is $\tau = 9.0 \times 10^{-11}$ s as estimated from the equation[65] (by setting $T_2 = 40$ μs)

$$\frac{1}{T_2} = \frac{1}{2T_1} + \gamma_{\rm Li}^2 \overline{\langle h_z^2 \rangle} \tau, \tag{6.19}$$

which is valid in the fast motion limit (i.e. $\tau\gamma(\overline{\langle h_z^2 \rangle})^{1/2} \ll 1$) and the contribution to $1/T_2$ from nuclear dipole-dipole interactions is neglected. The contribution from the nuclear dipolar interaction is of the order of 300 μs so the above equation is valid only close to the zero-field

T_g when it yields a T_2 value much smaller than 300 μs. The expression for $\langle h_z^2 \rangle$ is [59]

$$\langle h_z^2 \rangle = \sum_i \frac{\gamma_s^2 \hbar^2}{3 r_i^6} (1 - 3\cos^2\theta_i)^2 S(S+1). \tag{6.20}$$

Its average in Eq. (6.19) is estimated with the same numerical procedure as above and is found to be $(\overline{\langle h_z^2 \rangle})^{1/2} = 0.12$ T. The value of τ above which the signal becomes again observable is $\tau \sim T_2 \sim 40\ \mu\text{s} \gtrsim 1/(\overline{\langle h_z^2 \rangle})^{1/2} \gamma_{\text{Li}}$.[32] In this slow motion regime, T_2 increases with increasing τ up to the limiting value given by the nuclear dipole-dipole interaction and the signal intensity is partially recovered as shown in Fig. 6.11 for the $H = 1.1$ T data.

6.5.5 ^{11}B NMR

Figure 6.16 shows the ^{11}B NMR central $|I_z = -1/2\rangle \leftrightarrow |1/2\rangle$ transition spectra at applied magnetic fields $H = 1.28$ and 4.7 T and $T = 295$ K. The satellites from $|-3/2\rangle \leftrightarrow |-1/2\rangle$ and $|1/2\rangle \leftrightarrow |3/2\rangle$ transitions spread out due to anisotropic frequency shift since the measurements were performed on a powder sample and could not be detected due to limited signal to noise ratio.[59] The spectrum at $H = 1.28$ T shows two peaks corresponding to the two singularities in the powder pattern of a second order quadrupole effect. The two peaks merge into one at $H = 4.7$ T because the separation of the two peaks is inversely proportional to the field. If one assumes an axially symmetric electric field gradient (EFG), then the separation of the two peaks ($\delta\nu$) is[59]

$$\delta\nu = \frac{25\pi}{24} \frac{\nu_Q^2}{H\gamma_{\text{Li}}}, \tag{6.21}$$

where the quadrupole frequency ν_Q is

$$\nu_Q = \frac{3e^2qQ}{h2I(2I-1)} = \frac{1}{2}\frac{e^2qQ}{h},$$

$eq = V_{zz}$ is the electric field gradient along the axial symmetry axis, and Q and I are the quadrupole moment and spin of a ^{11}B nucleus, respectively. At $H = 1.28$ T, $\delta\nu = 44(4)$ kHz, so $\nu_Q = 1.2(1)$ MHz. This value is close to that in crystalline B_2O_3 where $2\nu_Q = 2.69 \pm 0.03$ MHz.[66] In both systems, boron atoms are at the centers of triangles with oxygen atoms at the vertices.

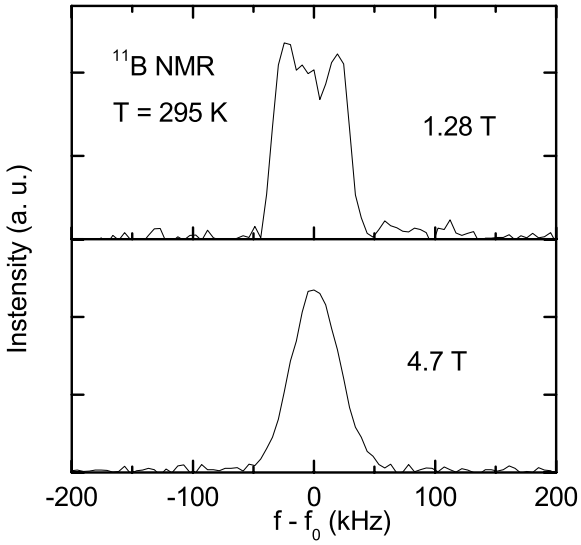

Figure 6.16 Spectra of ^{11}B NMR central transition at $H = 1.28$ and 4.7 T and $T = 295$ K.

Since only the central line for ^{11}B ($I = 3/2$) can be irradiated, the nuclear spin-lattice relaxation is intrinsically nonexponential. For a relaxation due to magnetic interactions, the recovery of the central line follows[67]

$$\begin{aligned} 1 - \frac{M(t)}{M(\infty)} &= C\exp(-2Wt) \\ &+ (1-C)\exp(-12Wt), \end{aligned} \tag{6.22}$$

where C depends on the saturation sequence and the degree of overlap of the satellite background with the central line and W is related to the transition rate $W_{m\to m-1}$ from the $I_z = |m\rangle$ to the $|m-1\rangle$ state through

$$W = \frac{W_{m\to m-1}}{(I-m+1)(I+m)} = \text{const},$$

where $m = \pm 1/2$ or $3/2$ here. At low temperatures, due to the presence of a distribution of electronic spin relaxation times, Eq. (6.22) no longer fits the relaxation curves. We thus used the following phenomenological stretched exponential equation to fit the relaxation curves:

$$\begin{aligned} 1 - \frac{M(t)}{M(\infty)} &= C\exp[-(2W^*t)^\beta] \\ &+ (1-C)\exp[-(12W^*t)^\beta]. \end{aligned} \tag{6.23}$$

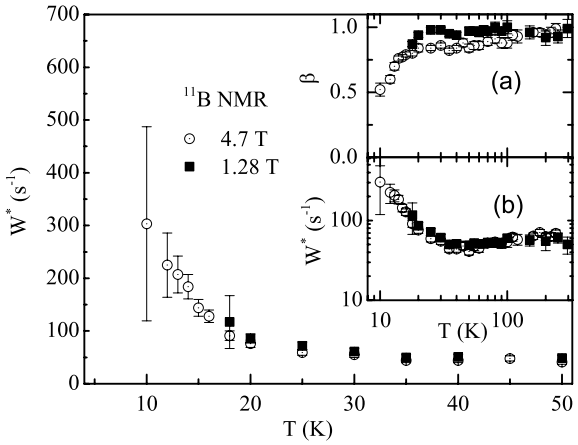

Figure 6.17 W^* and β in Eq. (6.23) vs temperature T for ^{11}B NSLR at fields $H = 1.28$ and 4.7 T. Main panel and inset (b): W^* versus T with different temperature scales. Inset (a): β versus T.

The saturation sequence we used consisted of nine $\pi/2$ pulses with a separation of 400 μs between neighboring pulses. The value of C is found to be in the range 0.3–0.4 at $H = 4.7$ T and in the range 0.5–0.6 at $H = 1.28$ T. The difference of the C values at the two fields is currently not understood.

The fitting results of W^* and β versus T at $H = 1.28$ and 4.7 T are displayed in Fig. 6.17. The data displayed are only for $T \geq 10$ K at $H = 4.7$ T and $T \geq 18$ K at $H = 1.28$ T. Due to a loss of signal intensity (similar to ^{7}Li in the main panel of Fig. 6.11) and a large increase of relaxation rate, reliable W^* and β results cannot be obtained at lower temperatures. However, it is clear that ^{11}B NMR nuclear spin-lattice relaxation rates are also strongly enhanced at low temperature, in qualitative agreement with the slowing down of the spin fluctuations on approaching the zero-field spin glass transition temperature.

6.6 Summary and Conclusions

X-ray diffraction studies on both single crystal and polycrystalline samples confirmed the previously reported structure of the $(Li_xV_{1-x})_3BO_5$ system. The structure contains both frustration and disorder, which are usually considered as necessary ingredients of a spin glass system.

The high temperature magnetic susceptibility results cannot be explained by the simple picture of formation of VL1–VL4–VL1 linear trimers proposed in Ref. [30]. The observed negative curvature in the inverse susceptibility below $T \approx 100$ K might instead be due to the occurrence of magnetic clusters as the spin glass transition temperature is approached. Magnetization measurements at low temperatures showed field-cooled and zero-field-cooled splitting of magnetization, slow relaxation of magnetization on a macroscopic time scale, and memory and rejuvenation effects which are all evidences of a spin glass state below $T_{\rm g} \sim 10$ K.

The strong enhancement of nuclear spin-lattice relaxation rates upon approaching the zero-field $T_{\rm g}$ suggests that the dramatic slowing down of electronic spin dynamics persists even in a high field of 4.7 T where a true long range spin glass transition may be suppressed as indicated by the magnetization measurements (Fig. 6.5). Our NMR measurements cannot distinguish whether the spin system is in thermodynamic equilibrium or not at a particular temperature. In addition, we have no information on whether the spins freeze on a time scale longer than that of NMR ($\sim 10^{-6}$ s).

We extracted the distribution of electronic spin relaxation times τ from NMR. A derived broad distribution of τ starts well above the zero-field spin glass transition temperature $T_{\rm g}$ and becomes successively broader as the zero-field $T_{\rm g}$ is approached. The broad distribution of τ explains the observed loss of signal intensities displayed in the inset of Fig. 6.11. As illustrated in Fig. 6.15, as the temperature decreases toward $T_{\rm g}$, more and more vanadium spins have τ in the range of $\sim 10^{-10}$–10^{-6} s, which results in $T_2 \lesssim 40\,\mu$s for the nearby ^{7}Li nuclear spins. Our modeling in terms of dynamical electronic spin heterogeneity[17, 21–25] offers an alternative framework to models of homogeneous electronic relaxation.[18, 28]

Acknowledgements

We would like to thank B. J. Suh for helpful discussions. We also acknowledge A. Ellern in the molecular structure laboratory of Iowa State University for determining the structure of the single crystals through x-ray diffraction study. Work at the Ames Laboratory was supported by the Department of Energy-Basic Energy Sciences under Contract No. DE-AC02-07CH11358.

References

[1] X. Zong, A. Niazi, F. Borsa, X. Ma, and D. C. Johnston, Phys. Rev. B **76**, 054452 (2007).

[2] T. Nakamura and S. Endoh, J. Phys. Soc. Jpn. **71**, 2113 (2002).

[3] F. Matsubara, T. Shirakura, S. Endoh, and S. Takahashi, J. Phys. A **36**, 10881 (2003).

[4] K. Hukushima and H. Kawamura, Phys. Rev. B **72**, 144416 (2005).

[5] L. W. Lee and A. P. Young, Phys. Rev. B **76**, 024405 (2007).

[6] I. Campos, M. Cotallo-Aban, V. Martin-Mayor, S. Perez-Gaviro, and A. Tarancon, Phys. Rev. Lett. **97**, 217204 (2006).

[7] I. A. Campbell and H. Kawamura, Phys. Rev. Lett. **99**, 019701 (2007).

[8] D. S. Fisher and D. A. Huse, Phys. Rev. B **38**, 386 (1988).

[9] G. Parisi, Phys. Rev. Lett. **43**, 1754 (1979).

[10] J. Mattsson, T. Jönsson, P. Nordblad, H. Aruga Katori, and A. Ito, Phys. Rev. Lett. **74**, 4305 (1995).

[11] P. E. Jönsson, H. Takayama, H. A. Katori, and A. Ito, Phys. Rev. B **71**, 180412 (2005).

[12] P. E. Jönsson and H. Takayama, J. Phys. Soc. Jpn. **74**, 1131 (2005).

[13] G. G. Kenning, D. Chu, and R. Orbach, Phys. Rev. Lett. **66**, 2923 (1991).

[14] D. Chu, G. G. Kenning, and R. Orbach, Phys. Rev. Lett. **72**, 3270 (1994).

[15] D. Petit, L. Fruchter, and I. A. Campbell, Phys. Rev. Lett. **83**, 5130 (1999).

[16] D. Petit, L. Fruchter, and I. A. Campbell, Phys. Rev. Lett. **88**, 207206 (2002).

[17] A. P. Murani, J. Magn. Magn. Mater. **22**, 271 (1981).

[18] C. Pappas, F. Mezei, G. Ehlers, P. Manuel, and I. A. Campbell, Phys. Rev. B **68**, 054431 (2003).

[19] A. T. Ogielski, Phys. Rev. B **32**, 7384 (1985).

[20] K. Gunnarsson, P. Svedlindh, P. Nordblad, L. Lundgren, H. Aruga, and A. Ito, Phys. Rev. Lett. **61**, 754 (1988).

[21] I. A. Campbell, A. Amoto, F. N. Gygax, D. Herlach, A. Schenck, R. Cywinski, and S. H. Kilcoyne, Phys. Rev. Lett. **72**, 1291 (1994).

[22] L. Lundgren, P. Svedlindh, and O. Beckman, J. Magn. Magn. Mater. **25**, 33 (1981).

[23] L. E. Wenger, Lecture Notes in Physics **192**, 60 (1983).

[24] H. Takano and S. Miyashita, J. Phys. Soc. Jpn. **64**, 423 (1995).

[25] S. C. Glotzer, N. Jan, T. Lookman, A. B. MacIsaac, and P. H. Poole, Phys. Rev. E **57**, 7350 (1998).

[26] P. H. Poole, S. C. Glotzer, A. Coniglio, and N. Jan, Phys. Rev. Lett. **78**, 3394 (1997).

[27] C. Brangian, W. Kob, and K. Binder, J. Phys. A: Math. Gen. **35**, 191 (2002).

[28] A. Keren, G. Bazalitsky, I. Campbell, and J. S. Lord, Phys. Rev. B **64**, 054403 (2001).

[29] R. G. Palmer, D. L. Stein, E. Abrahams, and P. W. Anderson, Phys. Rev. Lett. **53**, 958 (1984).

[30] M. Onoda, J. Solid State Chem. **141**, 418 (1998).

[31] D. E. MacLaughlin and H. Alloul, Phys. Rev. Lett. **36**, 1158 (1976).

[32] D. E. MacLaughlin and H. Alloul, Phys. Rev. Lett. **38**, 181 (1977).

[33] D. A. Levitt and R. E. Walstedt, Phys. Rev. Lett. **38**, 178 (1977).

[34] D. Bloyet, E. Varoquaux, C. Vibet, O. Avenel, and M. P. Berglund, Phys. Rev. Lett. **40**, 250 (1978).

[35] M. C. Chen and C. P. Slichter, Phys. Rev. B **27**, 278 (1983).

[36] D. C. Johnston, S.-H. Baek, X. Zong, F. Borsa, J. Schmalian, and S. Kondo, Phys. Rev. Lett. **95**, 176408 (2005).

[37] J. Merrin, Y. Fudamoto, K. M. Kojima, M. Larkin, G. M. Luke, B. Nachumi, Y. J. Uemura, S. Kondo, and D. C. Johnston, J. Magn. Magn. Mater. **177–181**, 799 (1998).

[38] D. C. Johnston, Phys. Rev. B **74**, 184430 (2006).

[39] S. Kondo, D. C. Johnston, and L. L. Miller, Phys. Rev. B **59**, 2609 (1999).

[40] B. H. Toby, J. Appl. Cryst. **34**, 210 (2001).

[41] A. C. Larson and R. B. Von Dreele, Los Alamos National Laboratory Report No. LAUR 86-748, 2004 (unpublished).

[42] J. B. Goodenough, *Magnetism and the Chemical Bond* (Interscience Publishers, New York-London, 1963).

[43] J. B. Goodenough, Phys. Rev. **117**, 1442 (1960).

[44] R. Omari, J. J. Prejean, and J. Souletie, J. Phys. (Paris) **44**, 1069 (1983).

[45] P. W. Selwood, *Magnetochemistry* (Interscience, New York, 1956), 2nd ed.

[46] B. Southern, J. Phys. C: Solid State Phys. **8**, L213 (1975).

[47] M. M. Zaripov, V. S. Kropotov, L. D. Livanova, and V. G. Stepanov, Dokl. Akad. Nauk SSSR **173**, 1043 (1967).

[48] D. C. Johnston, T. Saito, M. Azuma, M. Takano, T. Yamauchi, and Y. Ueda, Phys. Rev. B **64**, 134403 (2001).

[49] Y. Ueda, J. Kikuchi, and H. Yasuoka, J. Magn. Magn. Mater. **147**, 195 (1995).

[50] A. P. Ramirez, Annu. Rev. Mater. Sci. **24**, 453 (1994).

[51] G. Griffith, F. A. Volkening, and H. Claus, J. Appl. Phys. **57**, 3392 (1985).

[52] K. Binder and A. P. Young, Rev. Mod. Phys. **58**, 801 (1986).

[53] J. Ferré, M. Ayadi, R. V. Chamberln, R. Orbach, and N. Bontemps, J. Magn. Magn. Mater. **54-57**, 211 (1986).

[54] R. V. Chamberlin, G. Mozurkewich, and R. Orbach, Phys. Rev. Lett. **52**, 867 (1984).

[55] Y. Sun, M. B. Salamon, K. Garnier, and R. S. Averback, Phys. Rev. Lett. **91**, 167206 (2003).

[56] F. Lefloch, J. Hammann, M. Ocio, and E. Vincent, Europhys. Lett. **18**, 647 (1992).

[57] M. Sasaki, P. E. Jönsson, H. Takayama, and P. Nordblad, Phys. Rev. Lett. **93**, 139701 (2004).

[58] E. Fukushima and S. B. W. Roeder, *Experimental Pulse NMR: A Nuts and Bolts Approach* (Perseus Books, Cambridge, 1981).

[59] A. Abragam, *Principles of Nuclear Magnetism* (Oxford University Press, Oxford, 1982).

[60] J. A. Ibers, C. H. Holm, and C. R. Adams, Phys. Rev. **121**, 1620 (1961).

[61] H. M. McConnell and R. E. Robertson, J. Chem. Phys. **29**, 1361 (1958).

[62] M. Belesi, A. Lascialfari, D. Procissi, Z. H. Jang, and F. Borsa, Phys. Rev. B **72**, 014440 (2005).

[63] T. Moriya, Prog. Theor. Phys. **16**, 23 (1956).

[64] F. Borsa and A. Rigamonti, in *Magnetic Resonance of Phase Transitions*, edited by F. J. Owens, C. P. Poole, and H. A. Farach (Academic Press, New York, 1979), p. 103.

[65] C. P. Slichter, *Principles of Magnetic Resonance* (Springer, Berlin, 1990), 3rd ed.

[66] C. Rhee and P. J. Bray, J. Chem. Phys. **56**, 2476 (1972).

[67] E. R. Andrew and D. P. Tunstall, Proc. Phys. Soc. London **78**, 1 (1961).

CHAPTER 7. Summary

In conclusion, we have presented NMR studies on spin dynamics and spin structure on three different strongly correlated vanadium oxide compounds LiV_2O_4, $(Li_xV_{1-x})_3BO_5$, and CaV_2O_4. In the rare d-electron heavy fermion LiV_2O_4, we found that ^{7}Li NMR properties are sensitive to the presence of a small amount of magnetic defects within its spinel crystal structure. In order to understand the nature of the LiV_2O_4 samples with magnetic defects, we carried out a systematic ^{7}Li NMR study on LiV_2O_4 powder and single crystal samples with different concentrations of magnetic defects. Our measurements show that there are different kinds of magnetic defects in the system. The magnetic defects in the powder samples undergo a spin glass freezing below 1 K while those in the single crystals remain paramagnetic down to the lowest measurement temperature 0.5 K. Our NMR results can be well explained by treating the magnetic defects as dilute paramagnetic centers and assuming that the heavy fermion carriers are preserved in the presence of the magnetic defects. The finding that heavy fermion carriers survive in the presence of magnetic defects may constrain further theoretical developments in understanding the origin of the intrinsic heavy fermion properties in LiV_2O_4.

In the zig-zag spin-1 chain system CaV_2O_4, we used ^{17}O and ^{51}V NMR to study the magnetic phase transition and low temperature spin structure and spin wave properties in the system. ^{17}O NMR together with complementary magnetic susceptibility measurements gave clear evidence for an antiferromagnetic phase transition at $T = 78$ K in the powder samples. ^{51}V NMR spectrum study on the crystals in the ordered state revealed the presence of two antiferromagnetic spin substructures. Each substructure is collinear, with the easy axes of the two substructures separated by an angle of 19 degrees, and with their average direction pointing approximately along the b-axis of the crystal structure, consistent with our group's anisotropic

magnetic susceptibility measurements on single crystals. The temperature dependence of the ordered moments shows the presence of an energy gap in the antiferromagnetic spin wave excitation spectrum with the gap value lying between 64 and 98 K. The low temperature ordered moment is estimated from the value of local field at the ^{51}V nuclear spin to be 1.63 ± 0.33 μ_B/V atom.

In the insulating spin glass $(Li_xV_{1-x})_3BO_5$, we established the presence of a spin glass state below ~ 10 K in this material through magnetization measurements. The apparent spin freezing temperature is shifted to lower temperatures at higher fields from magnetization measurements. However, the NMR measurements in a strong applied magnetic field up to 4.7 T show the persistence of dramatic slowing down of the spin dynamics at an almost field independent temperature, that is about the same as the zero field spin-glass transition temperature. The difference between magnetization and NMR results suggests that a sharp dynamical slowing down still occurs even if a true thermodynamic phase transition is suppressed by the applied field. Our results also suggest that NMR can be used as a sensitive way to detect the spin glass freezing despite the requirement for the presence of a large applied magnetic field. Furthermore, we observed a stretched exponential nuclear spin-lattice relaxation on approaching the zero-field spin glass transition temperature, similar to the nuclear spin-lattice relaxation behavior in LiV_2O_4 samples with magnetic defects. We modeled the stretched exponential relaxation as dominated by the electronic spin dynamical heterogeneity. The distribution of correlation times derived under such an assumption is found to be consistent with the observed loss of NMR signal intensity close to the zero-field spin glass transition temperature.

APPENDIX. ^{11}B NMR in the Layered Diborides OsB_2 and RuB_2

(This appendix is based on a paper published in Phys. Rev. B by B. J. Suh, X. Zong, Y. Singh, A. Niazi, and D. C. Johnston[1])

Abstract

^{11}B nuclear magnetic resonance (NMR) measurements have been performed on ^{11}B enriched OsB_2 and RuB_2 polycrystalline powder samples in an external field of 4.7 T and in the temperature range 4.2 K $< T <$ 300 K. The spectra for both samples show similar quadrupole powder patterns that are typical for a non-axial symmetry. The Knight shifts K in both samples are very small and constant in temperature. The nuclear spin-lattice relaxation rate T_1^{-1} follows a Korringa law in the whole temperature range investigated with $T_1T = 600$ and 680 s K for OsB_2 and RuB_2, respectively. The experimental results indicate that a p character dominates the conduction electron wave function at the B site with a negligibly small s character in both compounds.

Introduction

Right after the discovery of superconductivity in MgB_2 at a high temperature $T_c = 39$ K,[2] a number of subsequent experiments,[3, 4] in particular, isotope effects measurements[5, 6] confirmed that MgB_2 belongs to the conventional BCS superconductor. Theoretical studies using band structure calculations also found that in MgB_2, the Fermi level (E_F) is located at the shoulder of the density of states (DOS) curve in which B $2p$ states are dominant.[7–9] It seems to be generally accepted that the B $2p$ band plays a crucial role for the high T_c in MgB_2. On the other hand, many structurally-related metal diborides TB_2 (T = Ti, Zr, Hf, V, Cr, Nb,

Ta, Mo) have been studied,[10–14] some of which had already been studied in the past,[15] but the role of the B $2p$ band for the superconductivity in other metal diborides $T\mathrm{B}_2$ is not clearly understood yet.

There is also an interesting metal-diboride family, OsB_2 and RuB_2, which crystallize in an orthorhombic structure ($Pmmn$) containing deformed boron sheets instead of a planar boron array as in the hexagonal MgB_2. They have been known to be superconductors with $T_\mathrm{c} = 2.1$ K for OsB_2 and 1.6 K for RuB_2 since 1975,[16] but other physical properties besides T_c have not been reported until the recent studies related to their unusually high bulk modulus.[17–19]

Note that the difference between T_c's for two compounds, $\delta T_\mathrm{c} = 0.5$ K, which is 24 % of $T_\mathrm{c} = 2.1$ K of OsB_2, is sufficiently large but no noticeable difference between the properties related to the superconductivity has been reported yet. OsB_2 and RuB_2 are isostructural, where the difference between the lattice constants is less than 1 %.[20, 21] Band structure calculations suggest that the relevant DOS's at the Fermi level are even identical for both compounds as summarized in Table A.1.[18] From a recent comprehensive study by some of us, no considerable difference between their thermodynamic properties was observed except for the Debye temperatures, $\Theta_\mathrm{D} = 550$ K for OsB_2 and $\Theta_\mathrm{D} = 701$ K for RuB_2, which are consistent with their relative molar masses but are not helpful to explain the higher T_c in OsB_2.[21]

Nuclear magnetic resonance (NMR) is a microscopic tool to investigate the electronic struc-

Table A.1 Summary of various information on OsB_2 and RuB_2. The densities of states N at the Fermi level (E_F) are theoretically calculated values in units of states/(eV f.u.) for the total $N(E_\mathrm{F})$ (both spin directions) and of states/(eV B atom) for the partial s- and p-type densities of states, respectively, where "f.u." means formula unit.

	OsB_2	RuB_2	Reference
T_c (K)	2.1	1.6	[16], [21]
Θ_D (K)	550	701	[21]
$N(E_\mathrm{F})$	0.551	0.548	[18]
$N_{\mathrm{B}s}(E_\mathrm{F})$	0.007	0.006	[18]
$N_{\mathrm{B}p}(E_\mathrm{F})$	0.098	0.097	[18]

ture in a nonmagnetic metal. The NMR parameters, the Knight shift (K) and the nuclear spin-lattice relaxation rate (T_1^{-1}) are related to the partial DOS's at the site of probing nuclei. As demonstrated from a number of ^{11}B NMR studies in MgB_2 and related materials, ^{11}B NMR is a suitable probe of the B s and/or B p states selectively in metal diborides.[22–25] We have applied ^{11}B NMR to investigate the structural and electronic properties of OsB_2 and RuB_2. The experimental results for the spectra, Knight shifts, and relaxation rates in the two compounds have been compared and discussed in relation to the local structure or to the partial DOS's at the B site.

Experimental

^{11}B enriched polycrystalline samples of OsB_2 and RuB_2 were prepared by arc-melting using ultrahigh purity Os (99.995 %, Sigma Aldrich), Ru (99.995 %, MV labs), and ^{11}B (99.999 %, Eagle Pitcher). Details for the preparation, and the structural and thermodynamic properties of OsB_2 and RuB_2 are described elsewhere.[21] ^{11}B (nuclear spin $I = 3/2$) NMR and relaxation measurements were carried out on the powdered samples with a standard Fourier transform (FT) pulse NMR spectrometer in the temperature range 4.2 K $< T <$ 294 K and in an external magnetic field $H = 4.7$ T corresponding to the Larmor frequency $\nu_{\rm L} = 64.17837$ MHz for ^{11}B in a $NaBH_4$ aqueous solution. The $\pi/2$ radio frequency (rf) pulse length was typically 2.4 μs. The ^{11}B spectrum was obtained from the Fourier transform of half of the echo following a $(\pi/2)_0 - (\pi/2)_{90}$ pulse sequence. In order to cover the whole spectrum, separate spectra were recorded at every 100 kHz in the frequency range $-400 \leq \nu - \nu_{\rm L} \leq 400$ kHz and added together. The ^{11}B T_1^{-1} was measured by monitoring the recovery of the nuclear magnetization following a long sequence of saturating rf pulses. Following this sequence, the entire spectrum becomes saturated, and the recovery of the nuclear magnetization was observed to be exponential in the whole temperature investigated.

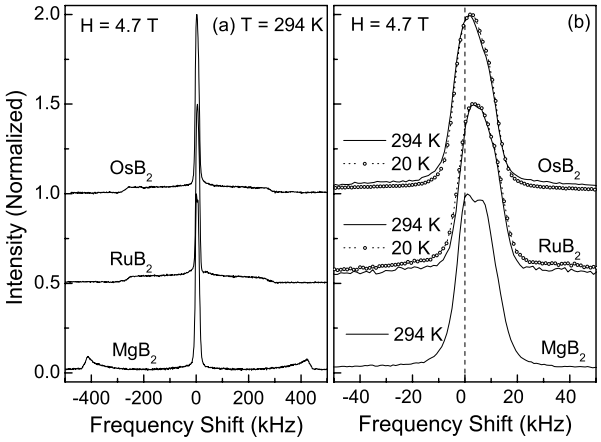

Figure A.1 ^{11}B ($I = 3/2$) NMR spectra in ^{11}B enriched OsB_2 and RuB_2 powder samples at $H = 4.7$ T corresponding to $\nu_L = 64.17837$ MHz: (a) The whole spectra at room temperature and (b) the central line transition at two representative temperatures. The spectrum for MgB_2 is also plotted for comparison.[26]

Results and Discussion

Figure A.1 shows representative spectra for OsB_2 and RuB_2, consisting of a central line and a broad background with steps at $\nu - \nu_L \approx \pm 285$ kHz. The spectra for both compounds are quite similar to each other except for the small relative shift of the central line transition, which will be discussed later. Since the background is of quadrupolar origin and, hence, sensitive to the local symmetry including the local charge distribution at the site of probing nuclei, the observation of nearly identical spectra for both compounds is consistent with their isostructural nature.

On the other hand, the spectra [see the enlarged plots in Fig. A.2(a)] are quite different from the one for hexagonal MgB_2 that shows two singularities of the distribution of satellite transitions typical for $I = 3/2$ with an uniaxial symmetry.[26, 27] The rounded quadrupolar background indicates that the local symmetry at the B site in OsB_2 and RuB_2 is far from being uniaxial,[27] reflecting the low point symmetry (the m symmetry with a mirror in the ac-plane)

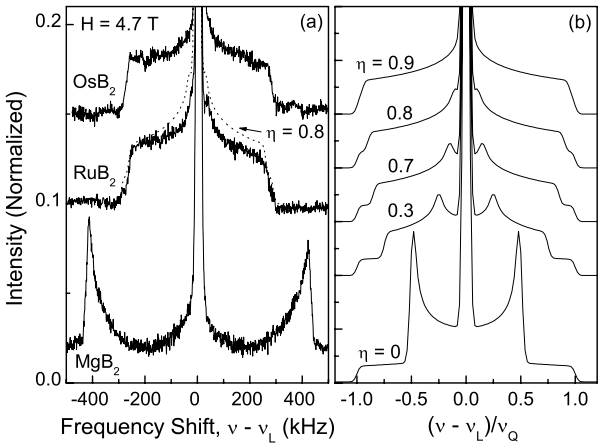

Figure A.2 Comparison of the ^{11}B ($I = 3/2$) NMR spectra in OsB_2 and RuB_2 with theoretical simulations: (a) The experimental results and (b) the theoretical simulations for $I = 3/2$ and several representative values of the asymmetry parameter η with a line broadening $\delta\nu/\nu_Q = 0.03$. Data for MgB_2 are shown in (a) for comparison.

of the B sites which occupy the $4f$ Wyckoff sites in the orthorhombic lattice ($Pmmn$).[19] Compared with theoretical simulations of the NMR spectrum for $I = 3/2$ with a non-axial symmetry as shown in Fig. A.2(b), the observed spectra for both compounds correspond to the ones with the asymmetry parameter $\eta \equiv |V_{xx} - V_{yy}|/|V_{zz}| = 0.8 - 0.9$. Moreover, for such a large value of η, the rounded edge of the quadrupolar background roughly corresponds to the quadupole frequency $\nu_{\rm Q}$ as can be seen from the simulations in Fig 2(b). Thus, we estimate $\nu_{\rm Q} = 285 \pm 10$ kHz for both compounds, which is much smaller than $\nu_{\rm Q} = 835$ kHz for MgB_2.

As shown separately in Fig. A.1(b), the central line transition is observed to be asymmetric and quite broad with a linewidth $\delta\nu \simeq 14$ kHz (FWHM; full width at half maximum) and to be constant in temperature for both OsB_2 and RuB_2. In the presence of the second order quadrupole effects, the separation between the two singularities in the central line is given by[27]

$$\Delta\nu = \frac{\nu_Q^2}{48\nu_L}\left[I(I+1) - \frac{3}{4}\right](\eta^2 + 22\eta + 25)\,. \tag{A.1}$$

.

Using $I = 3/2$, $\nu_L = 64.17837$ MHz, $\nu_Q \simeq 285$ kHz, and $\eta \approx 0.9$, we obtain $\Delta\nu \approx 1.2$ kHz, which is too small to explain the observed linewidth, $\delta\nu \simeq 14$ kHz. Such a broad central line cannot be explained by the quadrupole effects. As compared in Fig. A.1(b), the anomalously broad line (with a split structure) has also been observed in MgB_2[22, 25, 26] and explained excellently by dipolar doublets from systematic measurements at various external fields.[25] From the calculation of the second moment $< \Delta\omega^2 >$ for the ^{11}B enriched OsB_2 using the lattice parameters in Ref. [20], we obtained $< \Delta\omega^2 > \simeq 1800$ [rad^2 kHz^2], which corresponds to $\Delta\nu \simeq 15$ kHz for a Gaussian line shape. Thus we conclude that the broad and temperature-independent linewidth in OsB_2 and RuB_2 is also dominated by the dipole-dipole interaction between ^{11}B nuclei similarly to the MgB_2 case. The rather rounded and asymmetric shape of the central line without the split structure seems to be related to the anisotropic dipole interaction and/or to the non-axial symmetry in OsB_2 and RuB_2. We note that the dipolar interaction is very sensitive to the B-B distance, d, between the nearest neighbors.[25] Therefore, the observation of the nearly identical linewidth, which implies that d in both compounds is qualitatively similar to each other, is also consistent with their isostructural nature.

Since the central line is asymmetric, the position of the center of gravity $\nu_{\rm cg}$ instead of the peak position was used to determine the Knight shift K. Thus, the K values obtained here represent the isotropic Knight shift. From the central part with the intensity (normalized with respect to the maximum value) higher than 0.05 which is chosen to exclude the background contribution, we obtain $\nu_{\rm cg} - \nu_{\rm L} \approx 3$ kHz and ≈ 5 kHz, yielding $K \equiv (\nu_{\rm cg} - \nu_{\rm L})/\nu_{\rm L} \approx 50$ ppm for OsB_2 and $K \approx 80$ ppm for RuB_2 with respect to a $NaBH_4$ aqueous solution. If the Knight shift is referred to the BF_3 solution that is used as the "zero chemical shift",[28] we obtain $K \approx 10$ ppm for OsB_2 and $K \approx 40$ ppm for RuB_2. The small and temperature-independent K indicates that the s-component of the wave function at the B site at the Fermi level is negligibly small in both compounds,[27] which is in good agreement with the theoretical calculations

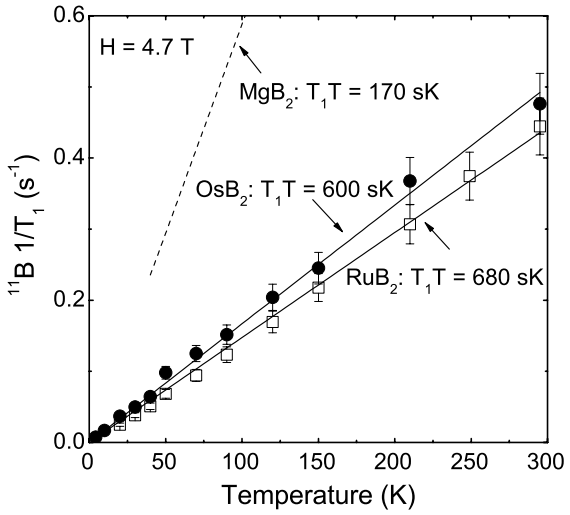

Figure A.3 Temperature dependence of the ^{11}B nuclear spin-lattice relaxation rate T_1^{-1} in OsB_2 and RuB_2 powder samples. The solid lines are fits to the Korringa relation T_1T = Constant. The dashed line represents the results for MgB_2 from Ref. [25].

summarized in Table A.1[18] and similar to the situation of MgB_2.[24, 25]

We turn now to the behavior of the ^{11}B nuclear spin-lattice relaxation rate, T_1^{-1}. As mentioned earlier, with a sufficiently long sequence of saturating rf pulses, the recovery of the nuclear magnetization was observed to be exponential. This is ascribed to the relatively narrow quadrupolar background in OsB_2 and RuB_2. The experimental results of ^{11}B T_1^{-1} obtained by fitting the recovery data to a single exponential function are shown in Fig. A.3. The ^{11}B T_1^{-1} follows a linear temperature dependence, the so-called Korringa law, with $T_1T = 600 \pm 30$ sK for OsB_2 and 680 ± 35 sK for RuB_2 in the whole temperature range investigated. Using the values for the isotropic Knight shift K and the value $S = 2.57 \times 10^{-6}$ sK for ^{11}B [$S \equiv (\gamma_e/\gamma_n)^2(h/8\pi^2k_B)$, and γ_e and γ_n are the gyromagnetic ratios for electron and nucleus, respectively], we obtain the Korringa ratio, $R \equiv K^2T_1T/S \approx 0.02$ and ≈ 0.4 for OsB_2 and for RuB_2, respectively. Note that the Korringa ratio for both compounds is much smaller than the ideal value of unity for the case where the contact interaction with s electrons causes both K and T_1^{-1}.[27] This indicates that the T_1^{-1} is partially driven by a mechanism different from

Table A.2 Summary of the experimental ^{11}B NMR parameters for OsB_2 and RuB_2. The results for MgB_2 from Ref. [25] are presented for comparison.

	OsB_2	RuB_2	MgB_2 [25]
ν_Q (kHz)	285(10)	285(10)	835
K (ppm)*	≈ 10	≈ 40	40
T_1T (sK)	600(30)	680(35)	170
R	≈ 0.02	≈ 0.4	0.102

scattering with s-type conduction electrons at the Fermi level, such as the orbital contribution from the p electrons. This orbital contribution is expected to be roughly proportional to the density of p states at the Fermi level and to temperature. On the other hand, this orbital contribution is quenched for the isotropic Knight shift and does not obey the Korringa ratio. In fact, from band structure calculations, $N_{\mathrm{B}p}(E_{\mathrm{F}}) \approx 0.1$ states/(eV B atom) is obtained to be much larger than $N_{\mathrm{B}s}(E_{\mathrm{F}}) \approx 0.01$ states/(eV B atom) for both compounds (see Table A.1),[18] in qualitative agreement with our observations.

Finally, we note that the Korringa ratio R and the values of T_1T are observed to be clearly different in the two compounds. Although the partial DOS's, $N_{\mathrm{B}p}$ and $N_{\mathrm{B}s}$, were reported to be almost the same for both compounds on the basis of band structure calculations,[18] our observation indicates that there exists a noticeable difference between the partial DOS's in the two compounds, whereby $N_{\mathrm{B}p}$ is considerably larger in OsB_2 than in RuB_2. The B p-band contribution to the DOS at the Fermi level is believed to be the key for the superconductivity in MgB_2[7–9] and to be relevant to the superconductivity even in other metal diborides TB_2.[13, 14] In this scenario, the larger B p-band contribution is expected for the higher T_{c} in OsB_2 as we observed here from ^{11}B NMR relaxation measurements.

Conclusions

We have presented a complete set of ^{11}B NMR data in the layered diborides OsB_2 and RuB_2 and representative results are summarized in Table A.2. All the experimental results have been understood qualitatively in relation to the local structure or to the partial DOS's.

*Corrected with respect to the reference solution BF_3 as described in text.

We find that, at the B site, the p character is dominant for the DOS at the Fermi level for both compounds similarly to the MgB_2 case. A noticeable difference between the Korringa ratio R for the two compounds has been observed, which seems to be relevant to the different T_c's for two compounds. In discussion about the mechanism of the ^{11}B T_1^{-1}, the contribution of the fluctuating dipolar field from the B p character at the Fermi surface is overlooked due to the lack of theoretical support.[24, 25] In order to understand better the microscopic origin of the difference between the NMR parameters in the two compounds and its relevance to the superconductivity, a comparison of our experimental results with *ab initio* calculated values for Knight shifts and relaxations is highly desirable.[24, 25]

Acknowledgements

We thank the authors of Ref. [18] for sharing their band structure calculation data. Work at the Ames Laboratory was supported by the Department of Energy-Basic Energy Sciences under Contract No. DE-AC02-07CH11358.

References

[1] B. J. Suh, X. Zong, Y. Singh, A. Niazi, and D. C. Johnston, Phys. Rev. B **76**, 144511 (2007).

[2] J. Nagamatsu, N. Nakagawa, T. Muranaka, Y. Zenitani, and Akimitsu, Nature (London) **410**, 63 (2001).

[3] T. Takahashi, T. Sato, S. Souma, T. Muranaka, and J. Akimitsu, Phys. Rev. Lett. **86**, 4915 (2001).

[4] G. Rubio-Bollinger, H. Suderow, and S. Vieira, Phys. Rev. Lett. **86**, 5582 (2001).

[5] S. L. Bud'ko, G. Lapertot, C. Petrovic, C. E. Cunningham, N. Anderson, and P. C. Canfield, Phys. Rev. Lett. **86**, 1877 (2001).

[6] D. G. Hinks, H. Claus, and J. D. Jorgenson, Nature (London) **411**, 457 (2001).

[7] J. M. An and W. E. Pickett, Phys. Rev. Lett. **86**, 4366 (2001).

[8] J. Kortus, I. I. Mazin, K. D. Belashchenko, V. P. Antropov, and L. L. Boyer, Phys. Rev. Lett. **86**, 4656 (2001).

[9] N. I. Medvedeva, A. L. Ivanovskii, J. E. Medvedeva, and A. J. Freeman, Phys. Rev. B **64**, 020502(R) (2001).

[10] D. Kaczorowski, A. J. Zaleski, O. J. Zogal, and Klamut, cond-mat/0103571.

[11] V. A. Gasparov, N. S. Sidorov, I. I. Zverkova, and M. P. Kulakov, JETP Lett. **73**, 532 (2001).

[12] H. Rosner, W. E. Pickett, S.-L. Drechsler, A. Handstein, G. Behr, G. Fuchs, K. Nenkov, K.-H. Muller, and H. Eschrig, Phys. Rev. B **64**, 144516 (2001).

[13] J. Nakamura, N. Yamada, K. Kuroki, T. A. Callcott, D. L. Ederer, J. D. Denlinger, and R. C. C. Perera, Phys. Rev. B **64**, 174504 (2001).

[14] I. R. Shein and A. L. Ivanovskii, cond-mat/0109445.

[15] A. N. Cooper, E. Corenzwit, L. D. Longinotti, B. T. Mattias, and W. H. Zachariasen, Proc. Nat. Acad. Sci. USA **67**, 313 (1970).

[16] J. M. Vandenberg, B. T. Matthias, E. Corenzwit, and H. Barz, Mater. Res. Bull. **10**, 889 (1975).

[17] R. W. Cumberland, M. B. Weinberger, J. J. Gilman, S. M. Clark, S. H. Tolbert, and R. B. Kaner, J. Am. Chem. Soc. **127**, 7264 (2005).

[18] S. Chiodo, H. J. Gotsis, N. Russo, and E. Sicilia, Chem. Phys. Lett. **425**, 311 (2006).

[19] Z. Y. Chen, H. J. Xiang, J. Yang, J. G. Hou, and Q. Zhu, Phys. Rev. B **74**, 012102 (2006).

[20] R. B. Roof Jr. and C. P. Kempter, J. Chem. Phys. **37**, 1473 (1962).

[21] Y. Singh, A. Niazi, M. W. Vannette, R. Prozorov, and D. C. Johnston, cond-mat/0612605.

[22] J. K. Jung, S. H. Baek, F. Borsa, S. L. Bud'ko, G. Lapertot, and P. C. Canfield, Phys. Rev. B **64**, 012514 (2001).

[23] H. Kotegawa, K. Ishida, Y. Kitaoka, T. Muranaka, and J. Akimitsu, Phys. Rev. Lett. **87**, 127001 (2001).

[24] E. Pavarini and I. I. Mazin, Phys. Rev. B **64**, 140504(R) (2001).

[25] S. H. Baek, B. J. Suh, E. Pavarini, F. Borsa, R. G. Barnes, S. L. Bud'ko, and P. C. Canfield, Phys. Rev. B **66**, 104510 (2002).

[26] For comparison, we have measured the ^{11}B NMR spectrum under the same conditions with the ^{11}B enriched MgB_2 powder sample that was used previously for the measurements in Ref. [25].

[27] G. C. Carter, L. H. Bennet, and D. J. Kahan, *Metallic Shifts in NMR, Part I, Progress in Material Science* (Pergamon Press, New York, 1977), Vol. 20.

[28] T. P. Onak, H. Landesman, R. E. Williams, and I. Shapiro, J. Phys. Chem. **63**, 1533 (1959).

ACKNOWLEDGEMENTS

I would like to take this opportunity to express my thanks to those who helped me with various aspects of conducting research and the writing of this thesis.

First and foremost, I am grateful to my advisors Dr. David C. Johnston and Dr. Ferdinando Borsa for their guidance, patience and support throughout the research and the writing of this thesis. My progresses could not have been made without their guidance and words of encouragements. I am especially thankful to Dr. Johnston for teaching me scientific rigor while helping me to improve my thesis, and to Dr. Borsa for many discussions and email communications that have always been very instructive.

Furthermore, I would like to express my appreciations to many former and current group members. I would like to thank Dr. Byoung Jin Suh for his guidance and generous helps during his summer and sabbatical year visit in Ames Lab. I have benefited a lot from his guidance and good suggestions on NMR experiments, data analysis, and paper writing. I thank Dr. A. Niazi for my training in sample synthesis and characterization. He is always so patient in offering his help. I would also like to thank Mr. Supriyo Das and Dr. Yogesh Singh for their collaboration and stimulating discussions. I thank Dr. Marilena Belesi for her guidance and many helps in NMR experiments. I would also like to thank Dr. Robert Vincent, Dr. Zeehoon Yang, Dr. Daniel Procissi, and Dr. Seung-Ho Baek for sharing their rich experiences in instrumentation. I would also like to thank Dr. Ioannis Rousochatzakis for many enjoyable and fruitful discussions.

I am also thankful to Dr. Jörg Schmalian, Dr. Robert McQueeney, Dr. Craig Ogilvie, and Dr. Steve Martin for kindly serving as committee members of my program of study.

I would like to extend my appreciations to the professors who offered excellent physics courses. I thank Dr. Marshall Luban, Dr. Jörg Schmalian, and Dr. Constantine Stassis for their inspirational teaching styles and Dr. Alex Travesset for my extensive training in solid state physics.

Last but not least, I would like to thank my parents, my wife, my sisters, and my parents-in-law for their love and endless support.

This work was performed at Ames Laboratory under Contract No. DE-AC02-07CH11358 with the U.S. Department of Energy. The United States government has assigned the DOE Report number IS-T 2615 to this thesis.